Spring 1991

Rotationally Resolved Laser Spectroscopy of the 3s2Σ+ ← 2p2Π Transition in 6Li20Ne and 7Li20Ne Van Der Waals Molecules

Chang Jae Lee
Old Dominion University

ROTATIONALLY RESOLVED LASER SPECTROSCOPY OF THE $3s^2\Sigma^+ \leftarrow 2p^2\Pi$ TRANSITION IN $^6Li^{20}Ne$ AND $^7Li^{20}Ne$ VAN DER WAALS MOLECULES

by

Chang Jae Lee

B.S. January, 1982, Young Nam University

M.S. May, 1985, Hampton University

A Dissertation Submitted to the Faculty of Old Dominion University
in Partial Fulfillment of the Requirements for the Degree of

DOCTOR OF PHILOSOPHY

APPLIED PHYSICS

OLD DOMINION UNIVERSITY

May, 1991

Approved by:

Mark D. Havey (Director)

ABSTRACT

ROTATIONALLY RESOLVED LASER SPECTROSCOPY OF THE $3s^2\Sigma^+ \leftarrow 2p^2\Pi$ TRANSITION IN $^6Li^{20}Ne$ AND $^7Li^{20}Ne$ VAN DER WAALS MOLECULES

Chang Jae Lee
Old Dominion University, 1991
Director: Dr. Mark D. Havey

The rotationally resolved absorption spectrum of the $^6Li^{20}Ne$ and $^7Li^{20}Ne$ $3s^2\Sigma^+ \leftarrow 2p^2\Pi$ transition has been observed. For each isotope, thirteen vibrational transitions from four vibrational levels (v"=0, 1, 2, and 3) of the lower $2p^2\Pi$ to six (v'=0, 1, 2, 3, 4, and 5) of the upper $3s^2\Sigma^+$ electronic state have been rotationally analyzed. Adiabatic potentials and dissociation energies for both states have been obtained through an inverse perturbation analysis. For the $2p^2\Pi$ state, a well depth of 212(5) cm^{-1} and an equilibrium separation of 4.36(2) a_o have been obtained. Analysis of the $3s^2\Sigma^+$ electronic state has revealed a barrier greater than 60 cm^{-1} above the atomic Li 3s asymptote and a well of 570(7) cm^{-1} located at 4.11(1) a_o below the asymptote. An anomalously large spin-orbit constant of A=2.77(3) cm^{-1} was determined for the $2p^2\Pi$(v"=0) state while no splitting is observed for transitions out of any $2p^2\Pi$ level with v">0.

ACKNOWLEDGEMENTS

I would like to thank Dr. Mark D. Havey, advisor, for not only guiding this dissertation research but also providing encouragement during my study at Old Dominion University. I am grateful to my committee members, Dr. G. Copeland, Dr. G. Hoy, Dr. A. Klein and Dr. L. Vahala, for their reading of this dissertation and their comments. I wish to express my appreciation for the support of my fellow graduate students, especially Mr. D. Olsgaard and Mr. R. Meyer. I am also grateful to my uncle Dr. Ja H. Lee and his family for encouragement. Finally, I would like to thank my wife, Yun Hee, and my son, Sang Gil for their understanding and encouragement throughout all of my graduate work.

This work was supported by the National Science Foundation and the Research Corporation.

TABLE OF CONTENTS

APPENDIXES

LIST OF TABLES

LIST OF FIGURES

Figure page

CHAPTER 1

INTRODUCTION

To gain understanding of various physical processes that occur when two atomic particles collide, considerable attention has been focused recently on the alkali metal-noble gas diatomic systems. Processes such as quenching of excited states, depolarization, pressure broadening of spectral lines, intra-multiplet transitions, collisional redistribution of radiation, etc, would be understood better if the interatomic potentials were more fully known [1, 2]. Unfortunately, these have still not been completely determined. Moreover, there is little information concerning the interatomic potentials, particularly when the alkali atom is in a highly excited state. The potentials of these diatomic molecules have been studied using a wide range of theoretical [3 - 28] and experimental techniques [29 - 52].

Theoretically, several methods have been developed to study interatomic interactions between alkali and rare gas atoms. One of them is *ab initio* calculations of adiabatic potentials for alkali-rare gas atom pairs [3 - 6]. These can be quite accurate when enough electronic configurations are included in the calculation. Calculations [7 - 24] using model potentials or pseudopotentials can be reduced to an effective three-body problem (alkali-metal core, valence electron, and rare-gas atom).

Also, numerous calculations have been made to obtain only the long range part of the interatomic potentials [25, 28]. Although the molecule repeatedly vibrates classically from an inner turning point (typically 1 Å) to an outer turning point (typically 5-20 Å), it spends almost all of its time in the long-range region (where the amplitude of its wave function is large). Hence such molecules are commonly called "long-range molecules" since their average internuclear distance is in the region where the potential energy is well described by its long-range form (e.g. $-C_6/R^6$).

Besides the possibility of developing new excimer lasers, interest in the alkali-rare gas diatomic systems is due to their role as a kind of test system, which allows the comparison of experimental and theoretical methods, and their accuracy. When one or both atoms has a closed electronic shell, the attractive forces between the atoms are normally inadequate to form a bound molecule which is stable under normal laboratory conditions. Thus, the standard spectroscopic techniques used for open shell systems are inapplicable [44]. A number of experimental techniques have been applied to determine the potentials of weakly bound alkali-rare gas systems. In the far-wing line broadening method [29 - 35], measurements have been made of the temperature dependent intensities of the far wings of alkali resonance lines broadened by the pressure of a rare gas. These measurements are related to interaction potentials of the alkali-rare gas using the quasistatic line-broadening theory or the equivalent classical Franck-Condon principle. Alternatively, in the atomic beam scattering experiment [36 -42], the cross sections are interpreted to obtain information about the ground- and excited-state interatomic potentials.

While these experimental techniques have been quite valuable, the accuracy to

which they have determined weakly attractive potentials has never been equal to that of spectroscopically determined potentials of strongly bound diatomic systems. In recent years, due to the development of new laser techniques, rotationally resolved laser spectroscopy [43 -52] has yielded the most accurate and consistent results for some weakly bounded van der Waals molecules which are formed by long range polarization binding. For the lighter alkali metal-rare gas pairs, however, only a few rotationally resolved spectroscopic investigations have been published [48, 52]. These few electron systems are most amenable to *ab initio* theoretical calculations of the potentials.

In this dissertation, the experimental method and the rotational-vibrational structure of the ^{6,7}Li-^{20}Ne $2p^2\Pi$ and $3s^2\Sigma^+$ states are presented. Thirteen vibrational transitions from the lower $2p^2\Pi$ (v"=0, 1, 2, 3) to the upper $3s^2\Sigma^+$ (v'=0, 1, 2, 3, 4, 5) electronic state have been observed and rotationally analyzed for ^{6}Li^{20}Ne and ^{7}Li^{20}Ne.

The interatomic potentials of both states [53] are discussed using the inverted perturbation analysis. A barrier at a large internuclear separation in the $3s^2\Sigma^+$ state is revealed. Also the spin-orbit interaction in the $2p^2\Pi$ state is measured. Due to the reactive properties of lithium metal, a special cell design is required and is discussed in a later section.

The remainder of this dissertation is organized as follows. In Chapter 2, the theoretical background of the experiment is presented. The experiment and the results are discussed in Chapters 3 and 4, respectively, followed by the spectral analysis and the discussion in Chapters 5 and 6. Results and discussion are summarized

in chapter 7.

CHAPTER 2

THEORETICAL BACKGROUND

A. THE ROTATIONAL TERM VALUES OF THE COMPONENTS OF A $2p^2\Pi$ STATE

According to the Born-Oppenheimer approximation [54], the wavefunction for the molecule is separable into a nuclear and an electronic part; that is

$$\Psi_{molecule}(\vec{r},\vec{R}) = \Psi_{el}(\vec{r};\vec{R})\,\chi_N(\vec{R}) \qquad (2\text{-}1)$$

where $\vec{R}$ is the internuclear distance, and $\vec{r}$ represents all electron coordinates in the molecule fixed system. Therefore, the total energy in wavenumber units can be expressed as the sum of nuclear and electronic parts,

$$E = E_{el} + G(v) + F(J) \qquad (2\text{-}2)$$

where the nuclear part of the energy is divided into the vibrational energy G(v), and the rotational energy F(J). The nonrelativistic Hamiltonian can be expressed as

$$H = H_{el} + H_{vib} + H_{rot} \qquad (2\text{-}3)$$

where H_{el} includes both the electron kinetic energy and the electrostatic potential energy for the nuclei and electrons. Therefore, the electronic part of Schrodinger equation can be written as [55, 56]

$$H_{el}\,|\psi^{\Lambda}_{el}\rangle = E^{\Lambda}_{el}(\vec{R})\,|\psi^{\Lambda}_{el}\rangle \qquad (2\text{-}4)$$

and the nuclear part as

$$[H_{vib}+H_{rot}+E^{\Lambda}_{el}(\vec{R})]\,|\chi^{v}_{N}(\vec{R})\rangle = E\,|\chi^{v}_{N}(\vec{R})\rangle \qquad (2\text{-}5)$$

where Λ is the projection of the electronic orbital angular momentum on the inter-nuclear axis, and v is the vibrational quantum number. $E^{\Lambda}_{el}(\vec{R})$ may be viewed as representing the potential curve in which the nuclei move. The nonzero off-diagonal matrix elements of H_{el}, H_{vib}, and H_{rot} which are neglected in the Born-Oppenheimer approximation, give rise to electrostatic perturbations, nonadiabatic interactions, and rotational perturbations, respectively. If the spin-orbit Hamiltonian H_{so} is included, the off-diagonal matrix elements of the operator will give rise to spin-orbit perturbations.

There are five angular momentum basis sets, from which Hund's case (a) - (e) bases [55 - 57] are defined. In the present discussion we shall restrict our attention to Hund's cases (a) and (b). Figure 1 shows the vector model of both the Hund's cases. In Hund's case (a), the electronic motion (spin and orbital) is coupled very strongly to the line joining the nuclei. The good quantum numbers are J, Λ, Σ, $\Omega=\Lambda+\Sigma$ and s. J is the total angular momentum; Λ is the projection of the orbital angular momentum

FIGURE 1

Vector model diagram of Hund's case (a) and (b).

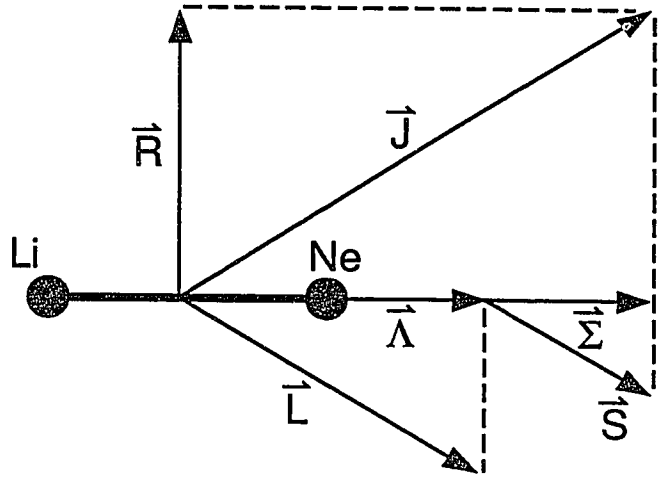

Case (a)

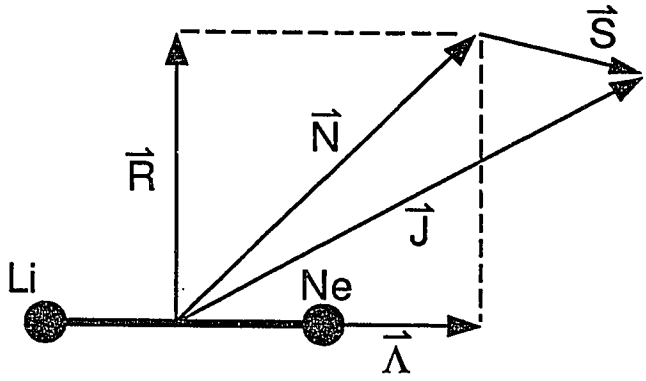

Case (b)

L on the molecular axis; while Σ is the projection of the spin s. In Hund's case (b) the spin is not coupled (or is very weakly coupled) to the internuclear axis. The good quantum numbers are J, N, Λ, and s. N is the total angular momentum excluding spin. In both cases, the molecular parity is also a good quantum number.

The case (b) function $|N, \Lambda, s, J\rangle$ may be expressed as linear combinations of case (a) functions $|\Lambda, s, \Sigma, J, \Omega\rangle$ using Clebsch Gorden coefficients [56, 58] as follows:

$$|N,\Lambda,s,J\rangle = \sum_{-s}^{s} C(J,s,\Omega,-\Sigma|N,\Lambda)\ |\Lambda,s,\Sigma,J,\Omega\rangle \qquad (2\text{-}6)$$

For the $^2\Pi$ state, there are two case (a) basis functions $|^2\Pi_{1/2}\rangle$ and $|^2\Pi_{3/2}\rangle$ [56 - 60]. For N=J+1/2 (F_2 level),

$$|F_2\rangle = -\sqrt{\frac{J-\frac{1}{2}}{2J+1}}\,|^2\Pi_{\frac{3}{2}}\rangle + \sqrt{\frac{J+\frac{3}{2}}{2J+1}}\,|^2\Pi_{\frac{1}{2}}\rangle \qquad (2\text{-}7)$$

and for N=J-1/2 (F_1 level),

$$|F_1\rangle = \sqrt{\frac{J+\frac{3}{2}}{2J+1}}\,|^2\Pi_{\frac{3}{2}}\rangle + \sqrt{\frac{J-\frac{1}{2}}{2J+1}}\,|^2\Pi_{\frac{1}{2}}\rangle \qquad (2\text{-}8)$$

Matrix element expressions for spin-orbit and rotational interactions are developed here starting with an expression for the rotational part of the

Hamiltonian [57]

$$H_{rot} = B_v\vec{R}^2 = B_v(R_x^2 + R_y^2) \qquad (2\text{-}9)$$

where $\vec{R}$ is the nuclear rotation angular momentum, and $R_z=0$, since $\vec{R}$ is perpendicular to the internuclear axis. $\vec{R}$ is related to the total angular momentum $\vec{J}$ of the molecular system by

$$\vec{R} \equiv \vec{J} - \vec{L} - \vec{S} \qquad (2\text{-}10)$$

Equation (2-9) can be reexpressed

$$\begin{aligned} H_{rot} = B_v[\,&(J^2-J_z^2) + (L^2-L_z^2) + (S^2-S_z^2) + (L^+S^- + L^-S^+) \\ &- (J^+L^- + J^-L^+) - (J^+S^- + J^-S^+)\,] \end{aligned} \qquad (2\text{-}11)$$

where the molecule fixed raising and lowering operators are

$$\begin{aligned} J^\pm &= J_x \pm iJ_y \\ L^\pm &= L_x \pm iL_y \\ S^\pm &= S_x \pm iS_y \end{aligned} \qquad (2\text{-}12)$$

and [57]

$$\begin{aligned} \langle A, M_A \pm 1 | A^\pm | A, M_A \rangle &= \sqrt{[A(A+1) - M_A(M_A \pm 1)]} \\ \langle J, \Omega \pm 1 | J^\mp | J, \Omega \rangle &= \sqrt{J(J+1) - \Omega(\Omega \pm 1)} \end{aligned} \qquad (2\text{-}13)$$

where A is an angular momentum operator $\vec{L}$ or $\vec{S}$, and M_A is the projection of A on the internuclear axis. The first three terms of H_{rot} have diagonal matrix elements; the last three terms have off diagonal matrix elements which are responsible for perturbations between different basis states. The diagonal part of H_{rot} is the rotational energy associated with the case (a) $|\Lambda, s, \Sigma; J, \Omega>$ basis function. These eigenvalues are

$$E_{rot}(V) = B_v[J(J+1) - \Omega^2 + S(S+1) - \Sigma^2] \qquad (2\text{-}14)$$

where

$$B_v = \frac{h}{8\pi^2\mu c}\langle v|\frac{1}{R^2}|v\rangle \qquad (2\text{-}15)$$

R is the internuclear distance, and μ is the reduced mass.

The orbital part

$$B_v[L(L+1) - \Lambda^2] \qquad (2\text{-}16)$$

is included in the electronic energy. In equation (2-16), there is a μ dependence that is responsible for part of the electronic isotope effect.

The off diagonal term $L^{\pm}S^{\mp}$ gives rise to spin-electronic mixing between different Hund's case (a) basis functions; $J^{\pm}S^{\mp}$ is an S-uncoupling operator and $J^{\pm}L^{\mp}$ is an L-uncoupling operator [56].

The spin-orbit part of the Hamiltonian [56, 57, 61] is

$$\begin{aligned} H_{so} &= A_v \vec{L}\cdot\vec{S} \\ &= A_v \left[L_z S_z + \frac{1}{2}\left(L^+S^- + L^-S^+\right) \right] \end{aligned} \qquad (2\text{-}17)$$

where A_v is the spin-orbit coupling constant. The diagonal matrix element is

$$\langle \Lambda, \Sigma, S, \Omega, v | H_{so} | \Lambda, \Sigma, S, \Omega, v \rangle = A_v \Lambda\Sigma \qquad (2\text{-}18)$$

Using equations (2-14 and 18), the diagonal parts of the rotational and spin orbit energies are obtained. For off-diagonal elements, S-uncoupling parts are only contributed. For example [56 - 60],

$$\begin{aligned} &\langle {}^2\Pi_{\frac{3}{2}} | -B_v J^- S^+ | {}^2\Pi_{\frac{1}{2}} \rangle \\ &= -B_v \sqrt{\left[J(J+1) - \frac{3}{4} \right]} \end{aligned} \qquad (2\text{-}19)$$

Therefore, the matrix for the case (a) $^2\Pi$ state [56, 57] is

	$^2\Pi_{\frac{1}{2}}$	$^2\Pi_{\frac{3}{2}}$
$^2\Pi_{\frac{1}{2}}$	$T_\Pi - \frac{A_v}{2} + B_v\left[J(J+1) + \frac{1}{4}\right]$	$-B_v\sqrt{\left[J(J+1) - \frac{3}{4}\right]}$
$^2\Pi_{\frac{3}{2}}$	$-B_v\sqrt{\left[J(J+1) - \frac{3}{4}\right]}$	$T_\Pi + \frac{A_v}{2} + B_v\left[J(J+1) - \frac{7}{4}\right]$

(2-20)

The desired rotational energy levels are found by solving the secular equation for the matrix of (2-20). Putting $Y=A_v/B_v$, the well known result of Hill and Van Vleck [62] is obtained

$$E = T_{\Pi}+B_v[(J+\frac{1}{2})^2-1] \pm \frac{B_v}{2}\sqrt{[Y(Y-4)+4(J+\frac{1}{2})^2]} \qquad (2\text{-}21)$$

Pure Hund's case (b) occurs when $A_v=0$. If $A_v=0$, equation (2-21) can be written as

$$F_1(N=J-\frac{1}{2}) = T_{\Pi}+B_v[(J-\frac{1}{2})(J+\frac{1}{2})-1]$$

$$F_2(N=J+\frac{1}{2}) = T_{\Pi}+B_v[(J+\frac{1}{2})(J+\frac{3}{2})-1] \qquad (2\text{-}22)$$

Both of these equations are of the form B[N(N+1)-1] which is the form of the Hund's case (b) expression $B[N(N+1)-\Lambda^2]$ with $\Lambda=1$.

B. INTERACTION BETWEEN THE $^2\Pi$ AND $^2\Sigma^+$ STATE

Before disscussing the interaction between the $^2\Pi$ and $^2\Sigma^+$ state, the concept of parity is introduced [56, 57]. There are two energy components (positive and negative) for each Λ and Σ (or $\Omega=\Lambda+\Sigma$), which are degenerate. These two

components are not symmetrized eigenfunctions of the total Hamiltonian. Only linear combinations of these functions have the well-defined symmetry which is called parity. There are three types of symmetry classifications. One is the total parity which is obtained by reflection of the spatial and spin coordinates of all electrons through the molecule-fixed x-z plane. The x-z plane is choosen for convention. The second is e/f parity, which excludes the J-dependence from the total parity. The third type of parity arises when only the spatial coordinates of all electrons are reflected through the molecule-fixed x-z plane. For $\Lambda=0$ states, there is Σ^+ or Σ^- symmetry. Only $|\Lambda=0>$ basis function have this third type of parity because they can not be put into linear combinations of the form ($||\Lambda|>\pm|-|\Lambda|>$) [57].

Returning to the interaction between the $^2\Pi$ and $^2\Sigma^+$ state, consider a $^2\Sigma^+$ state that is sufficiently far from a $^2\Pi$ state. The diagonal part of the matrix element in case (a) [56, 57] is

$$\begin{aligned} &\langle \Lambda=0, \Sigma=\tfrac{1}{2}, \Omega=\tfrac{1}{2}|H|\Lambda=0, \Sigma=\tfrac{1}{2}, \Omega=\tfrac{1}{2}\rangle \\ &= T_{\Sigma}^{v}+B_v[J(J+1)+\tfrac{1}{4}] \end{aligned} \qquad (2\text{-}23)$$

The nonzero matrix elements of the S-uncoupling operator give rise to states that have e and f symmetry components,

$$\begin{aligned} |^2\Sigma_e^+\rangle &= \frac{1}{\sqrt{2}}\left[|J, \Omega=\tfrac{1}{2}, \Lambda=0, \Sigma=\tfrac{1}{2}\rangle + |J, -\Omega=-\tfrac{1}{2}, -\Lambda=0, -\Sigma=-\tfrac{1}{2}\rangle\right] \\ |^2\Sigma_f^+\rangle &= \frac{1}{\sqrt{2}}\left[|J, \Omega=\tfrac{1}{2}, \Lambda=0, \Sigma=\tfrac{1}{2}\rangle - |J, -\Omega=-\tfrac{1}{2}, -\Lambda=0, -\Sigma=-\tfrac{1}{2}\rangle\right] \end{aligned} \qquad (2\text{-}24)$$

Since the matrix elements of the S-uncoupling operator are

$$\begin{aligned} &\langle \Lambda=0,\ \Sigma=\frac{1}{2},\ \Omega=\frac{1}{2} \mid -BJ^{-}S^{+} \mid \Lambda=0,\ \Sigma=-\frac{1}{2},\ \Omega=-\frac{1}{2}\rangle \\ &= -B_v\left(J+\frac{1}{2}\right) \end{aligned} \tag{2-25}$$

the energy eigenvalues are

$$\begin{aligned} E(^2\Sigma_e^+) &= T_\Sigma^v + B_v\left[J(J+1) + \frac{1}{4} - \left(J+\frac{1}{2}\right)\right] \\ E(^2\Sigma_f^+) &= T_\Sigma^v + B_v\left[J(J+1) + \frac{1}{4} + \left(J+\frac{1}{2}\right)\right] \end{aligned} \tag{2-26}$$

Therefore, the energy separation between the f and e levels are separated by $2B_v(J + 1/2)$.

For the matrix element between the $^2\Pi_{3/2}$ and $^2\Sigma^+$ states, only the L-uncoupling interaction with $^2\Sigma^+$ is nonzero. That is

$$\begin{aligned} &\langle ^2\Pi_{\frac{3}{2}},\ v_\Pi,\ J \mid H_{so}+H_{rot} \mid ^2\Sigma^+,\ v_\Sigma,\ J\rangle \\ &= -bB_v\sqrt{J(J+1)-\frac{3}{4}} \end{aligned} \tag{2-27}$$

where $b = \langle \Lambda=1 \mid L^+ \mid \Lambda=0\rangle$ and $v_\Pi = v_\Sigma$ which assumes that the potential curves for the $^2\Pi$ and $^2\Sigma^+$ states are the same [56]. Also,

$$\begin{aligned} &\langle ^2\Pi^e_{\frac{3}{2}},\ v_\Pi,\ J \mid H_{rot} \mid ^2\Sigma^{+e},\ v_\Sigma,\ J\rangle \\ &= \langle ^2\Pi^f_{\frac{3}{2}},\ V_\Pi,\ J \mid H_{rot} \mid ^2\Sigma^{+f},\ V_\Sigma,\ J\rangle \\ &= -bB_v\sqrt{J(J+1)-\frac{3}{4}} \end{aligned} \tag{2-28}$$

where the symmetrized $^2\Pi$ functions are

$$|^2\Pi^{e,f}_{\frac{3}{2}}\rangle = \frac{1}{\sqrt{2}}\left[\left|J, \Omega=\frac{3}{2}, \Lambda=1, \Sigma=\frac{1}{2}\right\rangle \pm \left|J, -\Omega=-\frac{3}{2}, -\Lambda=-1, -\Sigma=-\frac{1}{2}\right\rangle\right]$$

$$|^2\Pi^{e,f}_{\frac{1}{2}}\rangle = \frac{1}{\sqrt{2}}\left[\left|J, \frac{1}{2}, 1, -\frac{1}{2}\right\rangle \pm \left|J, -\frac{1}{2}, -1, \frac{1}{2}\right\rangle\right] \qquad (2\text{-}29)$$

The interaction between the $^2\Pi_{1/2}$ and $^2\Sigma^+$ states displays three types of off-diagonal interaction. The first type is a spin-orbit interaction. According to the selection rule $\Delta\Omega=0$ and e $\leftarrow/\rightarrow$ f, the matrix element is

$$\left\langle \Lambda=1, \Sigma=-\frac{1}{2}, \Omega=\frac{1}{2}, v_\Pi \middle| H_{so} \middle| \Lambda=0, \Sigma=\frac{1}{2}, \Omega=\frac{1}{2}, v_\Sigma \right\rangle = a_+ \frac{\langle v_\Pi | v_\Sigma \rangle}{2} = \frac{a_+}{2} \qquad (2\text{-}30)$$

where $v_\Pi = v_\Sigma$ and $a_+ = \langle \Lambda=1|\hat{a}L^+|\Lambda=0\rangle$ [56]. The second type is the spin-electronic

$$\left\langle \Lambda=1, \Sigma=-\frac{1}{2}, \Omega=\frac{1}{2}, v_\Pi \middle| BL^+S^- \middle| \Lambda=0, \Sigma=\frac{1}{2}, \Omega=\frac{1}{2}, v_\Sigma \right\rangle = bB_v \qquad (2\text{-}31)$$

And the third type is the L-uncoupling

$$\left\langle \Lambda=1, \Sigma=-\frac{1}{2}, \Omega=\frac{1}{2}, v_\Pi \middle| -BJ^-L^+ \middle| \Lambda=0, \Sigma=-\frac{1}{2}, \Omega=-\frac{1}{2}, v_\Sigma \right\rangle = -bB_v\left(J+\frac{1}{2}\right) \qquad (2\text{-}32)$$

Therefore, the off-diagonal interaction between $^2\Pi_{1/2}$ and $^2\Sigma^+$ are

$$\begin{aligned} \langle {}^2\Pi^e_{\frac{1}{2}} | H_{so}+H_{rot} | {}^2\Sigma^{+e}\rangle &= \frac{a_+}{2}+bB_v-bB_v(J+\frac{1}{2}) \\ \langle {}^2\Pi^f_{\frac{1}{2}} | H_{so}+H_{rot} | {}^2\Sigma^{+f}\rangle &= \frac{a_+}{2}+bB_v+bB_v(J+\frac{1}{2}) \end{aligned} \qquad (2\text{-}33)$$

Note that the difference between the e and f matrix elements is due to the L-uncoupling operator.

The interaction matrix between $^2\Pi_\Omega$ and $^2\Sigma^+$ [56, 57] is

	$^2\Pi_{\frac{1}{2}}$	$^2\Pi_{\frac{3}{2}}$	$^2\Sigma^+_{\frac{1}{2}}$
$^2\Pi_{\frac{1}{2}}$	$T_\Pi-\frac{A_v}{2}+B_v[J(J+1)+\frac{1}{4}]$	$-B_v\sqrt{[J(J+1)-\frac{3}{4}]}$	$\frac{a_+}{2}+[1\mp(J+\frac{1}{2})]bB_v$
$^2\Pi_{\frac{3}{2}}$		$T_\Pi+\frac{A_v}{2}+B_v[J(J+1)-\frac{7}{4}]$	$-bB_v\sqrt{(J-\frac{1}{2})(J+\frac{3}{2})}$
$^2\Sigma^+_{\frac{1}{2}}$			$T_v^\Sigma+B_v(J+\frac{1}{2})^2$

The Λ-doubling, due to the $^2\Pi$ - $^2\Sigma^+$ interaction [56], is different for the e and f levels. According to second order perturbation theory [56, 63], the energy shift for the $^2\Pi_{1/2}{}^e$ levels is

$$\Delta E^e_{\frac{1}{2}} = \frac{\left[\frac{a_+}{2}+\{1-(J+\frac{1}{2})\}bB_v\right]^2}{E_\Pi-E_\Sigma} \qquad (2\text{-}34)$$

and for the $^2\Pi_{1/2}{}^f$ levels is

$$\Delta E^f_{\frac{1}{2}} = \frac{\left[\frac{a_+}{2} + \{1+(J+\frac{1}{2})\}bB_v\right]^2}{E_\Pi - E_\Sigma} \qquad (2\text{-}35)$$

Therefore, the Λ-doubling for $^2\Pi_{1/2}$ is given by

$$\begin{aligned}\Delta E^{fe}_{\frac{1}{2}} &= \Delta E^f_{\frac{1}{2}} - \Delta E^e_{\frac{1}{2}} = \frac{2\,[a_+bB_v + 2b^2B_v^2]}{E_\Pi - E_\Sigma}\,(J+\tfrac{1}{2}) \\ &= P(J+\tfrac{1}{2})\end{aligned} \qquad (2\text{-}36)$$

where

$$P = \frac{2\,[a_+bB_v + 2b^2B_v^2]}{E_\Pi - E_\Sigma} \qquad (2\text{-}37)$$

For the $^2\Pi_{3/2}$ state,

$$\begin{aligned}\Delta E^f_{\frac{3}{2}} &= \Delta E^e_{\frac{3}{2}} = \frac{b^2B_v^2\,[J(J+1)-\frac{3}{4}]}{E_\Pi - E_\Sigma} \\ &= \frac{q}{2}\,[J(J+1)-\tfrac{3}{4}]\end{aligned} \qquad (2\text{-}38)$$

Therefore, there is no direct effect on Λ-doubling in the $^2\Pi_{3/2}$ state. However, $\langle {}^2\Pi_{3/2}{}^e|H|{}^2\Pi_{1/2}{}^e\rangle$ and $\langle {}^2\Pi_{3/2}{}^f|H|{}^2\Pi_{1/2}{}^f\rangle$ are affected in a parity-dependent manner. Using second order perturbation theory as mentioned above, Λ-doubling in the $^2\Pi_{3/2}$

state gives [56]

$$\Delta E^{fe}_{\frac{3}{2}} \approx 2\left(J-\frac{1}{2}\right)\left(J+\frac{3}{2}\right)\left(J+\frac{1}{2}\right)B_v q/A_v \qquad (2\text{-}39)$$

In the pure precession hypothesis [64, 65]

$$a_+ = \sqrt{L(L+1)}\,A_v \quad and \quad b = \sqrt{L(L+1)}$$

then [56]

$$p=\frac{2A_vB_vL(L+1)}{E_\Pi-E_\Sigma}$$
$$q=\frac{2B_v^2L(L+1)}{E_\Pi-E_\Sigma} \qquad (2\text{-}40)$$

where $a_+ \gg 2bB_v$ is assumed. For the $2p^2\Pi$ state in LiNe, the estimated values for p and q, using Roberts potentials [66], are 1×10^{-3} cm^{-1} and 3×10^{-4} cm^{-1}, respectively. We believe these are the maximum values since the potential cureves for $^2\Pi$ and $^2\Sigma^+$ states are assumed to be the same. Therefore, it was expected that Λ-doubling could not be resolved with the resolution available in this experiment.

C. INTENSITY DISTRIBUTION IN ROTATIONAL BANDS

The spectral lines are characterized not only by their position within the spectrum, but also by their intensity or strength. In this section, a theoretical relation of absorption line strength between spectral lines in rotational bands is derived.

The intensity distribution of absorption lines in rotational bands is given as follows [55, 67, 68];

$$I^{m'm''} \sim CN_{m''} \frac{\sum |R^{m'm''}|^2}{g_{J''}} \qquad (2\text{-}41)$$

where C is a constant, $N_{m''}$ is the number of molecules in the initial state m" (n", v", J"), m' is denotes the upper state (n', v', J'), $g_{J''}=2J''+1$, and $R^{m'm''}$ are the matrix elements of the electric dipole moment. In the Born-Oppenheimer approximation the dipole moment of the molecule can be written as [55]

$$\begin{aligned} R^{m'm''} &= \int \psi^*_{m'} M \psi_{m''} d\tau \\ &= \int \psi^*_{n'v'J'\Omega'M'} M_e \psi_{n''v''J''\Omega''M''} d\tau \\ &+ \int \psi^*_{n'} \psi_{n''} d\tau_e \int \psi^*_{v'J'\Omega'M'} M_n \psi_{v''J''\Omega''M''} d\tau_n \end{aligned} \qquad (2\text{-}42)$$

where M is the operator of the electric moments, $M=M_e+M_n$, $d\tau=d\tau_e + d\tau_n$, and $\Psi_{m'}$ and $\Psi_{m''}$ are the eigenfunctions of the two states. Since M_n only depends on the internuclear distance, and the electronic eigenfunctions belong to different electronic states, we have

$$\int \psi_{n'}^{*} \psi_{n''} d\tau_e = 0 \qquad (2\text{-}43)$$

Therefore, equation (2-42) can be rewritten as

$$R^{m'm''} = \int \psi_{m'}^{*} M_e \psi_{m''} d\tau \qquad (2\text{-}44)$$

Dropping the suffix e on M and considering the space fixed dipole operator M_z in a linearly polarized laser field, equation (2-44) can be expressed as

$$R^{m'm''} = \int \psi_{m'}^{*} M_o^{sp} \psi_{m''} d\tau_e d\tau_n \qquad (2\text{-}45)$$

where [60]

$$M_0^{sp} = \sum_{k=-1}^{1} D_{0k}^{1} M_k^{mol} \qquad (2\text{-}46)$$

The vector transition dipole operator in a spherical basis [58, 60] is defined as

$$M_1^{mol} = e\frac{x-iy}{\sqrt{2}} = e\sqrt{\frac{4\pi}{3}} r Y_{11}$$

$$M_0^{mol} = ez = e\sqrt{\frac{4\pi}{3}} r Y_{10} \qquad (2\text{-}47)$$

$$M_{-1}^{mol} = e\frac{x+iy}{\sqrt{2}} = e\sqrt{\frac{4\pi}{3}} r Y_{1-1}$$

where the superscript mol denotes the molecule fixed frame, e is the electron charge,

and r is the position of the electron. The rotation matrix $D_{m'm''}(\phi, \theta, 0)$ with θ and ϕ being the Euler angles, gives the orientation of the internuclear axis in the molecule fixed frame with respect to the space fixed frame [58 - 60]. The third Euler angle, ρ, is zero, since the internuclear axis is fixed on an axis of the space fixed coordinate system. Then equation (2-45) becomes

$$R^{m'm''} = [\int \psi^*_{v'} \psi_{v''} R^2 dR] \int \psi^*_{n'J'M'\Lambda'} M_0^{ep} \psi_{n''J''M''\Lambda''} d\tau_e d\Omega_R \qquad (2\text{-}48)$$

where $d\tau_n = R^2 dR d\Omega_R$. Since M_o does not depend on the internuclear distance R and the change of the electronic eigenfunction ψ_n vs R is usually slow, the term in brackets can be separated and is called the overlap integral (Frank-Condon factor)

$$q^{vib}_{v'v''} = \int \psi^*_{v'} \psi_{v''} R^2 dR \qquad (2\text{-}49)$$

The square of equation (2-49) is proportional to the band strength.

Substituting equation (2-46, 47, and 49) in equation (2-48),

$$R^{m'm''} = q^{vib}_{v'v''} \sum_{k=-1}^{1} [e\sqrt{\frac{4\pi}{3}} \int \psi^*_{n'} r Y_{1k} \psi_{n''} d\tau_e \int \psi^*_{J'M'\Lambda'} D^1_{0k} \psi_{J''M''\Lambda''} d\Omega_R]$$

$$= q^{vib}_{v'v''} e\sqrt{\frac{4\pi}{3}} (\int \psi^*_{n'}(r)\, r\, \psi_{n''}(r)\, r^2 dr) \sum_{k=-1}^{1} [(\int Y^*_{l'm'} Y_{1k} Y_{l''m''} d\Omega_R)$$

$$(\frac{\sqrt{(2J'+1)(2J''+1)}}{4\pi} \int D^{J'*}_{M'\Lambda'} D^1_{0k} D^{J''}_{M''\Lambda''})] \qquad (2\text{-}50)$$

$$R^{m'm''} = q^{vib}_{v'v''}\psi_{n'n''}(r)\, e\sqrt{\frac{4\pi}{3}}\sum_{k=-1}^{1}\left[\left(\int Y^{*}_{1'\Lambda'}Y_{1k}Y_{1''\Lambda''}d\Omega_R\right)\right.$$

$$\left.\sqrt{\frac{2J''+1}{2J'+1}}C(J''1J';M''0M')\;C(J''1J';\Lambda''k\Lambda')\right]$$

Now the Clebsch-Gordon coefficient is zero unless [58 - 60]

$$M \equiv M'' = M'$$

$$\Delta\Lambda \equiv \Lambda' - \Lambda'' = k = 0, \pm 1 \qquad (2\text{-}51)$$

$$\Delta J = J' - J'' = 0, \pm 1$$

Since we are interested only in the transition $2p^2\Pi \rightarrow 3s^2\Sigma^+$, the term with k=-1 is non-zero.

$$R^{m'm''} = q^{vib}_{v'v''}\left[\psi_{n'n''}(r)\, e\sqrt{\frac{4\pi}{3}}\int Y^{*}_{00}Y_{1-1}Y_{11}d\Omega_R\right] \qquad (2\text{-}52)$$

$$\sqrt{\frac{2J''+1}{2J'+1}}C(J''1J';M0M)\;C(J''1J';1-10)$$

The integration of the product of three spherical harmonics is [60]

$$\int Y^{*}_{00}Y_{1-1}Y_{11}d\Omega = -\sqrt{\frac{1}{4\pi}} \qquad (2\text{-}53)$$

By letting

$$\psi^{ele}_{n'n''} = -e\sqrt{\frac{1}{3}}\psi_{n'n''}(r)$$

$$S_{J'J''} = \sum_{M} |R^{m'm''}_{rot}|^2 \qquad (2\text{-}54)$$

$$= \sum_{M} \left|\sqrt{\frac{2J''+1}{2J'+1}} C(J''1J';M0M)\ C(J''1J';1\text{-}10)\right|^2$$

then

$$\sum_{M} |R^{m'm''}|^2 = |q^{vib}_{v'v''}|^2\ |\psi^{ele}_{n'n''}|^2\ S_{J'J''} \qquad (2\text{-}55)$$

where $S_{J'J''}$ is called line strength. For the Q branch, $\Delta J=0$

$$S^{Q}_{J''J''} = \frac{2J''+1}{6} \qquad (2\text{-}56)$$

For the R branch, $\Delta J=+1$ (J'=J"+1)

$$\therefore\ S^{R}_{J''+1\,J''} = \frac{J''}{6} \qquad (2\text{-}57)$$

For the P branch, $\Delta J=-1$ (J'=J"-1)

$$\therefore\ S^{P}_{J''-1\,J''} = \frac{J''+1}{6} \qquad (2\text{-}58)$$

According to the Bolzmann distribution,

$$N_{m''} = N_{n''v''} \frac{2J''+1}{Q_r} e^{-F_{J''}/kT} \qquad (2\text{-}59)$$

The partition function Q_r for rotational states is the rotational state sum, and for sufficiently large T or small B_v,

$$Q_r \approx \int_0^\infty (2J+1)\, e^{-F_{J''}/kT} dJ$$

If the distortion terms are neglected in the rotational energy, the partition function [55] is

$$Q_r \approx \frac{kT}{B_v''} \qquad (2\text{-}60)$$

$$\text{so,} \quad N_{m''} = N_{n''v''} \frac{B_v''}{kT} (2J''+1)\, e^{-B_v''J''(J''+1)/kT} \qquad (2\text{-}61)$$

By substituting equations (2-55 and 61) to equation (2-41),

$$I^{m'm''} \sim C_{m'm''} S_{J'J''} e^{-B_v''J''(J''+1)/kT} \qquad (2\text{-}62)$$

where

$$C_{m'm''} = \frac{C}{kT} B_v'' N_{n''v''} \left|q_{v'v''}^{vib}\right|^2 \left|\Psi_{n'n''}^{ele}\right|^2$$

$|q_{v'J'v''}^{vib}|^2$ is the Frank-Condon factor and C is constant.

The comparison between the theoretical line intensities according to equation (2-62) and the experimental results is discussed in Chapter 6. If equations (2-56, 57, and 58) are substituted into equation (2-62), the relative intensity ratio between the Q, R, and P branches at the same J" is

$$I^Q : I^R : I^P = 2J''+1 : J'' : J''+1 \qquad (2\text{-}63)$$

Thus relatively, the Q branch is the strongest and R is the weakest branch. But as J" is increased, the intensity of the R and P branches are comparable to each other, and the value I(Q)/I(R) becomes smaller.

CHAPTER 3

EXPERIMENT

A. OVERVIEW OF THE EXPERIMENTAL METHOD

Qualitative interatomic potentials of LiNe molecules are shown in Figure 2. Li atoms in the $1s^2 2s$ ground state are excited to the $1s^2 2p$ state by laser 1 at a wavelength of 671.0nm. At low Ne gas pressures these excited Li atoms will radiate before forming bound molecules, yielding a spectrum due to transitions from free exited atoms. As the Ne gas density is increased, LiNe molecules in the $2p^2\Pi$ electronic state are produced by collisions between an excited Li(2p) atom and two ground state atoms of Ne. At the thermal equilibrium of the experimental temperature T, the LiNe molecules in $2p^2\Pi$ states are rotationally and vibrationally distributed in bound states according to the Maxwell-Boltzman distribution law. Previous cell experiments [32, 34] have shown that the relative atomic and molecular populations are nearly in thermal equilibrium at the gas temperature of about 350°K for a Ne pressure of 50 torr.

A second, scanning laser 2 excites individual molecules from rotational-vibrational $2p^2\Pi$ levels (lower state) and produces excited molecules in the $3s^2\Sigma^+$ state

FIGURE 2

Qualitative interaction potentials for selected LiNe molecular states. The vertical axis is not to scale.

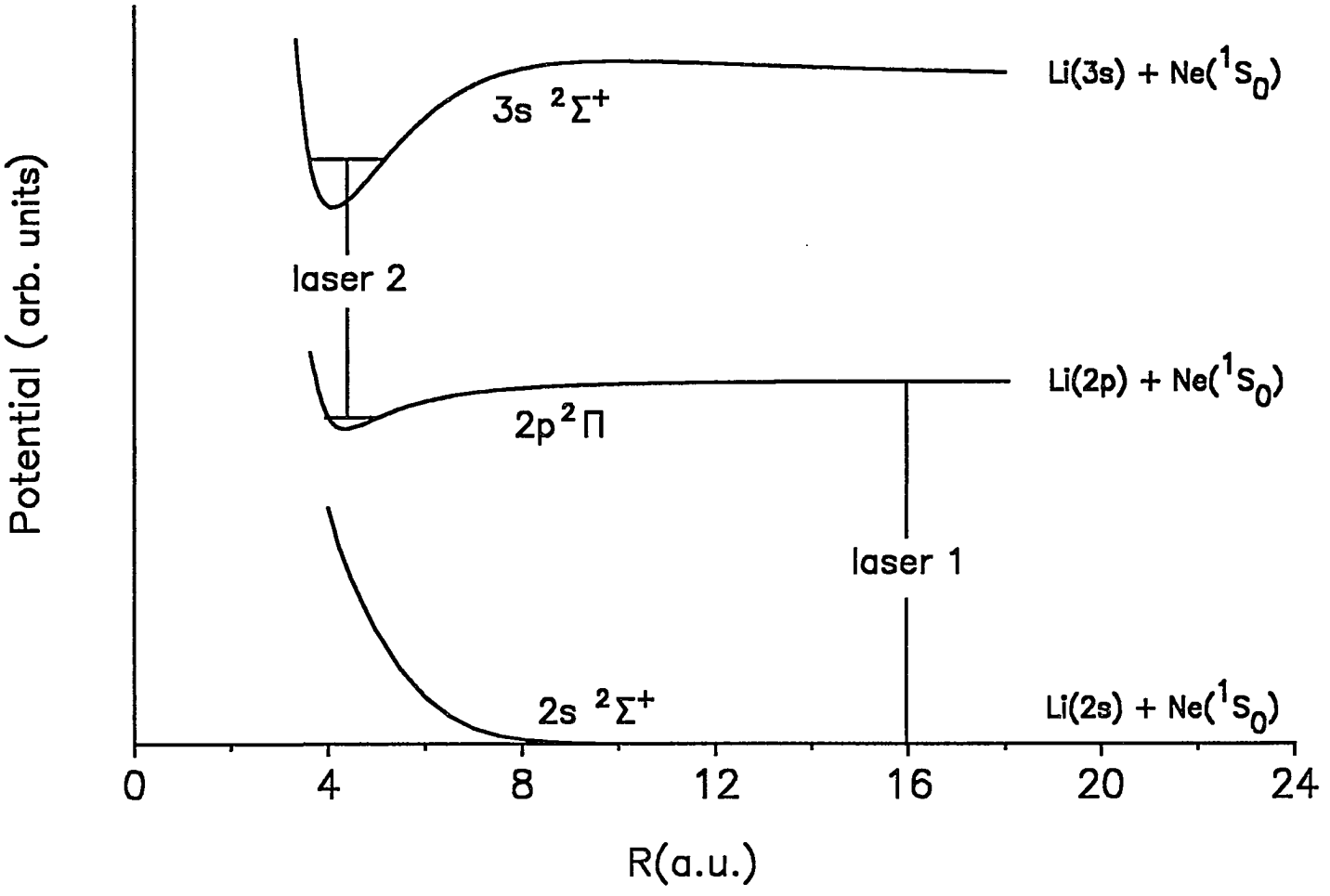

(upper state) of LiNe. Laser 2 is scanned over the range of possible transitions between the $2p^2\Pi$ and $3s^2\Sigma^+$ electronic states. The molecular reemission on the $3s^2\Sigma^+ \rightarrow 2s^2\Sigma^+$ transition (380-410 nm) serves as the signal in this laser absorption experiment.

In the following sections, experimental details associated with each of these steps are presented. In particular, due to the chemical reactivity of Li with air and Pyrex, special treatment of samples is required in this experiment. In the following section, the cell design is described in detail. Second, to continuously scan laser 2 over a wide range (11,680 cm^{-1} - 12,400 cm^{-1}) of possible transitions without mode hops, a scanning method has been developed; this is described in detail. Third, to identify the absolute vacuum wavelength of the laser, three references: a Fizeau wavemeter, a 0.5 cm^{-1} Fabry-Perot etalon, and a uranium-neon hollow cathode lamp have been employed. The background free signal detection system and the computer controlled data acquisition system are also discussed.

B. CELL DESIGN

A schematic diagram of the cell design is presented in Figure 3. A 250 cm^3 Pyrex flask with sidearms is mounted on the gas handling system. On the end of each of the 25 mm o.d. and 70 mm long sidearms, Brewster angle windows are attached to reduce the reflection of the laser light by the cell windows. The fluorescence view

FIGURE 3

A schematic diagram of the experimental apparatus.

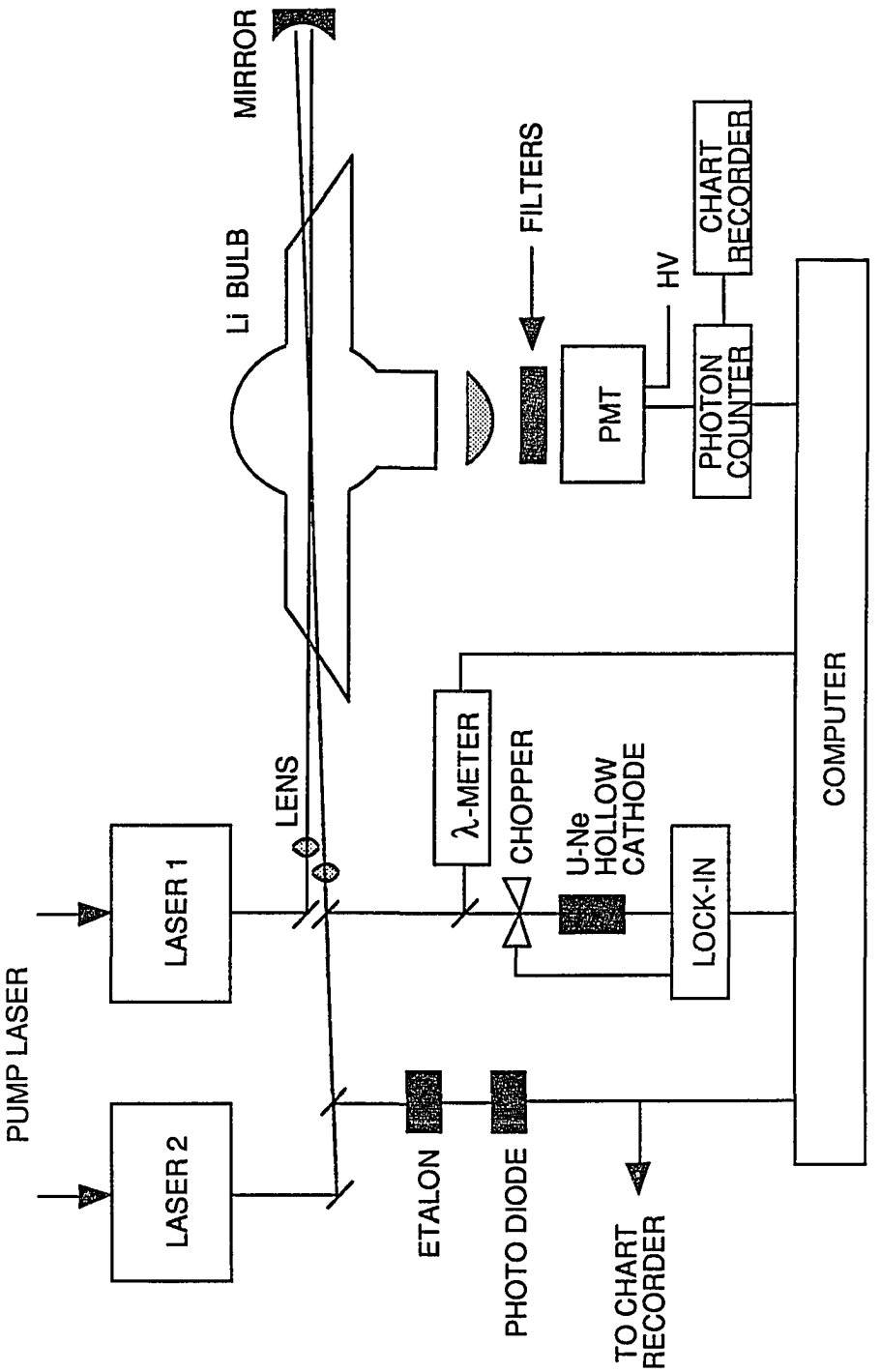

port is also attached to a 40 mm o.d. and 50 mm long pyrex tube on the cell perpendicular to the sidearm. A quartz window is mounted on the end of the viewing port using a low vapor pressure epoxy (Torr Seal, Varian Ind. Prod.).

For long term operation of the cell, the long sidearms and view port (from the center of the cell) are required to inhibit diffusion of Li vapor to the wall surface; Li vapor reacts with the hot walls upon contact. This reaction produces a tan colored coating on the windows which reduced significantly the signal of the experiment. This cell window deterioration is slowed by the presence of a noble gas. Therefore, choosing the proper Ne pressure in the cell is an important factor in this experiment.

Figure 4 shows the Li oven which is supported in the cell by an 8 mm o.d. quartz tube. The Li oven is made from iron. The dimensions of the iron boat are 8 mm inner diameter, 20 mm long, and the walls are 0.8 mm thick. There is round lip on the top of the Li oven with about a 10° slope to prevent spillage of the hot liquid Li. The thermocouple (Platinum and Platinum-10 % Rhodium) is attached to the side of the iron boat to monitor the temperature of the Li cell as shown as Figure 4.

The hot part (20 cm in long) of a helically-wound coaxial heater (1 mm o.d., ARi Industries, Inc.) is located inside the iron boat, while the cold part of heater (15 cm in long) is outside the boat. The sheath of the wire is made from Inconel 600 that does not noticeably react with hot Li.

The heater wire and thermocouple are connected to the power supply and temperature monitor through holes in a vacuum grease sealed glass joint cap, as shown as Figure 5. Torr Seal is used to fill the holes and provide a vacuum seal. The quartz tube with the iron boat is attached to the center of the inside of the glass

FIGURE 4

Design of the Li boat.

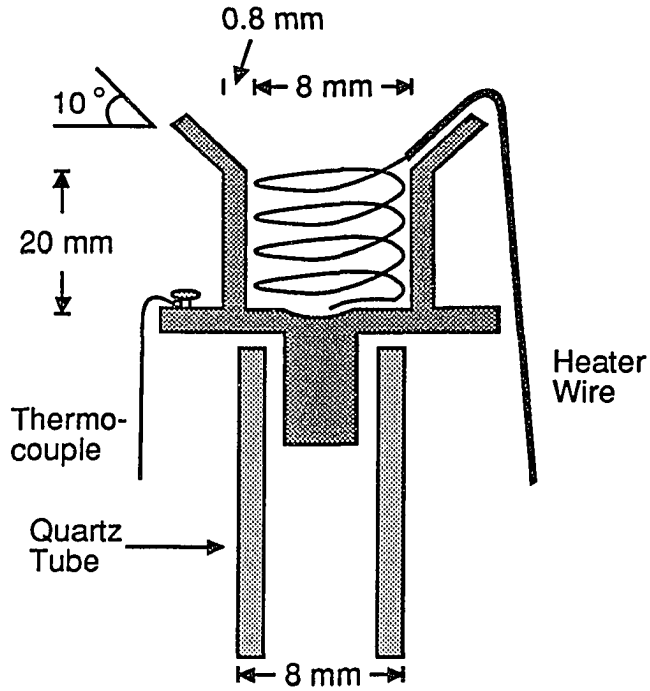

FIGURE 5

Schematic diagram of the cell.

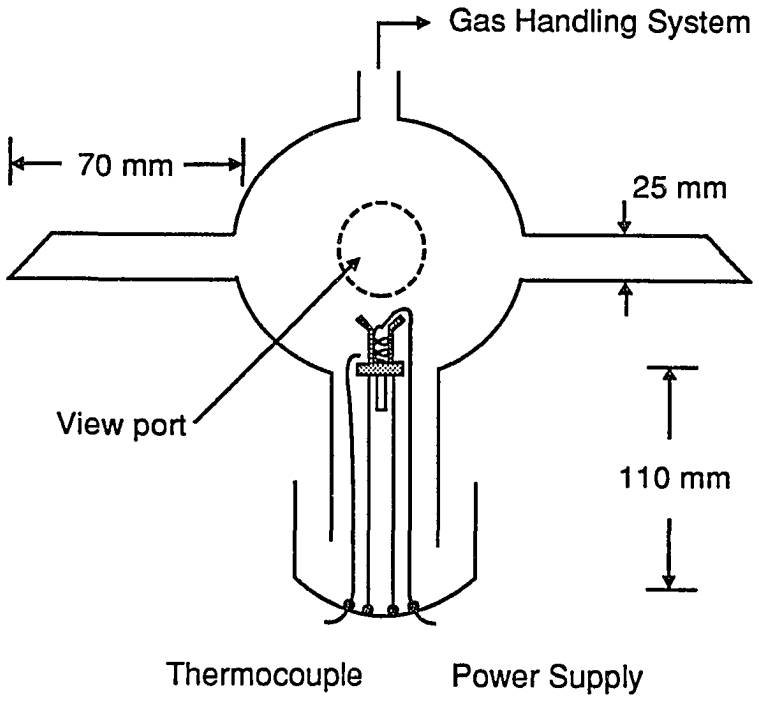

joint cap with Torr Seal. There is a small hole in the side of the quartz tube so gas can go in and out of the tube. The Pyrex cap with the iron boat is inserted into a 119 mm long grounded male tube and sealed with vacuum grease. The temperature of the grease joint part is only about 300 - 310°K since it is about 90 mm away from the hot iron boat. A small box fan (12 VDC) is used to insure that the grease joint stays cool. The top of the iron boat is located about 15 mm below the center of the cell.

C. SAMPLE PREPARATION

The following steps are used to insure having a clean Li cell. First, the iron boat with heater wire is rinsed with semiconductor grade trichloroethylene (Alfa, 99 % min.) to remove oil on the surface. Second, it is rinsed with flowing water for a few seconds. Then the first and second steps are repeated several times. To clean the glass parts, diluted HF (50 % water) is used for a few seconds followed by rinsing in water. Next, semiconductor grade acetone (Alfa, 99.6 % min.) is used and the cell is dried in air. Finally, the iron boat is attached to the vacuum system and heated under vacuum at 750°K for more than 8 hours. At the high temperature of the iron boat, a base pressure of 10^{-7} torr could be obtained with an ion pump.

Since the Li reacts with air very quickly, a glove box is used when loading Li into the boat to slow down the reaction of Li metal. The glove box is filled with nitrogen gas which is constantly flowing during the process. Metallic ^{6}Li (99.5 %)

and ^{7}Li (99.9 %) are purchased from Oak Ridge National Laboratory. The metallic Li is rinsed with trichloroethylene and cut into small pieces using a chemically cleaned knife. Several small pieces of metal ^{6}Li or ^{7}Li are squeezed into the cleaned iron boat in the glove box. Then, the iron boat with Li is transferred to the vacuum system using a glass tube filled with nitrogen.

To reduce the exposure time to air, the nitrogen is flowed in the cell and the iron boat is slid into the cell as quickly as possible. Then the cell is evacuated using a roughing pump. As soon as the ion pump is operational, the temperature of the Li boat is increased slowly up to 500°K; this achieves an initial outgassing of the Li metal. About 100 torr of Ne gas is added after the cell cools. Then the Li boat is heated again until the temperature is about 750°K. The shiny liquid Li can be seen at the top of the iron boat at this temperature. After about 5 hours, the cell is cooled down and the gas is pumped out.

Figure 6 shows a schematic diagram of the gas handling and vacuum system. Before the ion pump is started, the system is pumped out using the rough pump until the pressure is below 10^{-3} torr. The pressure is measured with a Hastings-Raydist Inc. thermocouple gauge model DV-6M and model SV-4 combination. Once the pressure is below 10^{-3} torr, the ion pump (Varian Ind. Prod., Vaclon 60l) can be started. The base pressure is on the order of 10^{-7} torr after pumping overnight. Flaming the Pyrex part of the system also helped to improve the vacuum.

A capacitance manometer baratron gauge (MKS Inst. Inc., Type 221A) is used to measure and monitor the Ne pressure in the system; it has an accuracy of about 0.1 Torr. Heating the Li boat up to 650°K with 50 torr of Ne produces an estimated Li

FIGURE 6

Schematic diagram of the vacuum-gas handling system.

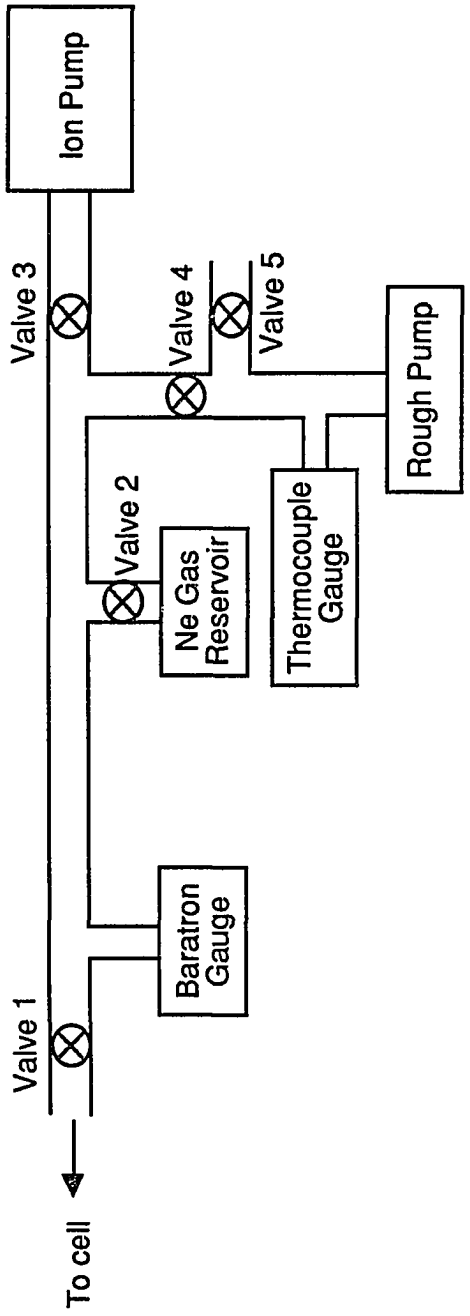

density of about 10^{11} cm^{-3} [69] in the region just above the iron boat.

D. LASERS

In this experiment, two continuous wave (c.w.) dye lasers, both pumped by Ar^+ lasers are used as shown in Figure 7. Laser 1 is tuned to the Li 2s-2p resonance transition at 671.0 nm, promoting Li atoms to the 2p state. A Control Ar^+ laser (Holobeam Laser Inc., Model 554A) with maximum 6W of power pumped the DCM dye (Exciton) of laser 1. Laser 1 is a Coherent Model 599 dye laser. The concentration of the DCM dye is about 1.5 x 10^{-3} mole/l with a ratio of 3:16 of Benzyl alcohol (BzOH) and Ethylene Glycol (EG). The birefringent filter tuning element consisted of three flat with parallel surfaces crystalline quartz plates placed inside the dye laser cavity at Brewster's angle as shown in Figure 7. A solid etalon which consisted of an uncoated, 1 mm thick quartz plate (20 mm in diameter) is also mounted in the laser cavity parallel to the output mirror and tuned by an electronically scanned galvanometer (General Scanning Inc., Model G124). Laser 1 is passively stabilized with a combination of the birefringent filter and solid etalon, and produced a linewidth of about 0.2 cm^{-1} at the Li 2s-2p resonance transition. The DCM dye laser when pumped by 5 W of the Ar^+ laser, produced a peak output power of about 500 mW.

Laser 2 excites LiNe molecules from the $2p^2\Pi$ to the $3s^2\Sigma^+$ molecular

FIGURE 7

Detailed schematic diagram of laser systems. B.F. is birefringent filter.

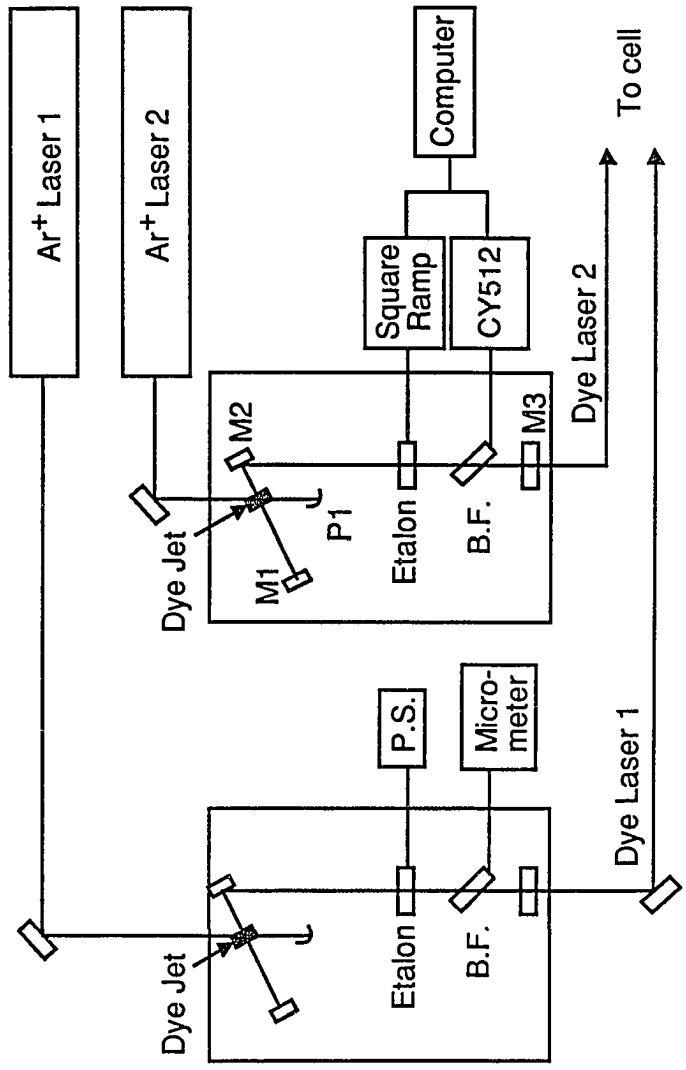

electronic states. Styril 9M laser dye (Lambda Physik) is used as the lasant in laser 2, which is pumped by an Ar^+ laser (Coherent, Innova 70-4). Two grams of Styril 9M were pre-mixed with 300 ml of Propylene Carbonate (PC) for 30 min then blended with 700 ml of EG. A Coherent 599 dye laser system is employed for laser 2 with an appropriate laser mirror set. Since a wavelength range of about 780 - 870 nm is required in this experiment, pushing the spectral range to the blue of the normal lasing spectral range of Styril 9M dye (720 - 900 nm) required the choice of a proper corresponding laser mirror set (see Table 1). By pumping with the 4 W Ar^+ laser, the dye laser produces a linearly polarized peak output of about 300 mW with a lasing spectral range of 780 - 870 nm. Since the laser is almost invisible to the eye, a fluorescence pad is used to work with the IR laser. The three plate birefringent filter and a solid etalon are placed inside the dye laser cavity for frequency scanning as shown in Figure 7. The uncoated quartz etalon is 1 mm thick and 20 mm diameter and is mounted on the galvanometer (General Scanning Inc. Model G124). The free-spectral range of the etalon is about 3.33 cm^{-1}.

A square-root of time ramp generator drives the galvanometer through a DC power supply (Kepco, Model CK36) to compensate for the θ^2 dependence of the shift of etalon transmission peaks with θ, where the θ is the angle between the normal to the etalon surface and the laser beam. The angle dependence of the frequency ν_m for the transmission maximum of m^{th} order [70] is

$$\nu_m = mC(1-\sin^2\theta/n^2)^{-0.5}/2nd$$

$$\simeq mC(1+\theta^2/2n^2)/2nd$$

$$\therefore \Delta\nu = \nu_m - \nu_0$$

TABLE 1

A mirror set for laser 2.

Mirror	Optical coating Range (nm)	Focal Length
Folding (M1)	680 - 810	75mm
High Reflection (M2)	660 - 810	50mm
Output (M3)		∞
Pump (M4)	453 - 532 350 - 365	75mm

$$\simeq \nu_0\theta^2/2n^2$$

where n: index of refraction

$\nu_0 = mC/2nd$

C: speed of light.

Since θ is varied up to about 4° in this experiment, the approximation $\sin^2\theta \simeq \theta^2$ is used. The starting angle is made slightly greater than 0° because reflection from the etalon at exactly 0° interferes with the laser operation. About 20 % walk-off losses due to laser reflection from the etalon surface and the shifting laser alignment is observed at the extreme of a 30 cm^{-1} scan. By varying the angle of the etalon and synchronously scanning with the birefringent filter, a 30 cm^{-1} smooth scan is achieved without etalon mode hops. Scans are sequenced with a 10.3 cm^{-1} overlap. The slope of the speed of the rotation of the etalon versus time is determined empirically.

The three plate birefringent filter in the laser 2 cavity is mechanically driven by a computer (Commodore, Vic-20) through a stepper motor controller (Cybernetic Micro systems. Inc., CY512). Backlash in the stepper motor (Rapidsyn Ind., Model 23c-6102A) and gearing is compensated for at each resetting of the starting frequency. The correction of the starting frequency of the birefringent filter and the slope of the speed of rotation of the etalon are important to achieving long sequences of overlapping scans with no etalon mode hops. Otherwise, there are mode hops which are produced because of the departure of the peak transmission of the etalon from the transmission maximum of the birefringent filter.

Plotting the micrometer reading versus the wavelength of the laser gives the conversion that determines the angle of rotation of the birefringent micrometer. The

angle of rotation is translated to the number of steps of the stepper motor and distributed linearly over a 30 cm^{-1} scan. Typically about 1,100 steps (depending on the region of the wavelength of the laser) of the stepper motor are made during the typically 160 seconds necessary to make a 30 cm^{-1} scan. About 300 cm^{-1} continuous scans are typically achieved without a mode hop which are monitored with a 0.5 cm^{-1} Fabry-Perot etalon and the other wavelength reference systems discussed in the following section. Since the Doppler broadening for LiNe is about 0.04 cm^{-1} at 310°K [70, 71], the resolution of this experiment is limited by the laser line width of 0.2 cm^{-1}.

E. WAVELENGTH REFERENCES

Since laser 1 excites the atoms to the 2p state, the intensity of fluorescence (671.0 nm) of the atomic Li 2p→2s transition confirms the laser wavelength. But for laser 2, a more complicated wavelength reference system is required.

As shown in Figure 8 the wavelength of the laser 2 output is monitored with three methods simultaneously. The first method is by measuring the transmitted intensity of a 0.5 cm^{-1} Fabry-Perot etalon (Gaertner Scientific Co.) as the laser frequency is scanned. A portion of the IR laser beam is passed through a 1.0026 cm (0.4987 cm^{-1} free spectral range) thick air spaced Fabry-Perot etalon. As the wavelength of laser 2 is changed, the intensity of the transmitted IR laser light

FIGURE 8

A schematic diagram of the wavelength measurement apparatus.

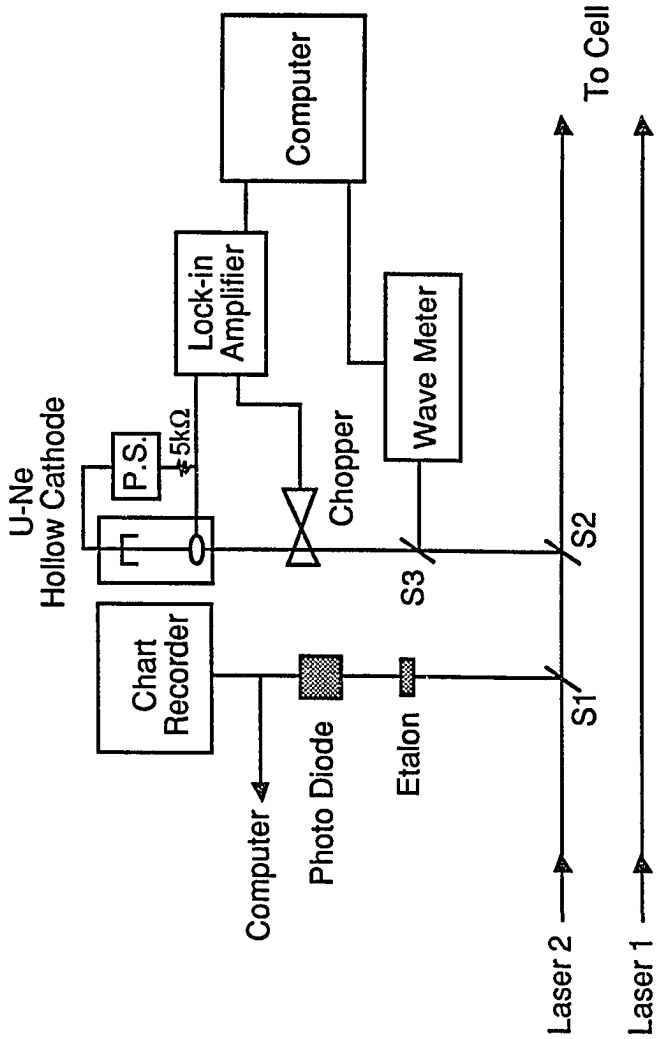

oscillates, with transmission maxima separated by the free spectral range. The intensity variation is detected by a calibrated power meter (Newport Research Co, Model 815) and is recorded on the chart recorder and a laboratory IBM compatible 80386 computer. Mode hops and mode competition are readily seen on the chart recorder and on the computer as irregular intensity variations.

To understand the origin of the mode hops, consider Figure 9, which shows the schematic curves of the transmittance of the birefringent filter and the intracavity etalon. The frequency selectable bandwidth of the birefringent filter is about 30 GHz. The linewidth and the free spectral range of the etalon are about 3 GHz and 100 GHz, respectively. When the peak transmittance scanning speed between the birefringent filter and the etalon do not correspond to each other, there are modes hops or mode competition. If the peak transmittance of the birefringent filter is between those of the etalon, there is mode competition of the laser output. But, if the peak transmittance of the etalon jumps from one to another, there is a mode hop of 100 GHz.

The second wavelength monitor is an uranium-neon hollow cathode lamp. The spectrum of uranium and a carrier gas of neon is obtained from a commercial hollow cathode discharge tube manufactured by Westinghouse Electric Corporation. A fraction the IR laser is passed through the beam splitter (S3), and is directed coaxially into the uranium cathode. Less than 4 % of the laser 2 power shines on the hollow cathode to get enough reference lines without considerably disturbing the laser power to the cell. The alignment of the beam is not critical, and focusing was not necessary. The laser is chopped at a frequency of 16 Hz. The optogalvanic signal

FIGURE 9

Qualitative transmission graph of a three-plate birefringent filter and etalon combination.

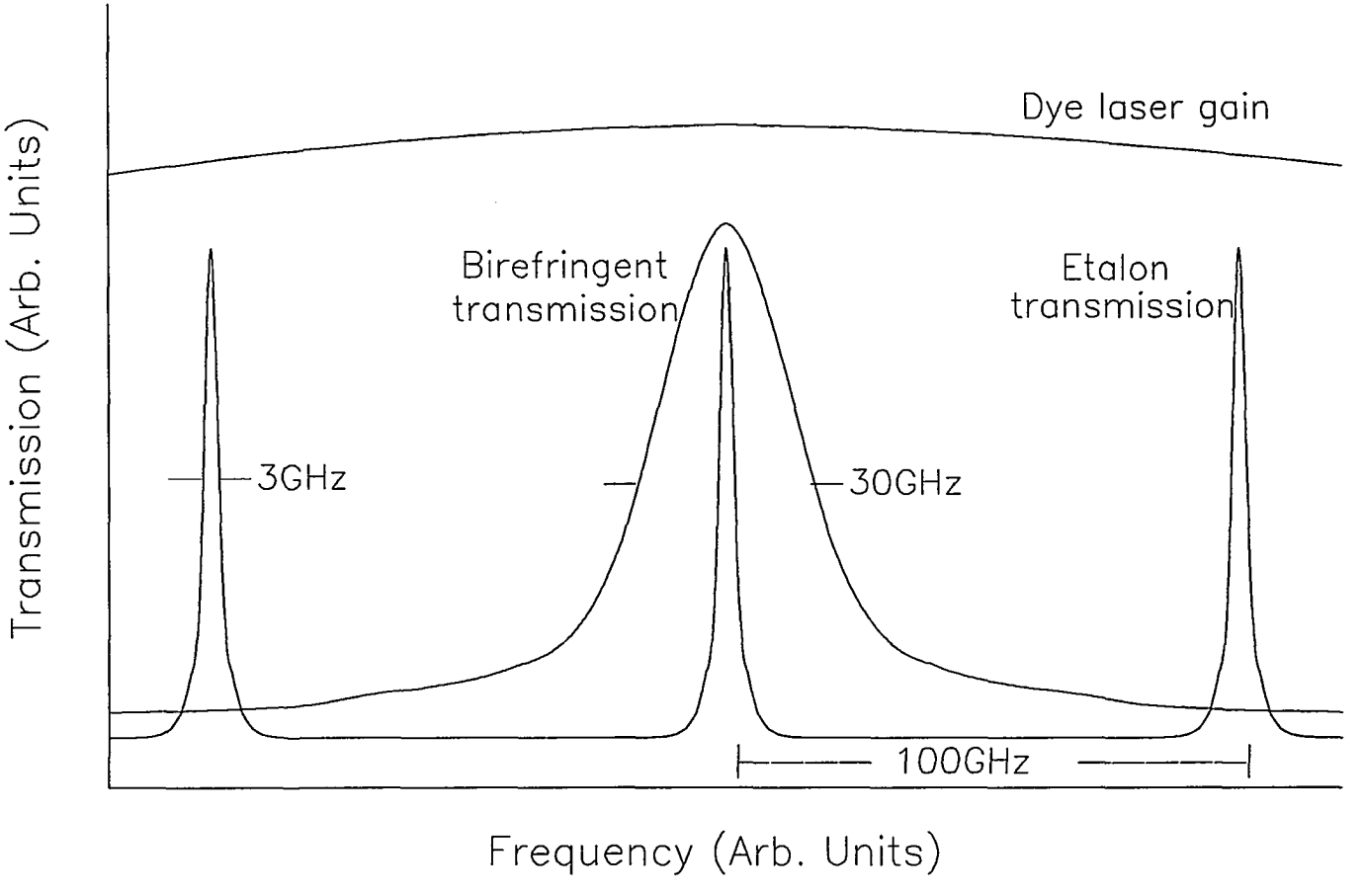

from the U-cathode is collected across the lamp ballast resistor (5 KΩ) with the lock-in amplifier tuned to chopping frequency. Even though the cathode has a 25 mA maximum operating current, 15 mA is applied to the cathode to obtain the best signal to noise ratio. When an atomic species in the discharge is irradiated with photons whose wavelength corresponds to an electronic transition, a substantial voltage change is produced. These voltage signals are due to absorption by the discharge species. The signal from the lock-in is displayed on the computer and is compared with an atlas of the spectrum of uranium and neon [72]. Most neon discharge signals are much stronger than the uranium ones. This spectrum serves as an absolute frequency scale with which to calibrate the third wavelength reference system, a Fizeau wavemeter.

The wavemeter (Model 100F, Lasertechnics Inc.) serves to continuously monitor the frequency of laser 2. To use this instrument, the calibration process is performed. Six lines, which are measured in units of vacuum wavenumbers by the U-Ne hollow cathod lamp, are used as absolute wavelength sources. From this calibration, an accuracy of ± 0.02 cm^{-1} in the reading of the wavemeter is achieved as shown in Table 2. The accuracy of the reading of the calibrated wavemeter is continuously monitored and is compared with the spectrum of the U-Ne hollow cathod output throughout this experiment.

TABLE 2

Comparison between U-Ne cathode line [72] and measured line positions. The transition energies are measured by the wavemeter. All units are in cm^{-1}.

#	U-Ne Cathode line	Measured Line (After Calibration)
1	11831.03	11831.01
2	11837.54	11837.52
3	12092.80	12092.78
4	12094.31	12094.31
5	12104.12	12104.15
6	12100.20	12100.19

F. SIGNAL DETECTION SYSTEM

(1) FOR THE EMISSION SPECTRUM OF THE $3s^2\Sigma^+ \rightarrow 2s^2\Sigma^+$ TRANSITION

The emission spectrum around 396 nm was measured with a 0.3 m monochromator (GCA/Mcpherson Inst. Model 700). This emission is considered to be a LiNe molecular emission in the bound-continuum $3s^2\Sigma^+ \rightarrow 2s^2\Sigma^+$ band [73 - 75] and serves as the signal of absorption on a $3s^2\Sigma^+ \leftarrow 2p^2\Pi$ molecular transition. Figure 10 shows a schematic diagram of the apparatus used in the measurement of a spectral profile of this transition. Laser 1 is tuned to the 2s → 2p atomic transition (671.0 nm) and laser 2 to the 2p → 3s atomic transition (812.8 nm). Laser 1 and 2 are very closely overlapped while passing through the Li cell. The temperature of the ^{6}Li boat is 620°K, and the pressure of ^{20}Ne is 50 torr. The emission of the $3s^2\Sigma^+ \rightarrow 2s^2\Sigma^+$ transition is collected by a quartz lens and focused to the photomultiplier (EMI, Model 9817B) through a 0.3 m monochromator. Two 1 mm thick color filters (BG39 and BG3 from Schott Glass Tech. Inc.) which pass light around 390±(30) nm are in front of the monochromator to eliminate background light due to laser scattering and room light. The signal from the photomultiplier is recorded on the chart recorder through an electrometer (Model 610c, Keithley Inst.) as shown in Figure 11. There is a peak intensity at about 396 nm and the featureless molecular emission spectrum has a full width at half maximum of 13 nm. Transitions from high lying Li levels were also observed. These transitions around 396nm from high lying Li atomic levels to 2p state are listed in Table 3 [76]. It appears that energy pooling [77-79] processes

FIGURE 10

A schematic diagram of the apparatus for emission spectrum measurements of the $3s^2\Sigma^+ \rightarrow 2s^2\Sigma^+$ transition.

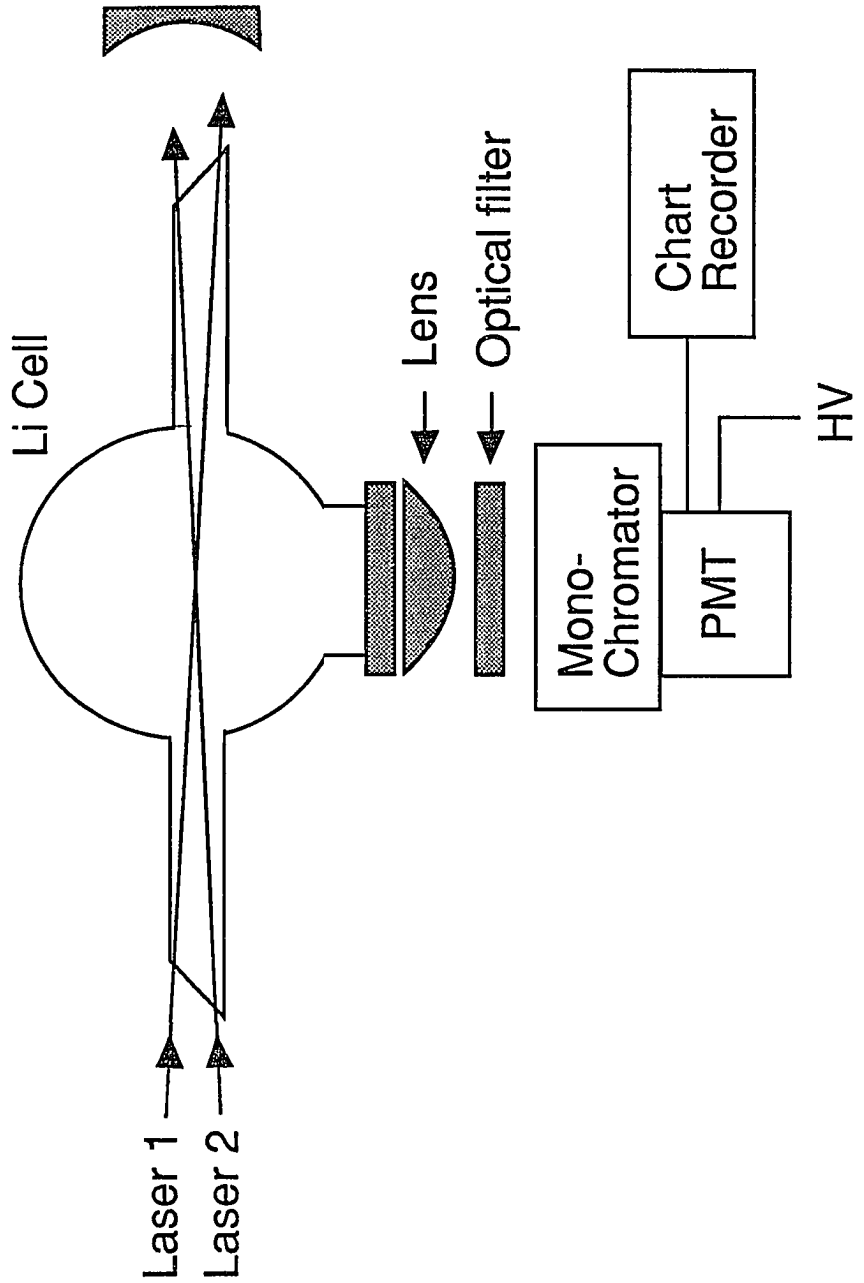

FIGURE 11

Emission spectrum of the $3s^2\Sigma^+ \rightarrow 2s^2\Sigma^+$ transition in $^7Li^{20}Ne$.

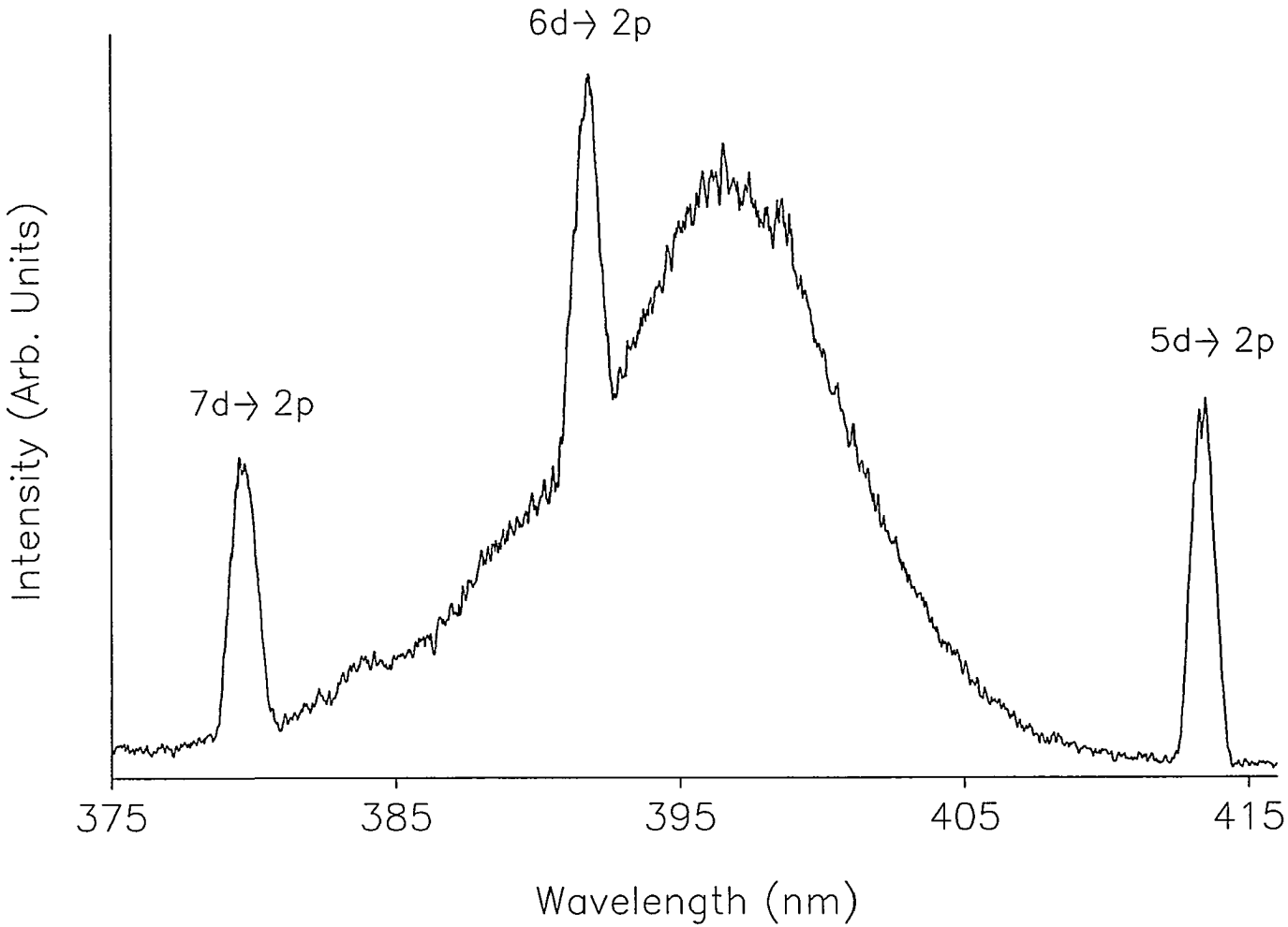

TABLE 3

Observed atomic transitions in the vicinity of the LiNe molecular $3s^2\Sigma^+ \rightarrow 2s^2\Sigma^+$ emission band [76].

Transition	Energy (cm^{-1})
8s → 2p	26682.84
7s → 2p	26063.64
6s → 2p	25083.81
7d → 2p	26342.24
6d → 2p	25533.48
5d → 2p	24190.64

in atomic Li are responsible for the production of the emission lines. In the process, 3s and 2p Li atoms or two excited Li(3s) atoms can collide, leaving one atom in a higher excited atomic state. When laser 1 and laser 2 is tuned off resonance, observed intensity of transitions from high lying Li states disappear; this supports the above interpretation of the observed transition.

(2) FOR THE ABSORPTION SIGNAL ON THE $3s^2\Sigma^+ \leftarrow 2p^2\Pi$ MOLECULAR TRANSITION

Figure 12 shows a schematic diagram of the absorption signal detection system. Laser 1 is fixed on the 2s-2p resonance transition, while laser 2 is scanned from 11680 cm^{-1} to 12400 cm^{-1}. Laser 1 and 2 are also tightly overlapped and focused with 100 cm focal length lenses to the center of the cell. A 12.7 cm focal length reflection mirror (Janos Tech. Inc.) coated with Cr-Au provides an additional laser pass. The signal is collected with a 10 cm focal length lens and focused on a photon counting mode photomultiplier (Hammamatsu, R464S). The photomultiplier has a 300 nm - 650 nm spectral response and is operated at 1000 volt anode to biakali cathode.

Several color filters (two BG36, three BG3, and one BG40) are used in front of the photomultiplier. Those filters are 1 mm thick and purchased from the Schott Glass Tech. Inc. This combination of color filters is very effective in cutting off the background light due to strong fluorescence (671.0 nm, 2p-2s atomic transition), laser

FIGURE 12

A schematic diagram of the signal detection system.

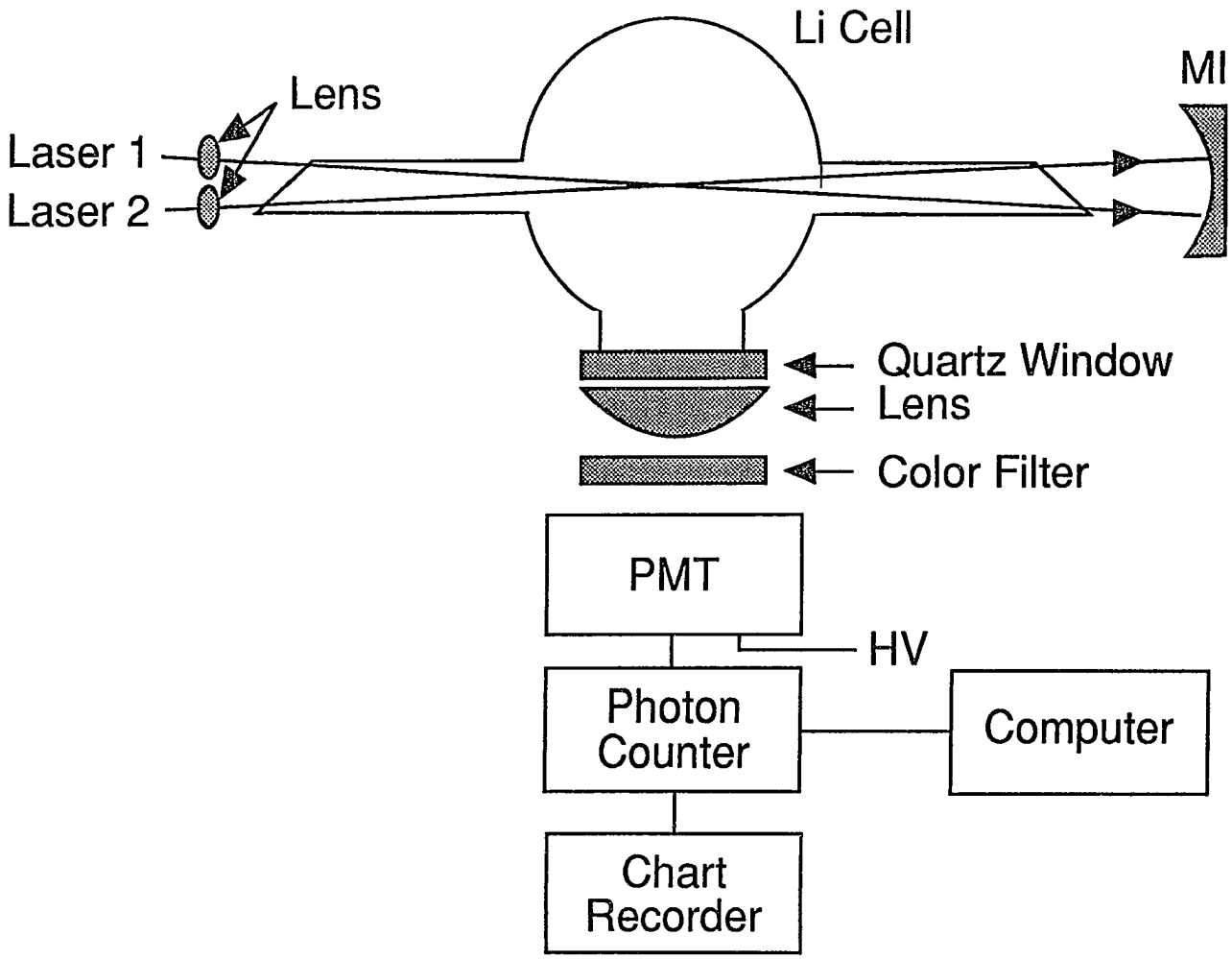

scattering, and room light. Only light around 390($\pm$30) nm can pass through the color filter combination.

G. DATA ACQUISITION SYSTEM

The data acquisition system basically consists of a 20 MHz microcomputer (32 bit) and a chart recorder. The computer uses a data acquisition and control interface board (Metra Byte Co., DAS20) that has several high speed analog/digital I/O channels. Each channel has an input voltage range of $\pm$10 volt with 4.8 mV resolution and about 8.5 μs A/D conversion time.

In this experiment, three I/O channels of the DAS20 are used to collect data from the lock-in amplifier, the power meter for the 0.5 cm^{-1} Fabry-Perot etalon, and the photon-counter. The fourth data input to the computer is the output from the wavemeter. The wavemeter communicates with the computer through an RS-232 port addressed using a simple Basic program. Combining this Basic program and the DAS20 control program, data from the four sources is stored on the disk and displayed on the screen as laser 2 is scanned. The data acquisition is synchronized with the wavemeter output at a sampling rate of 10 Hz. As soon as the output from the wavemeter is read, the analog input data through the other three channels is converted to digital form. The wavemeter output signal is considered to be an x-coordinate and three channels of input data are considered to be y-coordinates in real

time. Each data run is about 160 seconds. Since the sampling rate is 10 Hz, the spectral resolution due to the sampling rate is less than 0.02 cm^{-1}, which is the same as the accuracy of the wavemeter as discussed before. Since the hollow cathode signal is also recorded, it is possible to compare the U-Ne emission spectrum and the wavemeter reading continuously. While the data is displayed on the screen in real time, a mode hop or mode competition is easily seen. Re-scanning after adjustment of the starting position of the birefringent-filter micrometer or the slope of rotation of the intracavity etalon normally eliminated the mode hop. The output signal from the photon-counter and the 0.5 cm^{-1} Fabry-Perot etalon signal are also recorded on the chart recorder for convenience in the initial rotational analysis of the spectrum. The intensity change of the peak 0.5 cm^{-1} Fabry-Perot etalon signal over the 30 cm^{-1} segment gives an idea of the intensity change in the laser because of walk-off losses which are observed to be about 20 %. The line positions of the spectrum are obtained from the computer data files.

CHAPTER 4

RESULTS

A. THE 3s ← 2p ATOMIC TRANSITION

When laser 2 is tuned to the atomic Li 3s ← 2p transition, the 0.34 cm^{-1} fine structure splitting [76] is clearly resolved, as shown as Figure 13. The stronger line at 12302.12 cm^{-1} is the $2P_{3/2} \rightarrow 3S_{1/2}$ transition and the weaker line at 12302.46 cm^{-1} is the $2P_{1/2} \rightarrow 3S_{1/2}$ transition. The intensity ratio of the two lines is about 2:1 which corresponds to the number of magnetic sublevels of $2^2P_{3/2}$ and $2^2P_{1/2}$. A full width at half maximum of about 0.15 cm^{-1} is measured for the atomic transition.

The signal is detected through the $3s^2\Sigma^+ \leftarrow 2p^2\Pi$ excimer emission band at 396 nm. Since the atomic transition signal is too strong for the photomultiplier tube, a 10^{-4} attenuator is used on laser 1. Therefore the very weak molecular lines that are around the atomic line can not be distinguished on this scale.

FIGURE 13

Measured absorption spectrum of the atomic 3s←2p transition.

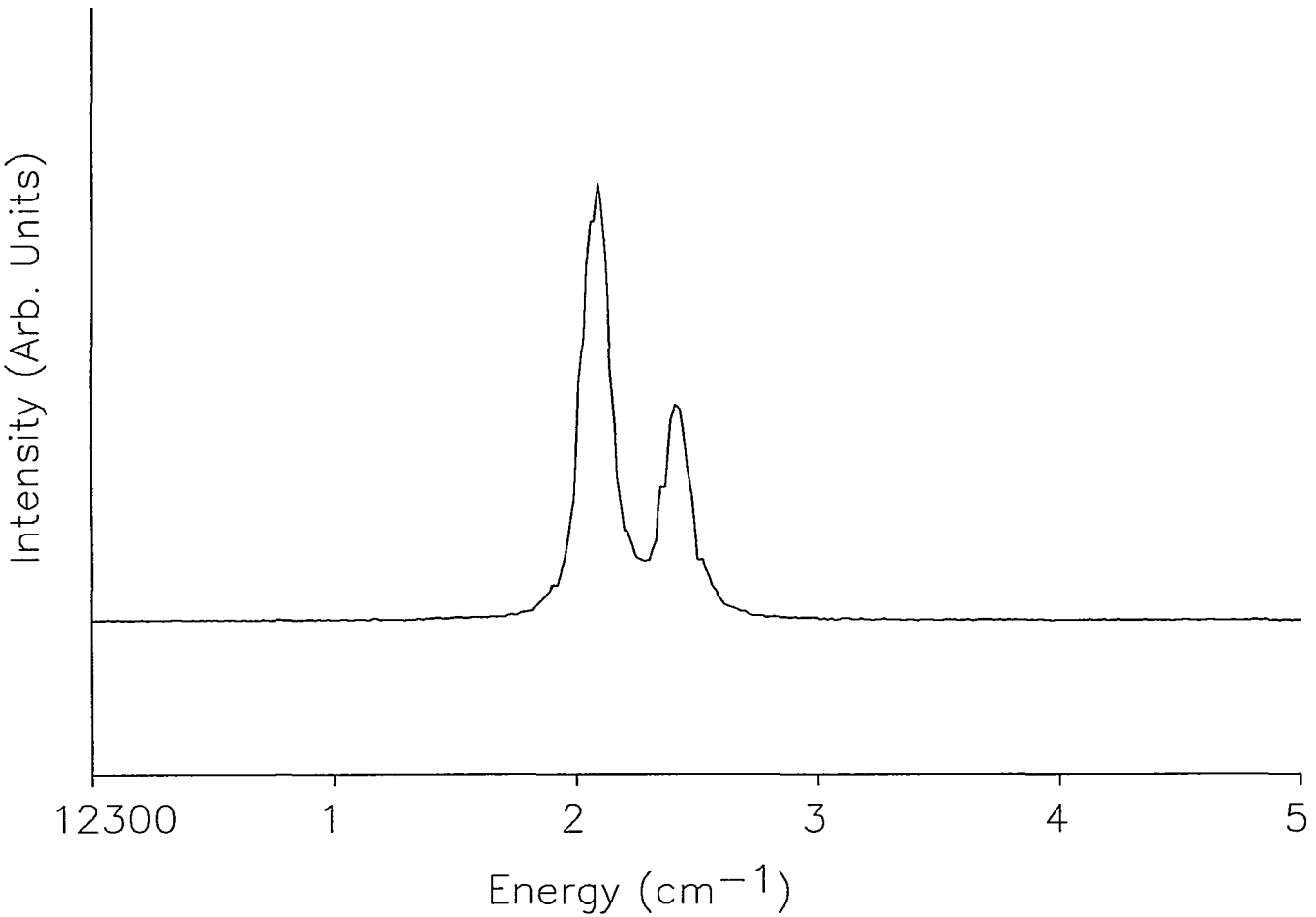

B. STRUCTURE OF RO-VIBRATIONAL BANDS

In scanning laser 2 from 11680 cm^{-1} to 12400 cm^{-1}, well resolved and intense rotation - vibration bands are observed. Thirteen ro-vibrational transitions from the lower $2p^2\Pi(v''=0, 1, 2 \text{ and } 3)$ to the upper $3s^2\Sigma^+(v'=0, 1, 2, 3, 4 \text{ and } 5)$ electronic state have been observed. The peak photon count intensity of the strongest transitions lines in the band is about 1100 kHz with less than 10 kHz background noise. The signal is translated to the photon count mode as discussed previously. Most individual molecular line photon count intensities are 20 - 1000 kHz, which is 10^{-5} - 10^{-3} of that of the Li atomic 3s←2p transition. The intensity of the molecular signal is strongly dependent on both the density of Li(2p) atoms and Ne pressure in the cell. As the density of Li(2p) atoms or the Ne pressure is reduced, a given band becomes considerably weaker, but the overall shape of the rovibrational band is almost identical. The molecular line width is very weakly dependent on the Ne pressure in the 10-110 torr range. Figure 14 shows the line widths for Q(8) and Q(10) of the $^6Li^{20}Ne(v''=0 - v'=0)$ increase slightly as a function of the Ne pressure. However, this change is within the size of the experimental error. Also, no shift of the line positions with Ne pressure is observed.

Since the selection rule for the total angular momentum N neglecting the spin is $\Delta N = 0, \pm 1$ in Hund's case (b), each band consists of three strong main P ($\Delta N = -1$), Q ($\Delta N = 0$) and R ($\Delta N = +1$) branches [55 - 57]. When considering the spin, the transition $\Delta N = 0, \pm 1$, and $\Delta J = 0, \pm 1$ with $\Delta N = \Delta J$ appears as the main branch where $J = N + S, (N + S - 1), \ldots, |N - S|$, and N is the total angular

FIGURE 14

The line widths for the Q(8) and Q(10) transitions of $^{6}Li^{20}Ne$ ($v''=0 - v'=0$) as a function of Ne pressure.

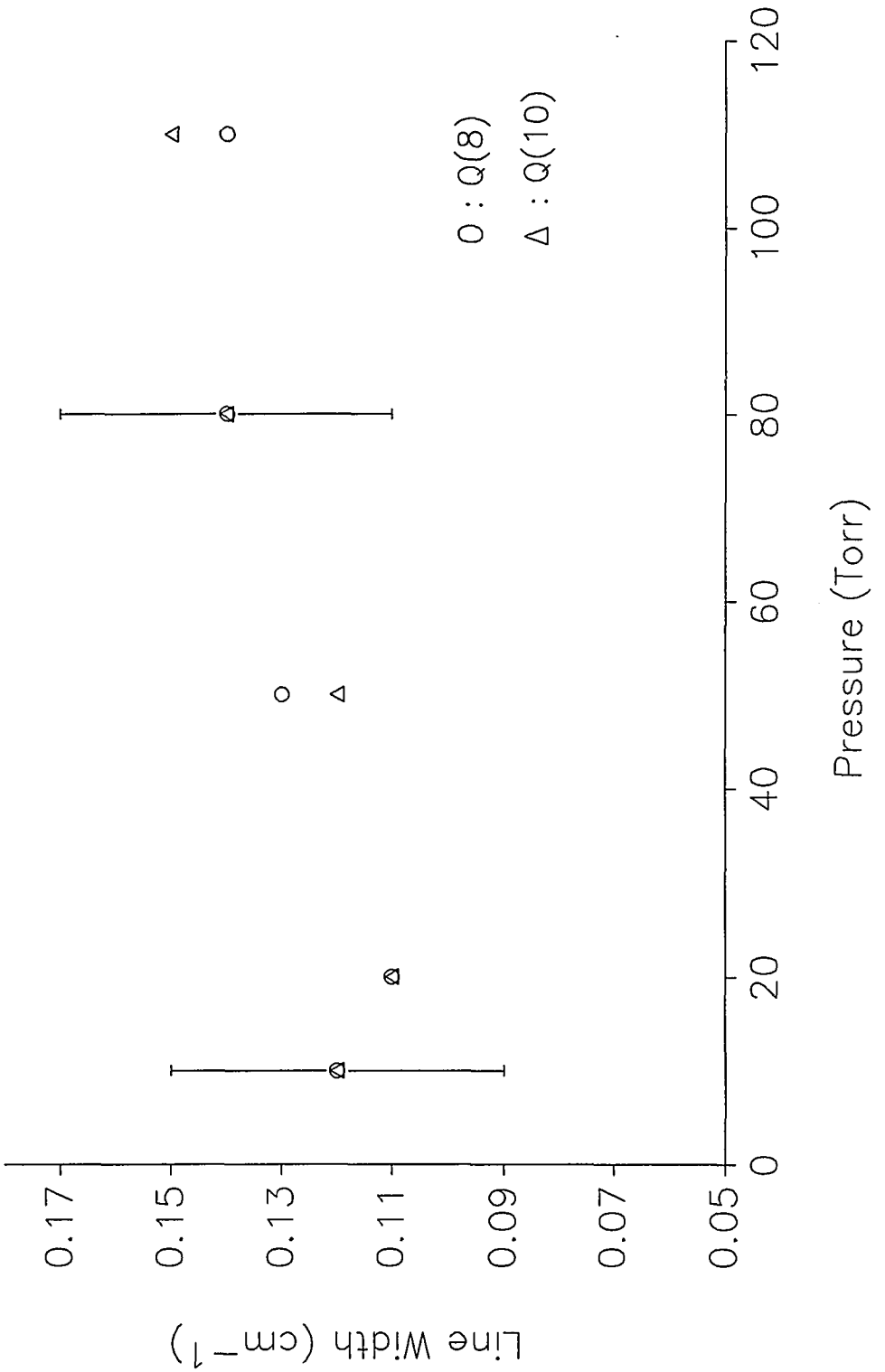

momentum quantum number apart from spin, $N = \Lambda, \Lambda + 1, \Lambda + 2, \ldots$. If $\Lambda = 0$ in the electronic state, the angular momentum N is identical with the rotational angular momentum R.

Spin-orbit splitting is observed in $2p^2\Pi$ ($v'' = 0$) of both isotopes. A more detailed discussion of the spin-orbit interaction is found in a later section. Each band is blue degraded and is spread over a range of 20 - 80 cm^{-1}. There is a band head in the P-branch, generally. Due to the rotational predissociation of the $2p^2\Pi$ state, each band is cut off abruptly at a certain angular quantum number N".

Figure 15 shows a full 30 cm^{-1} scan of the band head region of the (0-1) band of $^7Li^{20}Ne$. The upper signal of the figure is the spectrum of the U-Ne hollow cathode. The two peaks are Ne discharge signals of the hollow cathode at 12094.31 cm^{-1} and 12104.15 cm^{-1} [72].

The middle spectrum shows the variation in the transmitted intensity of the 0.4987 cm^{-1} Fabry-Perot etalon. Since the difference between two peaks is 0.4987 cm^{-1}, it also gives information on the laser 2 scan concerning relative wavelength determination and linearity. Mode hops at the free spectral range (FSR) of the intracavity etalon (3.33 cm^{-1}) are also readily detected. The signal also shows about 30 % walk-off losses at the extreme of the scan due to the rotation of the etalon in the laser 2 cavity. Since each scan is overlaped 10.3 cm^{-1} with the previous and next scan, a laser power variation of less than about 20 % is considered in the spectrum analysis.

The lower spectrum is the $3s^2\Sigma^+ \leftarrow 2p^2\Pi$ molecular absorption spectrum, as monitored through the LiNe $3s^2\Sigma^+ \rightarrow 2s^2\Sigma^+$ emission. A well developed (0-1) band is

FIGURE 15

Typical 30 cm^{-1} scan around the band head region of the (0-1) band of $^{7}Li^{20}Ne$.

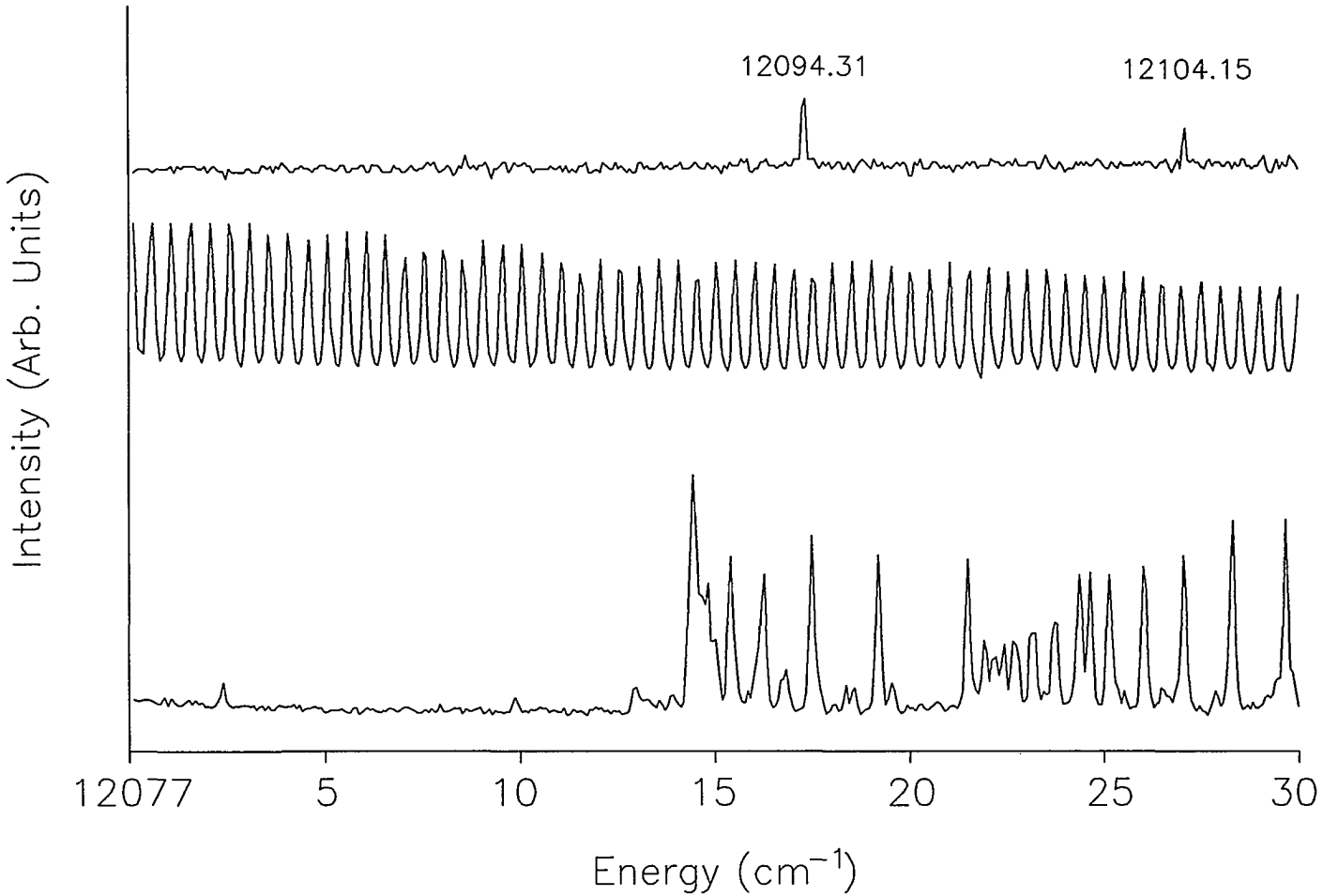

shown with a band head on the P-branch. At lower J, the spin-orbit splitting of the $2p^2\Pi(v''=0)$ state is also clearly shown in the spectrum. The band is blue degraded.

These spectra are displayed in real-time and stored on the hard disk. For convenience, the molecular spectrum and Fabry-Perot etalon output are also recorded on a chart recorder and then are merged into a continuous spectrum. Figure 16 shows the molecular spectrum combined into three adjacent scans. The spectrum is a 60 cm^{-1} segment of the (1-0) band of $^7Li^{20}Ne$. Using a long strip of paper, the branches can be identified by initial rotational analysis of the spectrum. Absolute line positions are obtained from the computer data files with an accuracy of ± 0.15 cm^{-1} .

Figure 17 and 18 show the $^6Li^{20}Ne$ and $^7Li^{20}Ne$ band origin region of the $3s^2\Sigma^+$ $(v'=0) \leftarrow 2p^2\Pi$ $(v''=0)$ transition, respectively. Each has a band head at $N'' = 7$ in the P-branch. It shows that the band origin of the $^7Li^{20}Ne$ is 1.59 cm^{-1} red-shifted from that of $^6Li^{20}Ne$. There is also a considerablely weaker isotope band about 0.05 times the main band intensity and about 1 cm^{-1} red-shifted from the main band. These isotope bands are attributed to the natural abundances of ^{20}Ne and ^{22}Ne [80]. Since the intensity of these isotope bands is so weak, they can not be analyzed independently, but several lines are identified using the isotope relation, which confirmed the source of the very weak lines.

In the $3s^2\Sigma^+ \leftarrow 2p^2\Pi$ transition, the three main R, Q and P branches each have a lowest $N'' = 1$. However, a lowest N" for each branch (also R(2) for $^7Li^{20}Ne$) is not assigned due either to the weak intensity or to an abundance of overlapping lines.

FIGURE 16

Typical absorption spectrum of three 30 cm^{-1} scans combined. This spectrum is taken in the band head region of the (1-0) band of $^{7}Li^{20}Ne$.

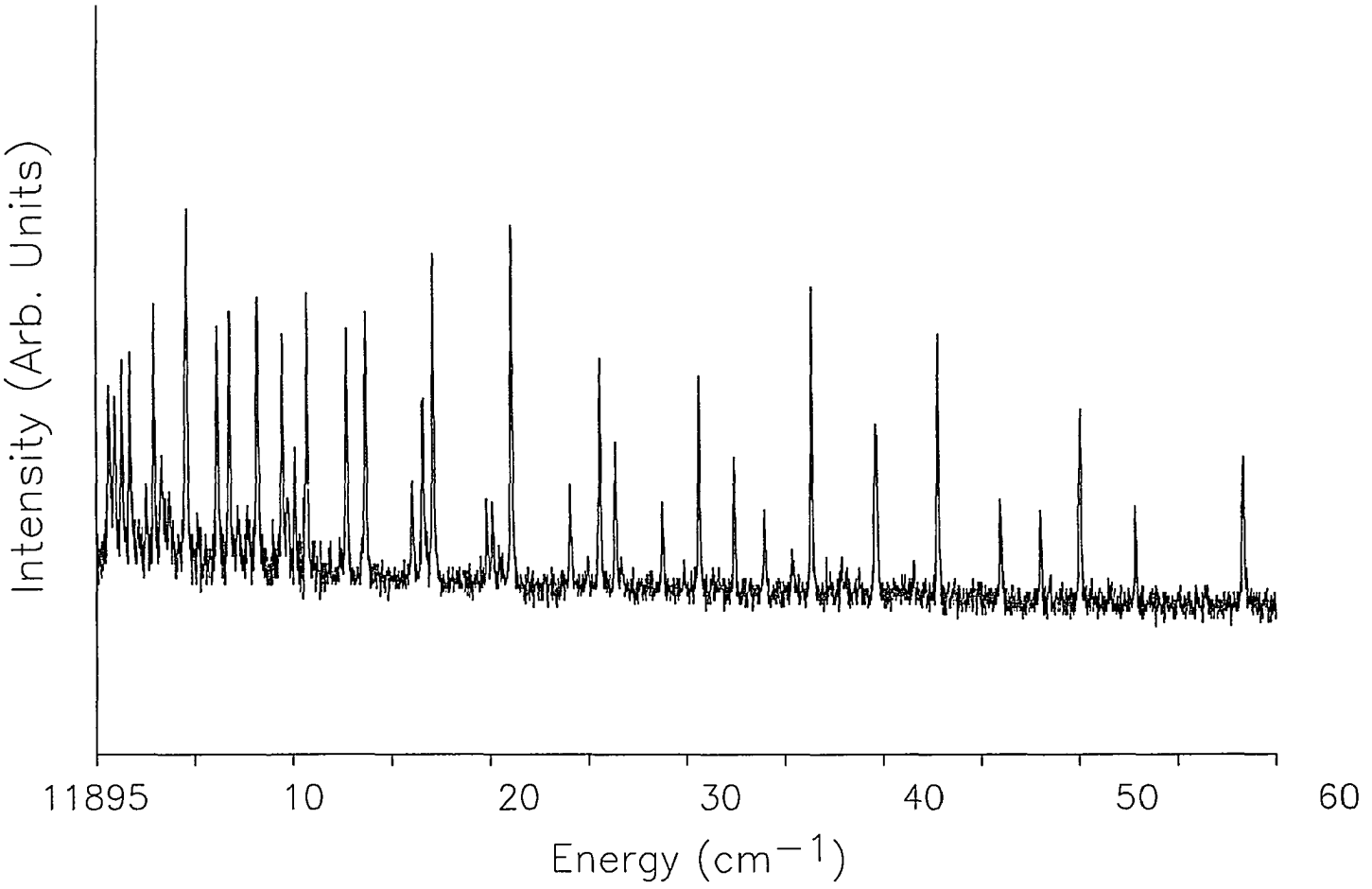

FIGURE 17

Assignments of the lines around the band head of the (0-0) band of $^{6}Li^{20}Ne$.

Note the fine structure splitting of the low N lines.

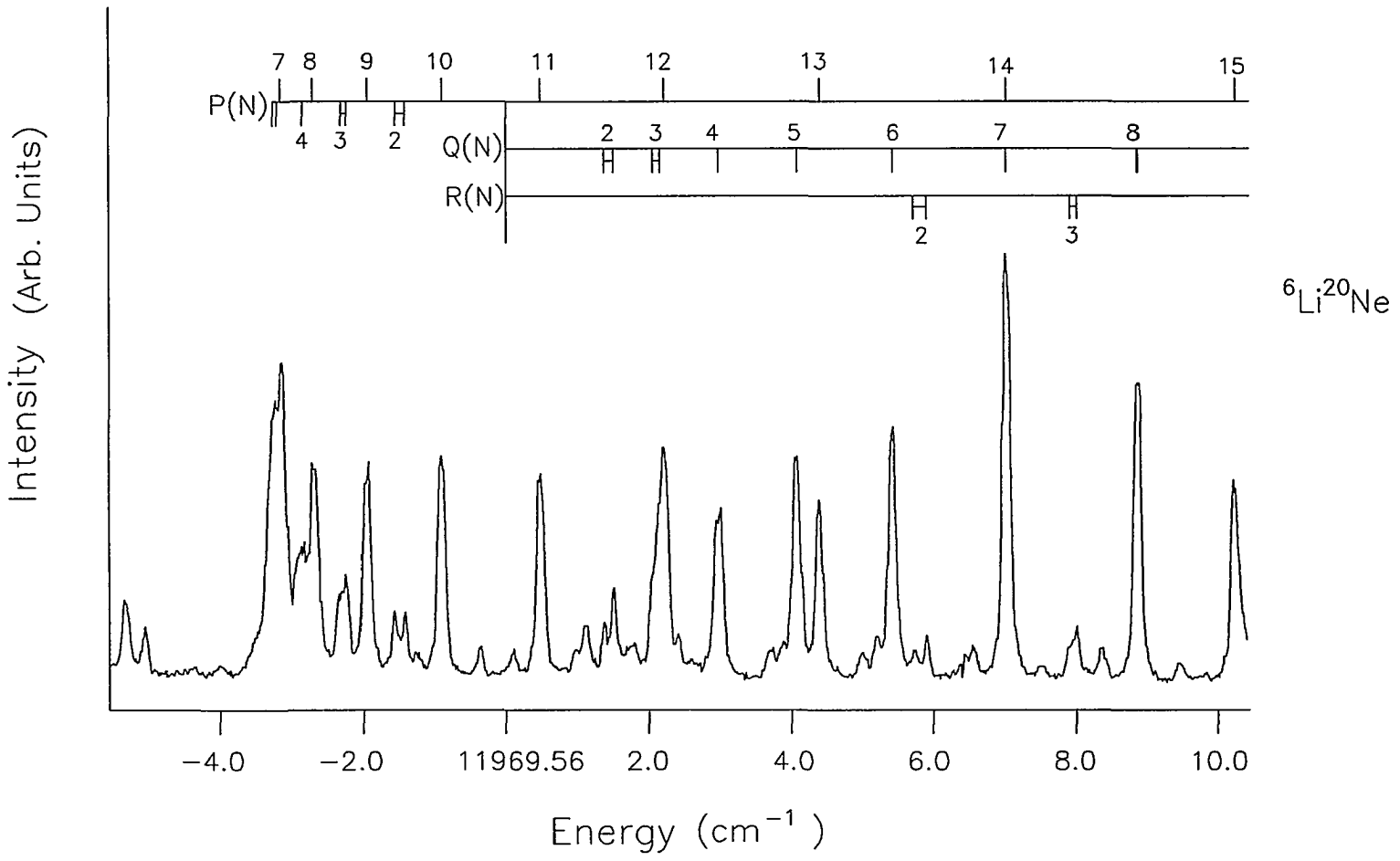

FIGURE 18

Assignments of the lines around the band head of the (0-0) band of $^{7}Li^{20}Ne$.

Note the fine structure splitting of the low N lines.

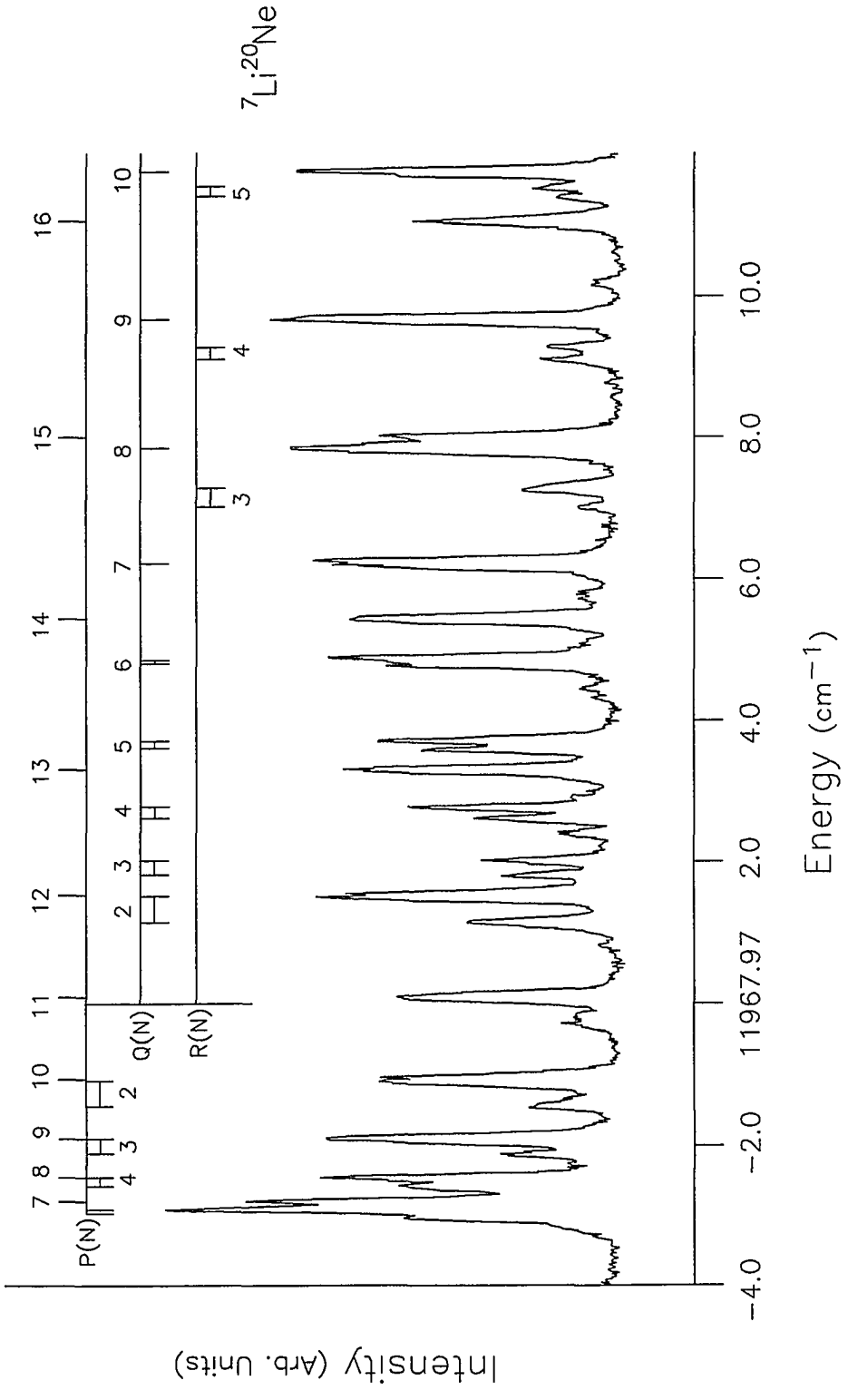

CHAPTER 5

SPECTRAL ANALYSIS

A. OVERVIEW

The total energy of the molecule (neglecting internal magnetic interactions and in the absence of external fields) consists of the potential and kinetic energies of the electrons and those of the nuclei. For fixed nuclei, the electronic energy (potential plus kinetic energy) will depend on the internuclear distance R. The excess energy of a non-rotating molecule over the minimum electronic energy E_e is considered as vibrational energy E_v and rotational energy E_r. Thus the total energy E of the molecule is, to a very good approximation, the sum of three parts

$$E = E_e + E_v + E_r \qquad (5\text{-}1)$$

Using the customary mechanical vibrational constants of visible spectroscopy, the vibrational energy values in cm^{-1} of the anharmonic oscillator are given by [55, 67]

$$G(v) = \omega_e(v+\frac{1}{2}) - \omega_e x_e(v+\frac{1}{2})^2 + \omega_e y_e(v+\frac{1}{2})^3 + \cdots \qquad (5\text{-}2)$$

Here v is the vibrational quantum number and the constants are $\omega_e \gg \omega_e x_e \gg \omega_e y_e$.

The rotational energy levels are given [55, 67] in cm^{-1} by

$$F_v(N) = B_v[N(N+1) - \Lambda^2] - D_v[N(N+1) - \Lambda^2]^2 + H_v[N(N+1) - \Lambda^2]^3 + \cdots \qquad (5\text{-}3)$$

B_v is the rotational constant in the vibrational state v and is given by [55]

$$B_v = B_e - \alpha_e(v + \frac{1}{2}) + \gamma_e(v + \frac{1}{2})^2 - \cdots \qquad (5\text{-}4)$$

where B_e, α_e and γ_e are constants. D_v is the rotational distortion constant and is considered to be the centrifugal term. D_v is given [55] by

$$D_v = D_e + \beta_e(v + \frac{1}{2}) + \cdots \qquad (5\text{-}5)$$

where D_e and β_e are constants.

The rotation - vibration energies may be generally described by

$$T(v,N) = G(v) + F_v(N)$$
$$= \omega_e(v+\tfrac{1}{2}) - \omega_e x_e(v+\tfrac{1}{2})^2 + \omega_e y_e(v+\tfrac{1}{2})^3 - \cdots$$
$$+ B_v[N(N+1) - \Lambda^2] - D_v[N(N+1) - \Lambda^2]^2$$
$$+ H_v[N(N+1) - \Lambda^2]^3 - \cdots \qquad (5\text{-}6)$$

In the following two sections, details of the rotational and vibrational analysis of the data are described. The spin-orbit splitting in the $2p^2\Pi(v=0)$ state is discussed in section D. The mass dependence on the spectra and associated constants are obtained and presented in the section E. Details of the long-range and inverted perturbation analysis employed in analyzing the experimental data, are provided in the final two sections, respectively.

B. ROTATIONAL

As in the case of rotation - vibration spectra, the measured term values for each band are fit to the general form

$$\nu = T(v', N') - T(v'', N'') \qquad (5\text{-}7)$$

where T(v',N') and T(v",N") are the ro-vibrational energies of the upper $3s^2\Sigma^+$ and lower $2p^2\Pi$ state. For a specific vibrational transition, the quantity $\nu_o = \nu_e + \nu_v$ is

constant, while ν_r is variable and depends on the rotational quantum number N. Then, equation (5-7) can be expressed as

$$\nu = \nu_o + F'(N') - F''(N'') \qquad (5\text{-}8)$$

where F'(N') and F"(N") are the rotational terms of the upper and lower state, respectively. ν_o is also called the band origin. According to the selection rule $\Delta N = 0, \pm 1$, three main branches are expected according to the following formulas

$$R(N) = \nu_o + F'_v(N+1) - F''_v(N) \qquad (5\text{-}9)$$

$$Q(N) = \nu_o + F'_v(N) - F''_v(N) \qquad (5\text{-}10)$$

$$P(N) = \nu_o + F'_v(N-1) - F''_v(N) \qquad (5\text{-}11)$$

Because $\Lambda' = 0$ for the $3s^2\Sigma^+$ state and $\Lambda'' = 1$ for the $2p^2\Pi$ state, branches start at R(1), Q(1) and P(1). As shown in Figures 17 and 18 the three series of lines, whose separations change regularly, are blue degraded. The P branch is red degraded initially then turns around. The turning point is called a band head.

The P and R branches can be represented by a single formula [55]

$$\begin{aligned}\nu = \nu_o &+ [B'm(m+1) - D'\{m(m+1)\}^2 + \cdots] \\ &- [B''\{m(m-1) - 1\} - D''\{m(m-1) - 1\}^2 + \cdots]\end{aligned} \qquad (5\text{-}12)$$

where m = -N for the P branch and m = N + 1 for the R branch. The estimated m value at the band head is obtained by putting $d\nu/dm = 0$ and neglecting the distortion terms. This gives

$$m_h \cong - \frac{B'_v + B''_v}{2\,(B'_v - B''_v)} \qquad (5\text{-}13)$$

Therefore, if B' - B" > 0 then, the band head is formed in the P branch and the internuclear distance in the upper state is less than that in the lower. Conversely, if $B'_v \approx B''_v$, the band head could appear in the R branch depending on the size of the distortion terms.

The six combination relations of the three branches are as follows [55];

$$R(N) - Q(N) = F'_v(N+1) - F'_v(N) = \Delta_1 F'(N) \qquad (5\text{-}14)$$

$$Q(N+1) - P(N+1) = F'_v(N+1) - F'_v(N) = \Delta_1 F'(N) \qquad (5\text{-}15)$$

$$R(N) - Q(N+1) = F''_v(N+1) - F''_v(N) = \Delta_1 F''(N) \qquad (5\text{-}16)$$

$$Q(N) - P(N+1) = F''_v(N+1) - F''_v(N) = \Delta_1 F''(N) \qquad (5\text{-}17)$$

$$R(N) - P(N) = F'_v(N+1) - F'_v(N-1) = \Delta_2 F'(N) \qquad (5\text{-}18)$$

$$R(N-1) - P(N+1) = F''_v(N+1) - F''_v(N-1) = \Delta_2 F''(N) \qquad (5\text{-}19)$$

Equations (5-14, 15, 16, and 17) are called the first combination differences. If

equation (5-3), including higher order distortion terms, is substituted into these equations, the result obtained is

$$\begin{aligned}\Delta_1 F(N) &= F_v(N+1) - F_v(N) \\ &= [2B_v + 4D_v\Lambda^2 + 6H_v\Lambda^4](N+1) \\ &\quad + [-4D_v + H_v(2 - 12\Lambda^2)](N+1)^3 \\ &\quad + 6H_v(N+1)^5 \end{aligned} \tag{5-20}$$

Similarly, equation (5-18 and 19) are called the second combination differences and yield

$$\begin{aligned}\Delta_2 F(N) &= F_v(N+1) - F_v(N-1) \\ &= [4B_v + D_v(8\Lambda^2 - 6) + H_v(12\Lambda^4 - 18\Lambda^2 + \tfrac{27}{4})](N+\tfrac{1}{2}) \\ &\quad + [-8D_v + H_v(34 - 24\Lambda^2)](N+\tfrac{1}{2})^3 \\ &\quad + 12H_v(N+\tfrac{1}{2})^5 \end{aligned} \tag{5-21}$$

Assignments of the quantum number N are made through the first and second combination differences. For initial analysis, the combination differences of the peak of the molecular lines are marked with a pencil on a long strip of paper. Since $B_v \gg D_v \gg H_v$, the spaces between the adjacent pencil marks are approximately constant (2B for the first and 4B for second combinations). However, as N is extrapolated to zero, the combination differences become about 2B in both combinations. This allows the absolute N-numbering of the branches to be made. Assignments meet all the conditions of six combination differences. The final line position data is obtained

from the computer data files. The total experimental error of the line positions has been estimated to be about 0.2 cm^{-1}. A list of the identified line positions is provided in Appendix 1. Once absolute line positions are determined equations (5-20 and 21) are used with the help of a computer program to obtain rotational constants B_v, D_v and H_v. $\Delta_1F(N)/(N+1)$ and $\Delta_2F(N)/(N+1/2)$ are nearly linear functions of $(N+1)^2$ and $(N+1/2)^2$, respectively. The data are fitted to a quadratic function with a least squared fitting method to get the coefficients. In this fitting procedure [81], equally weightted data and estimated experimental errors are used. The coefficients and errors of the function can be related to rotational constants B_v, D_v and H_v, and error of each by comparing with equations (5-20 and 21). More discussion of the results of this fitting procedure is provided later.

Figure 19 shows typical fits of the second combination differences for the $3s^2\Sigma^+(0) \leftarrow 2p^2\Pi(1)$ band of $^6Li^{20}Ne$ and $^7Li^{20}Ne$. The upper two fits are made through equation (5-18) and the lower two used equation (5-17). The intercept of the fit is very nearly $4B_v$, while the slope is about $8D_v$. Although the value of H_v is small, it is responsible for the curvature appearing in the second combination differences for the $2p^2\Pi(1)$ state as shown in Figure 19. In equation (5-21), the third term on the right side of the equals sign is more rapidly increasing than the other two terms as N grows larger. Therefore, the H_v term is considered to be an effective value for fitting the data. On the other hand, the upper two fits for the $3s^2\Sigma^+(0)$ state do not have a measurable curvature due to a very small value of H_v. The mass dependence of the fits between two isotopes will be discussed in section E.

Six combination differences give three sets of rotational constants including

FIGURE 19

Second combination differences for the (1-0) transitions of $^{6}Li^{20}Ne$ and $^{7}Li^{20}Ne$. Upper state(⊛), lower state (○).

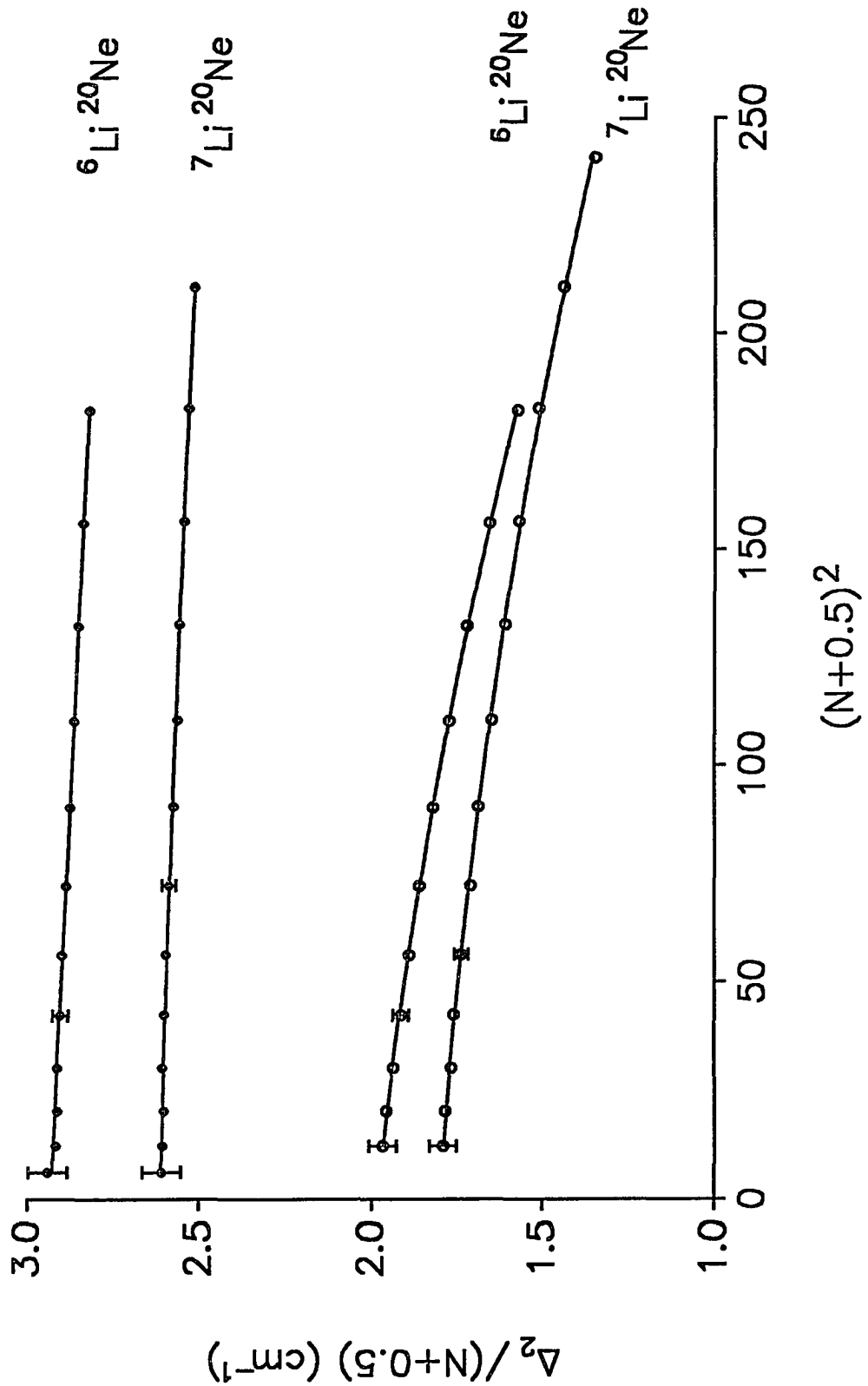

rotational distortion, for each upper and lower state. The corresponding rotational constants are statistically averaged. All values of B_v, D_v and H_v for the thirteen bands, are given in Appendix 2. A list of averaged rotational constants for each measured vibrational level is shown in Table 4.

The band origin ν_o is obtained from well separated and identified lines. From equation (5-10), the band origin is

$$\nu_o = Q(N) - F'_v(N) + F''_v(N) \qquad (5\text{-}22)$$

Since the P branch has a band head and blended lines, it is not suitable for the calculation of a band origin. Further, the R branch is also not the best since usually these lines are weaker than in the Q branch as discussed before. The band origins are thus determined by extrapolation of the Q branch to the rotationless state. As N is increased, the extrapolation error to the band origin is also increased. Therefore, lower N values of Q lines are better to use. In order to get the best possible value of ν_o, 4-6 Q lines are included in the calculation. The list of band origins of measured bands for both isotopes ($^6Li^{20}Ne$ and $^7Li^{20}Ne$) is shown on Table 5.

Once rotational constants and band origins are obtained, fitted R(N), Q(N) and P(N) are produced using equations (5-9, 10, and 11). Figures 20 and 21 show residuals of the fits to the measured $3s^2\Sigma^+ \leftarrow 2p^2\Pi$ line positions (for thirteen bands) for $^6Li^{20}Ne$ and $^7Li^{20}Ne$, respectively. There are 437 lines for $^6Li^{20}Ne$ and 430 lines for $^7Li^{20}Ne$. The average of residuals for $^6Li^{20}Ne$ is 0.029 cm^{-1} and for $^7Li^{20}Ne$ is 0.022 cm^{-1}. The differences between the fitted and measured line positions for most

TABLE 4

Rotational and rotational distortion constants for the $2p^2\Pi$ and $3s^2\Sigma^+$ vibrational levels. All quantities are in cm^{-1}.

$^6Li^{20}Ne$

	$2p^2\Pi$			$3s^2\Sigma^+$	
v	B_v	$D_v(10^{-4})$	$H_v(10^{-6})$	B_v	$D_v(10^{-4})$
0	0.618(3)	0.53(15)	-0.30(3)	0.734(2)	0.80(10)
1	0.494(2)	1.31(23)	-0.52(6)	0.664(2)	0.84(6)
2	0.378(3)	3.27(32)		0.600(2)	0.80(7)
3	0.271(15)	4.39(1.58)		0.535(2)	0.93(7)
4				0.472(9)	0.64(1.09)
5				0.408(4)	1.42(27)

$^7Li^{20}Ne$

	$2p^2\Pi$			$3s^2\Sigma^+$	
v	B_v	$D_v(10^{-4})$	$H_v(10^{-6})$	B_v	$D_v(10^{-4})$
0	0.555(3)	0.51(12)	-0.19(2)	0.656(2)	0.63(8)
1	0.451(2)	1.16(22)	-0.31(6)	0.596(2)	0.66(6)
2	0.356(2)	2.95(8)		0.540(2)	0.66(6)
3	0.259(15)	3.27(1.58)		0.488(3)	0.71(9)
4				0.433(4)	0.72(18)
5				0.381(3)	0.97(13)

TABLE 5

Band origins for the thirteen observed $3s^2\Sigma^+(v') \leftarrow 2p^2\Pi(v'')$ transitions in $^6Li^{20}Ne$ and $^7Li^{20}Ne$.

Isotope	v'',v'	$\nu_0(cm^{-1})$
$^6Li^{20}Ne$		
	0,0	11969.6(2)
	0,1	12106.0(2)
	0,2	12222.7(1)
	1,0	11895.8(1)
	1,1	12032.3(2)
	1,2	12149.1(2)
	1,3	12248.6(1)
	1,4	12331.4(1)
	2,0	11851.9(2)
	2,3	12204.6(3)
	2,4	12287.4(2)
	2,5	12354.0(2)
	3,0	11826.5(1)
$^7Li^{20}Ne$		
	0,0	11968.0(2)
	0,1	12098.0(2)
	0,2	12210.1(1)
	1,0	11896.6(2)
	1,1	12026.5(2)
	1,2	12138.8(2)
	1,3	12235.3(2)
	1,4	12317.0(2)
	2,0	11852.6(2)
	2,3	12191.2(3)
	2,4	12272.9(2)
	2,5	12340.3(2)
	3,0	11826.2(2)

FIGURE 20

Residuals of the fits to all measured $3s^2\Sigma^+ \leftarrow 2p^2\Pi$ line positions for $^6Li^{20}Ne$.

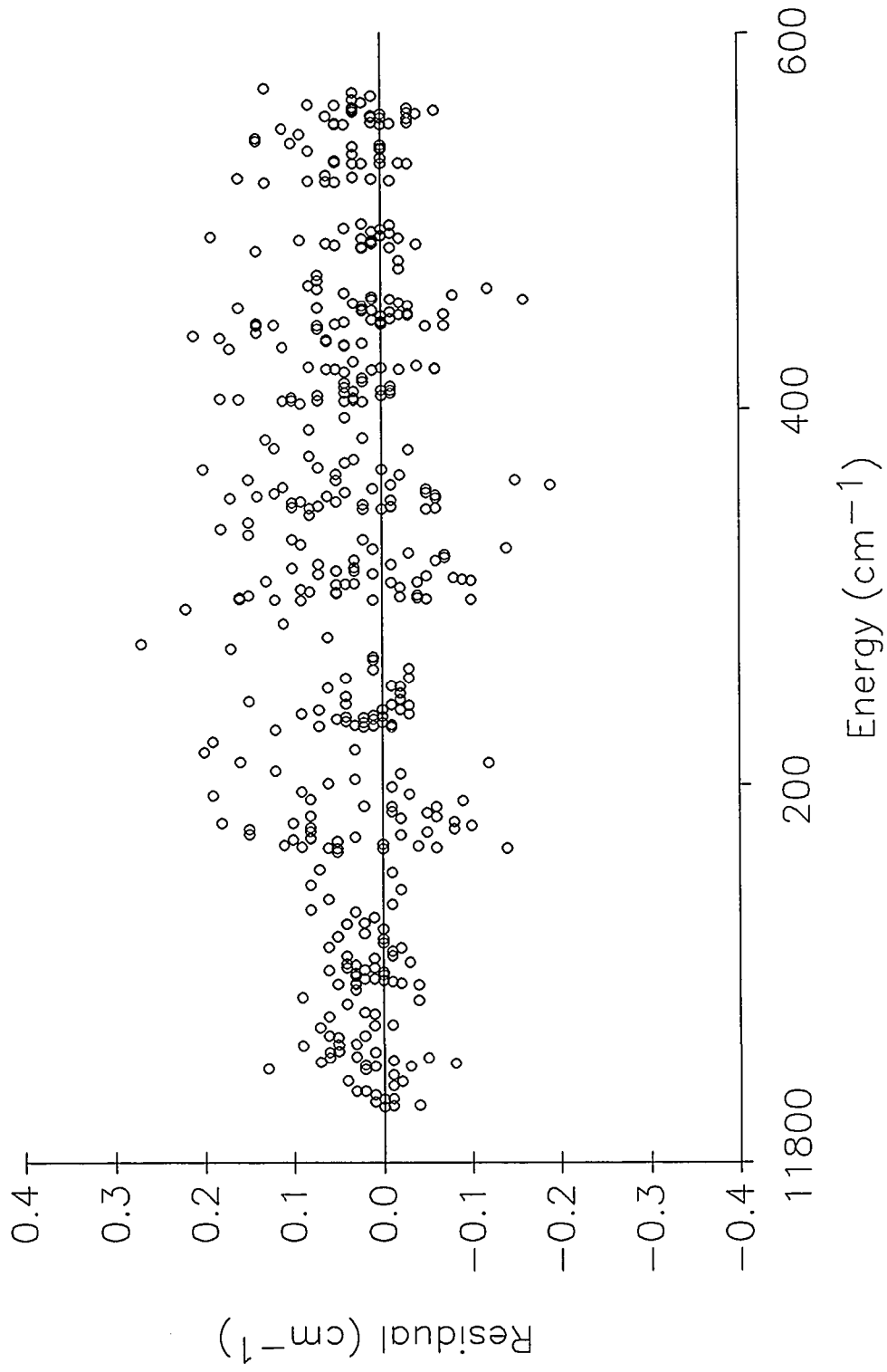

FIGURE 21

Residuals of the fits to all measured $3s^2\Sigma^+ \leftarrow 2p^2\Pi$ line positions for $^7Li^{20}Ne$.

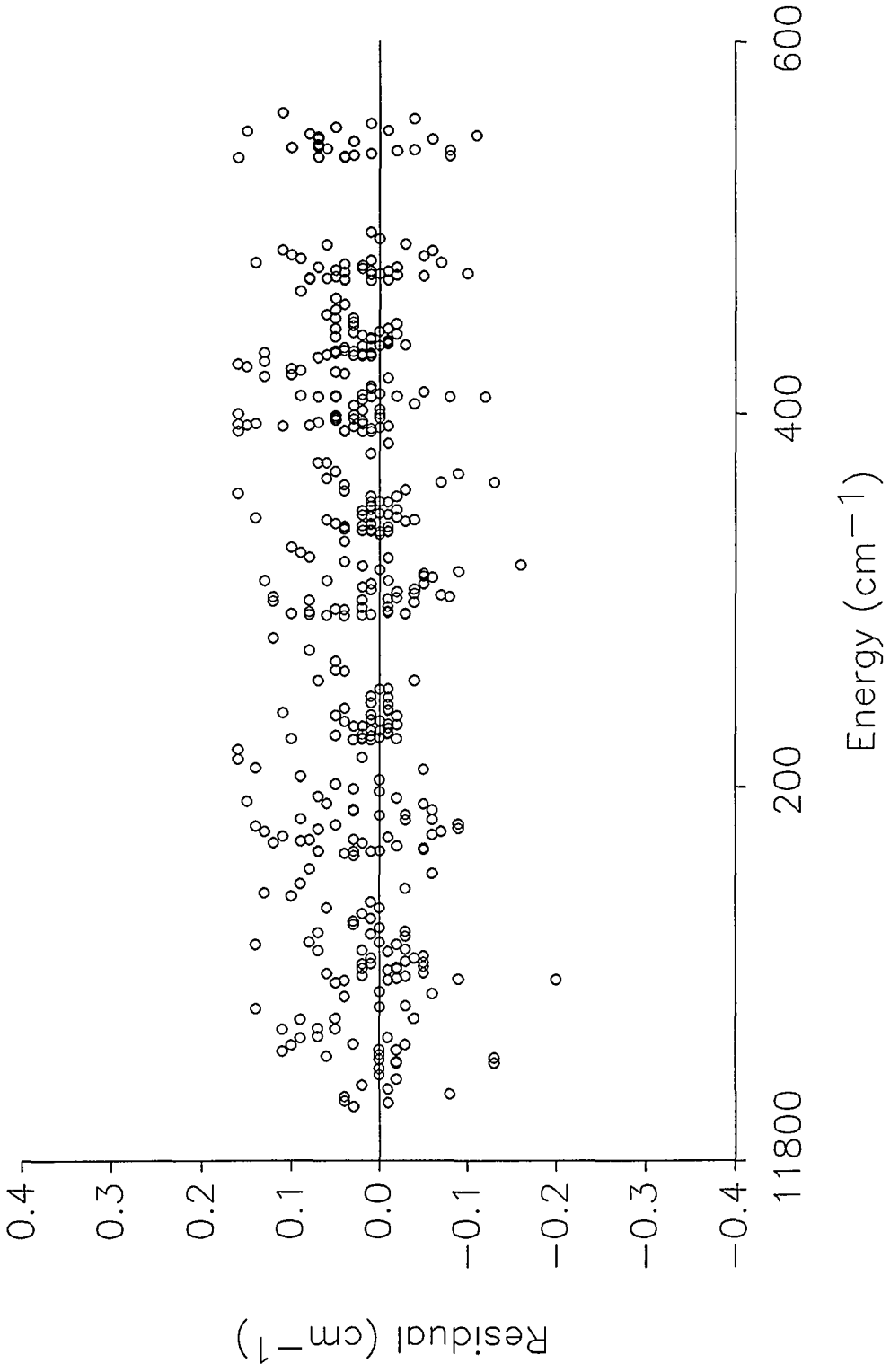

transitions are within 0.2 cm^{-1}, which is within the experimental uncertainty. This confirms the fitting procedure and assignment of the molecular lines. Due to the extrapolation error for the determination of a band origin, the statistical distribution of residuals is shifted as much as 0.029 cm^{-1} in $^{6}Li^{20}Ne$ as shown in Figure 20. Again, this is negligable compared to the experimental resolution.

By fitting the polynomial equation (5-4), the constants, B_e, α_e and γ_e are obtained by substituting the B_v values. Four vibrational states (v"=0, 1, 2 and 3) for the $2p^2\Pi$ state and six (v'=0, 1, 2, 3, 4 and 5) for the $3s^2\Sigma^+$ state are measured in this work. α_e is small compared to B_e, since the change in internuclear distance by the vibration is small compared to the internuclear distance. A list of these constants is in Table 6. B_e corresponds to the equilibrium separation r_e. It is given [55] by

$$B_e = \frac{h}{8\pi^2 c \mu r_e^2}$$

If, we put $R_e = r_e/a_o$ and $\mu_A = \mu N_A$ (units of ^{12}C), then the equation gives [82, 83]

$$R_e = \left(\frac{60.1997}{\mu_A B_e}\right)^{\frac{1}{2}} \qquad (5\text{-}23)$$

TABLE 6

Equilibrium rotational and mass scaled mechanical constants for the $2p^2\Pi$ and $3s^2\Sigma^+$ states of $^6Li^{20}Ne$ and $^7Li^{20}Ne$. All quantities are in cm^{-1}.

	$^6Li^{20}Ne$		$^7Li^{20}Ne$	
	$2p^2\Pi$	$3s^2\Sigma^+$	$2p^2\Pi$	$3s^2\Sigma^+$
B_e	0.684(5)	0.769(3)	0.609(5)	0.685(3)
α_e	0.133(8)	0.072(3)	0.110(8)	0.060(2)
γ_e	0.0043(26)	0.0011(5)	0.0032(25)	0.0009(4)
μB_e	3.16(2)	3.56(1)	3.16(3)	3.56(2)
$\mu^{3/2}\alpha_e$	1.32(8)	0.72(3)	1.30(9)	0.71(2)
$\mu^2\gamma_e$	0.09(6)	0.02(2)	0.08(8)	0.03(3)

C. VIBRATIONAL

The vibrational part of the energy can be extracted from the band origins for each band. For example, the difference of the band origin between the (v"=0, v'=0) and the (v"=0, v'=1) transition is the vibrational energy spacing between the v'=0 and v'=1 levels of the $3s^2\Sigma^+$ state. By adding this to the zero-point energy (v'=0), the vibrational energy (v'=1) is determined. The list of the vibrational energies for each vibrational quantum number is shown in Table 7. In the experiments, four vibrational energy levels (v"=0, 1, 2, and 3) for the $2p^2\Pi$ state and six levels (v'=0, 1, 2, 3, 4, and 5) for the $3s^2\Sigma^+$ state are obtained from the two isotopes ($^6Li^{20}Ne$ and $^7Li^{20}Ne$).

According to equation (5-2), the vibrational constants (ω_e, $\omega_e x_e$, $\omega_e y_e$, and $\omega_e z_e$) are determined. The energy spacing between consecutive vibrational states is given by

$$G(v+1)-G(v) = \omega_e - 2\omega_e x_e(v+1) + \omega_e y_e\left(3v^2+6v+\frac{13}{4}\right) - \omega_e z_e(4v^3+12v^2+13v+5) + \cdots \qquad (5\text{-}24)$$

For the $2p^2\Pi$ state, terms higher than $\omega_e z_e$ are neglected. The three constants are obtained by solving the three equations. In the case of the $3s^2\Sigma^+$ state, the $\omega_e z_e$ term is included since there are six vibrational states and the $\omega_e z_e$ term contributes significantly to the vibrational energy for the high vibrational states. Equation (5-24) is expressed as the polynomial equation which is a function of v. The coefficients of

TABLE 7

Vibrational energies for the $2p^2\Pi$ and $3s^2\Sigma^+$ states. All quantities are in cm^{-1}.

	$^6Li^{20}Ne$		$^7Li^{20}Ne$	
	$2p^2\Pi$	$3s^2\Sigma^+$	$2p^2\Pi$	$3s^2\Sigma^+$
G(0)	51.5(7)	76.5(9)	49.0(7)	72.4(7)
G(1)	125.2(7)	212.9(9)	120.4(7)	202.3(7)
G(2)	169.2(7)	329.8(9)	164.5(7)	314.6(8)
G(3)	194.6(7)	429.2(9)	190.9(7)	411.1(8)
G(4)		512.1(1.0)		492.8(9)
G(5)		578.8(1.1)		560.22(9)
D_o	161(5)		163(5)	

a equal weightted least square fitting equation are converted to the vibrational constants. Table 8 shows the list of the vibrational constants of both states for $^{6}Li^{20}Ne$ and $^{7}Li^{20}Ne$.

The zero-point energy is given by

$$G(v=0) = \frac{1}{2}\omega_e - \frac{1}{4}\omega_e x_e + \frac{1}{8}\omega_e y_e - \frac{1}{16}\omega_e z_e + \cdots \qquad (5\text{-}25)$$

The vibrational quantum numbering in both states is unambiguously determined from the measured isotope shifts of the band origins. Consider an unknown state of vibrational quantum number x, then the next state must have the quantum number x+1, and so on. On the right hand side of the equal sign in equation (5-24), the vibration constants of $^{6}Li^{20}Ne$ are replaced with the values from the following isotope relations [55]

$$\omega_e^i = \rho\omega_e, \quad \omega_e x_e^i = \rho^2\omega_e x_e, \quad \omega_e y_e^i = \rho^3\omega_e y_e, \quad \omega_e z_e^i = \rho^4\omega_e z_e$$

$$\rho = \sqrt{\frac{\mu(^{6}Li^{20}Ne)}{\mu(^{7}Li^{20}Ne)}} \qquad (5\text{-}26)$$

where i denotes $^{7}Li^{20}Ne$. Then the values of the left side of equation (5-24) will be the experimental vibrational spacing of $^{7}Li^{20}Ne$. If

$$G'(x+1) - G'(x) = \rho\omega_e - 2\rho^2\omega_e x_e(x+1) + \cdots$$

is solved for x, the vibrational quantum number for the G(x) state will be the closest

TABLE 8

Equilibrium vibrational and mass scaled mechanical constants for the $2p^2\Pi$ and $3s^2\Sigma^+$ states of $^6Li^{20}Ne$ and $^7Li^{20}Ne$. All quantities are in cm^{-1}.

	$^6Li^{20}Ne$		$^7Li^{20}Ne$	
	$2p^2\Pi$	$3s^2\Sigma^+$	$2p^2\Pi$	$3s^2\Sigma^+$
ω_e	114.1(1.3)	158.9(1.7)	108.1(1.3)	150.0(1.4)
$\omega_e x_e$	23.2(6)	12.2(8)	21.0(6)	10.8(6)
$\omega_e y_e$	1.8(1)	0.68(22)	1.6(1)	0.53(17)
$\omega_e z_e$		0.04(2)		0.03(2)
$\mu^{1/2}\omega_e$	245.4(2.8)	341.7(3.7)	246.4(3.0)	341.8(3.2)
$\mu\omega_e x_e$	107.3(2.7)	56.4(3.7)	109.1(3.1)	56.1(3.1)
$\mu^{3/2}\omega_e y_e$	17.9(1.0)	6.8(2.2)	18.9(1.2)	6.3(2.0)
$\mu^2\omega_e z_e$		0.86(43)		0.81(54)

integer to the value of x. There are two assumptions in this method. The first is, that the isotope relations are correct for the vibrational constants. More details of the isotope relation are discussed in a later section of this dissertation. Second, the vibrational states, are consecutively observed. Those two assumptions can be confirmed by the location of the band spectrum in the whole data of both isotopes. There is no evidence that the other band between observed vibrational states is observed. It is also checked with the rotation constant. The smoothness of the variation in the rotational constant which depends on the vibrational quantum number is good evidence to support the above assumption.

D. SPIN-ORBIT SPLITTING IN THE $2p^2\Pi(v''=0)$ LEVEL

A well-resolved splitting of lower N" levels is observed in the bands originating in the $2p^2\Pi(v''=0)$ level. As shown in Figures 17 and 18, the splitting decreases rapidly with increasing N". The positions of the measurable split lines are listed in Table 9. There are two components (F1 and F2) for each N. F1 corresponds to a fine structure component with $J''=N''+1/2$ and F2 to $J''=N''-1/2$.

When the influence of the molecular rotation predominates, S is uncoupled from the molecular axis. This is called spin uncoupling [57]. In other words, if the nuclear rotation is decreased, S is coupled to the molecular axis and the spin-orbit interaction becomes more evident. For large rotation, there is only a small splitting

TABLE 9

Measured line positions for transitions out of the $2p^2\Pi(v''=0)$ levels that are split due to the spin-orbit interaction. All quantities are in cm^{-1}.

$^{6}Li^{20}Ne$

(0,0)

N	F	R(N)	Q(N)	P(N)
2	F2	11975.46(1)	11971.06(1)	11968.13(1)
	F1	11975.28(1)	11970.93(1)	11968.00(1)
3	F2	11977.57(1)	11971.71(1)	11967.32(1)
	F1	11977.47(1)	11971.61(1)	11967.24(1)
5	F2	11982.41(1)		
	F1	11982.35(1)		

(0,1)

2	F2			12104.43(1)
	F1			12104.30(1)

$^{7}Li^{20}Ne$

(0,0)

N	F	R(N)	Q(N)	P(N)
3	F2		11969.99(1)	
	F1		11969.78(1)	
4	F2	11977.25(1)	11970.74(1)	
	F1	11977.08(1)	11970.59(1)	
5	F2	11979.52(1)	11971.68(1)	
	F1	11979.39(1)	11971.56(1)	

6	F2	11981.93(1)	11972.85(1)	
	F1	11981.83(1)	11972.77(1)	
(0,1)				
3	F2			12095.58(1)
	F1			12095.39(1)
5	F2		12099.76(1)	12093.85(1)
	F1		12099.63(1)	12093.74(1)
6	F2		12100.22(1)	
	F1		12100.12(1)	

of the levels with a given N (=R+Λ). A spin-orbit interaction is normally described by a spin-orbit parameter A_v.

The rotation term values of the components of doublet states have been calculated theoretically by Hill and Van Vleck [62] for any magnitude of the coupling between S and L and are given by

$$F_{v1}(J) = B_v[(J+\frac{1}{2})^2 - \Lambda^2 - \frac{1}{2}\sqrt{[4(J+\frac{1}{2})^2 + Y(Y-4)\Lambda^2]} - D_v J^4$$
$$F_{v2}(J) = B_v[(J+\frac{1}{2})^2 - \Lambda^2 + \frac{1}{2}\sqrt{[4(J+\frac{1}{2})^2 + Y(Y-4)\Lambda^2]} - D_v (J+1)^4 \qquad (5\text{-}27)$$

where J is the total angular momentum including spin and $Y=A_v/B_v$. For the $2p^2\Pi$ state, $\Lambda=1$ is substituted in equation (5-27), yielding

$$F_v(J) = B_v[(J+\frac{1}{2})^2 - 1] \mp B_v(J+\frac{1}{2})\sqrt{1+\frac{Y(Y-4)}{4(J+1/2)^2}} \qquad (5\text{-}28)$$

Here, the rotational distortion terms are neglected and the top sign is for $F_{v1}(J)$, while the bottom is for $F_{v2}(J)$. This is exactly the same as equation (2-21). Substituting $J=N\pm1/2$ into equation (5-28), gives

$$F_{v1}(J=N+\frac{1}{2}) = B_v[(N+1)^2 - 1] - B_v(N+1)\sqrt{1+\frac{Y(Y-4)}{4(N+1)^2}}$$
$$F_{v2}(J=N-\frac{1}{2}) = B_v[N^2 - 1] + B_v N\sqrt{1+\frac{Y(Y-4)}{4N^2}} \qquad (5\text{-}29)$$

For large N, the radical in the second term is small compared to 1. Equation (5-29) reduces to the usual case (b) expression, $B_v[N(N+1)-1]$, for the $2p^2\Pi$ state. It is also readily seen that F_{v1} equals F_{v2} for the same N value if Y=0 or 4, and F_{v1} and F_{v2} are nearly equal when Y is small. Even for larger Y values, F_{v1} and F_{v2} become more and more alike with increasing N.

Figure 22 shows the energy level diagram for the first few transition of a $^2\Sigma^+ \leftarrow {}^2\Pi$ band [57]. The intervals between the $^2\Sigma^+$, the $^2\Pi_{1/2}$ and the $^2\Pi_{3/2}$ states are so large that they can not be drawn to scale in the diagram. The so-called N values are virtual values of N obtained from the J values according to the definitions N=J-1/2 for F_{v1} and N=J+1/2 for F_{v2}, i.e. they are the N values which the levels would take on if we could make $A_v \rightarrow 0$. The lowest levels, J"=1/2 of $^2\Pi$, are assigned to N"=(0), since it is classified as a F_{v1} level in case (a), although really, if we could make $A_v \rightarrow 0$, J=1/2 would become $F_{v2}(1/2)$ which corresponds to N"=1. There are 10 branches, neglecting the positive and negative rotational levels. In the band line labels, the main labels P, Q, or R represents $\Delta J=-1$, 0 and 1, respectively, which in the main branches is equal to ΔN. Each main branch has two (F_{v1} and F_{v2}) branches. The superscript symbol P, Q or R in the satellite branches represents ΔN, where $\Delta J \neq \Delta N$. The intensity of four satellite branches would, in case (b), decrease very rapidly with increasing N. Their designations are $^QP_{21}$, $^RQ_{21}$, $^QR_{12}$ and $^PQ_{12}$ [57]. The first subscript denotes the upper state of F1 or F2 and the second denotes the lower state. They have the same form as the six main branches and, for a small doublet splitting of the $^2\Sigma^+$ state, their lines lie very close to the corresponding lines of the main branches. In this dissertation experiment, these satellite branches are not

FIGURE 22

Energy level diagram for the first few transitions of the $3s^2\Sigma^+ \leftarrow 2p^2\Pi$ band [84].

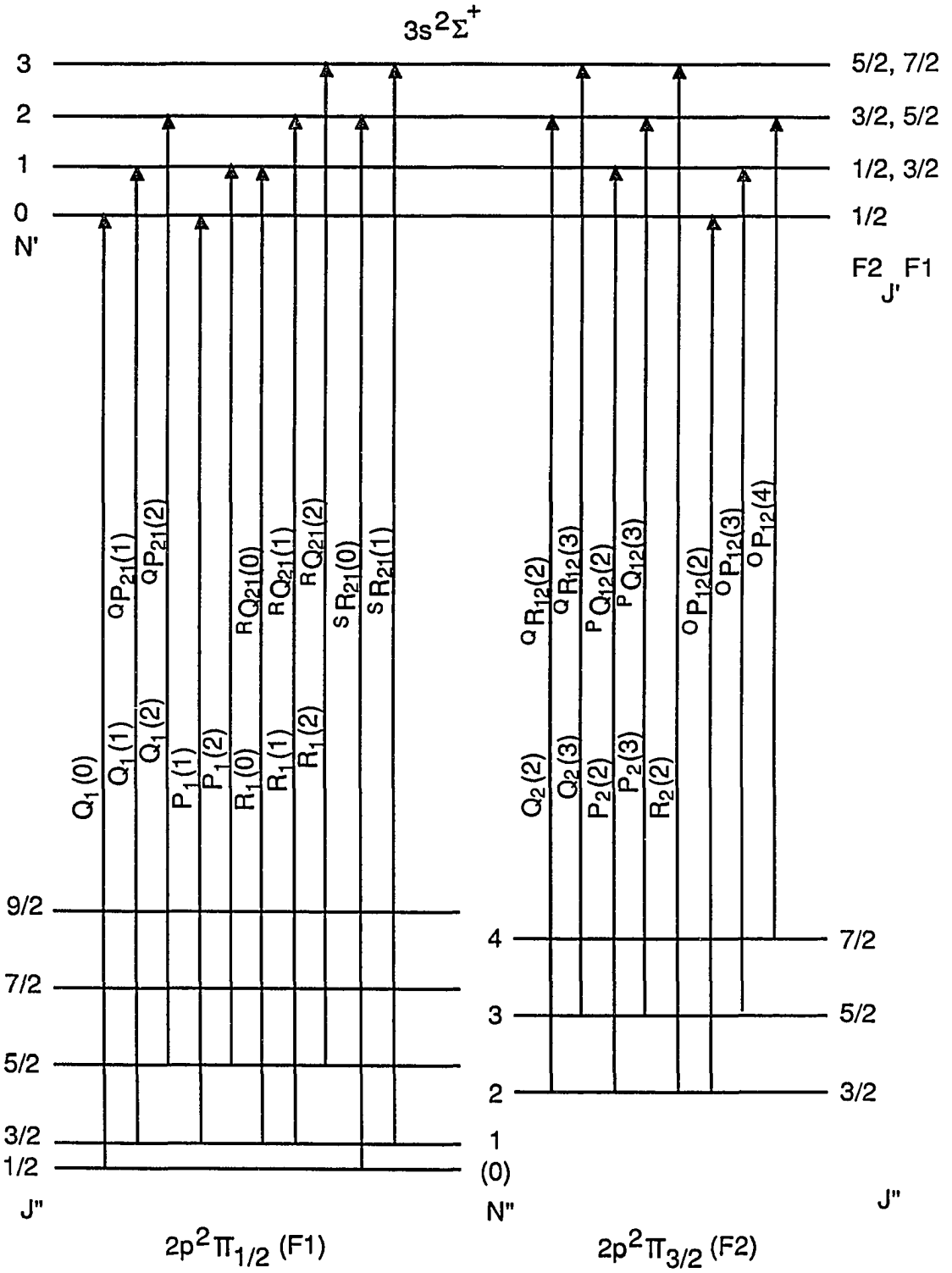

observed. In Figure 22, energy levels for F_{v1} and F_{v2} of the $3s^2\Sigma^+$ state are drawn on the same line.

The superscript symbol O means N'-N"=-2, S means N'-N"=+2 [57, 84]. These transitions would be forbidden in case (b) by the selection rule $\Delta N=0, \pm 1$. With a case (a) $^2\Pi$ state, the branches which in case (b) would be main, satellite, and forbidden are all strong branches. Due to the presence of weak $^{6,7}Li^{22}Ne$ transitions and line congestion in the band origin region, these $\Delta N=\pm 2$ transitions have not been unambiguously assigned. Thus, higher resolution data will be required.

The line positions of split transitions at low N out of the $2p^2\Pi(v"=0)$ level, are listed in Table 9. However, some low N transitions (e.g. N=1) are not listed, because they could not be unambiguously assigned due to line congestion or weak intensity as shown in Figures 17 and 18. When two graphs are compared with each other, the measured splittings are significantly greater for $^7Li^{20}Ne$. Since the rotational constant (B_v) for the $2p^2\Pi(v"=0)$ level is greater for $^6Li^{20}Ne$, the larger value of Y ($=A_v/B_v$) for $^7Li^{20}Ne$ is expected.

$\Delta F_v = F_{v2} - F_{v1}$ is the value of the splitting and is used to get the spin-orbit parameter A_v by substituting $Y=A_v/B_v$. Furthermore, for estimating the error of A_v for the $2p^2\Pi(v"=0)$ level, a numerical calculation is performed which varies the value of the rotational constant B" and A_v until the difference between the measured and calculated splitting is less than 0.0005 cm^{-1}. This numerical calculation is necessary since the value of the rotation constant B" in the rotational analysis may be varied due to the splitting in the lower N of the $2p^2\Pi(v"=0)$ level.

When reconsidering the rotational analysis with the elimination of the spin-

orbit splitting (Y=0), the change in the value of the rotational constants are much less than the estimated error. Therefore, the estimated error for A_v is combined with the error of B_v and the measured line position.

Values of Y=4.99(5) and Y=4.48(5) are obtained for $^7Li^{20}Ne$ and $^6Li^{20}Ne$, respectively. Each of these values leads to a spin-orbit parameter of A_v=2.77(3) cm^{-1} for the $2p^2\Pi(v''=0)$ level. For $v''>0$, no splitting is observed at low N. Within the linewidth, about 0.15 cm^{-1}, the value for Y is then either about 4.3(3) or less than 0.3 for those levels.

E. ISOTOPE RELATIONS

As mentioned earlier, spectra for the $3s^2\Sigma^+ \leftarrow 2p^2\Pi$ transition for the two molecules $^6Li^{20}Ne$ and $^7Li^{20}Ne$ are taken and analyzed. From these data, the reduced mass dependence of the spectroscopic constants can be obtained. Since the potential energy functions of the two molecules depends on the motions of the electrons and the Coulomb repulsion of the nuclei, they are identical to a high degree of approximation. Also, since the Coulomb repulsion of the nuclei is independent of the masses while the motions of the electrons are almost independent of these masses, the mass difference affects only the vibrational and rotational energy of the molecule in each electronic state.

Assuming harmonic vibrations, the (classical) vibrational frequency ν is given

by

$$\nu = \frac{1}{2\pi}\sqrt{\frac{k}{\mu}} \qquad (5\text{-}30)$$

where k is the force constant. Since it is determined by the electronic motion only, k is exactly the same for different isotopic molecules, whereas the reduced mass μ is different. Therefore, the ratio between frequencies of two isotopes is

$$\frac{\nu^i}{\nu} = \sqrt{\frac{\mu}{\mu^i}} = \rho \qquad (5\text{-}31)$$

where the superscript i refers to the $^7Li^{20}Ne$ molecule. Substituting equation (5-31) into equation (4-2) and including higher order terms then gives [55]

$$\begin{aligned} G^i(v) &= \omega_e^i(v+\tfrac{1}{2}) - \omega_e x_e^i(v+\tfrac{1}{2})^2 + \omega_e y_e^i(v+\tfrac{1}{2})^3 + \cdots \\ &= \rho\,\omega_e(v+\tfrac{1}{2}) - \rho^2\omega_e x_e(v+\tfrac{1}{2})^2 + \rho^3\omega_e y_e(v+\tfrac{1}{2})^3 + \cdots \end{aligned} \qquad (5\text{-}32)$$

Also, substituting equation (5-31) into equation (5-3), then gives

$$\begin{aligned} F^i(N) &= B^i[N(N+1)-1] - D^i[N(N+1)-1]^2 + H^i[N(N+1)-1]^3 + \cdots \\ &= \rho^2 B[N(N+1)-1] - \rho^4 D[N(N+1)-1]^2 + \rho^6 H[N(N+1)-1]^3 + \cdots \end{aligned} \qquad (5\text{-}33)$$

However, the above relation holds rigorously only for B_e, D_e and H_e, since the

equilibrium internuclear distances are the same in the two isotopic molecules, see equation (5-23), but not the effective internuclear distances for a given vibrational number v. The following relations hold for the rotational constants [55]

$$B_e^i = \rho^2 B_e,\ D_e^i = \rho^4 D_e,\ and\ H_e^i = \rho^6 H_e \qquad (5\text{-}34)$$

$$\alpha_e^i = \rho^3 \alpha_e, \gamma_e^i = \rho^4 \gamma_e,\ and\ \beta_e^i = \rho^5 \beta_e \qquad (5\text{-}35)$$

In the lower section of Table 6 and 8, isotopic mass scaled spectroscopic constants of both $2p^2\Pi$ and $3s^2\Sigma^+$ states are presented. All the vibrational and rotational constants that are listed in the table are in very good agreement with the usual reduced mass dependence. A reduced mass of 4.6239 and 5.1935 are used for $^6Li^{20}Ne$ and $^7Li^{20}Ne$, respectively [82, 83]. Differences in the intercepts, slopes, and curvatures in the fitting between the isotopes are clearly shown in Figure 19. Comparison of Figure 16 with 17 shows the spectral dependence on the reduced mass in the region of the band origin of the (0-0) transition. For this transition, the band origin of $^7Li^{20}Ne$ is red shifted from that of $^6Li^{20}Ne$. Also the splittings due to the spin-orbit interaction for $^7Li^{20}Ne$ are greater than for $^6Li^{20}Ne$ as discussed previously. The weaker lines in the figures have been confirmed to be due to the natural abundances of ^{20}Ne and ^{22}Ne. Since these isotopic molecular lines are so weak and congested, they have not been unambiguously assigned.

F. LONG RANGE ANALYSIS

Determination of the dissociation energy using the usual vibrational constants is subject to a large uncertainty. The reasons for this are the relatively high anharmonicity of the potential and absence of experimental vibrational data in the region of dissociation. Actually, the potential energy of an anharmonic oscillator represents the potential energy of a diatomic molecule near the equilibrium position only. Therefore, the region of dissociation (large value of internuclear separation) has been treated with a different method.

Vibrational levels of electronic states of diatomic molecules near dissociation limits may often be related to the long range nature of the relevant potential energy curve (e.g. $-C_6/R^6$). Physically, this is because, although the molecule repeatedly vibrates classically from an inner turning point to an outer turning point, it spends much of its time in the long range region (where the amplitude of its wavefunction is correspondingly large). Hence the potential energy of such levels is well described by its long range form [26].

In this dissertation, the experimental data has been applied to LeRoy's form [25],

$$[D_e - G(v)]^{\frac{n-2}{2n}} = C(v_D - v) \qquad (5\text{-}36)$$

where $n \neq 2$, D_e is the dissociation limit of the potential, C is a constant, and v_D is the

noninteger "effective" vibrational index of the dissociation limit (see appendix 3). They employed the first order WKB quantum condition useful in dealing with slowly varying potentials for the eigenvalues of a potential $V(R) = D_e - C_n/R^n$, where C_n is a constant and R is the nuclear separation.

In the analysis it was assumed that the above long range model is correct, and D_e was varied to fit the data with a choice of n. The result for D_e is not strongly sensitive to the long range exponent (n=4, 5, and 6).

For the $3s^2\Sigma^+$ state for both isotopes, the estimated D_e is about 770(30) cm^{-1}. Figure 23 shows that the long range fitting depends on the choice of the dissociation energy with n=5. There is slight curvature on the graphs for D_e=800 and 750 cm^{-1}. The fitting for the $2p^2\Pi$ state as shown as Figure 24 predicted a value for the dissociation energy of 210(10) cm^{-1} with n= 5.

However, the above method requires the energies and relative vibrational numbering of four or more rotationless levels lying close to the dissociation limit D_e (i.e. less than about 10 % of the well depth below D_e) to yield the best estimates of D_e and of the long range interatomic potential [25]. In this experiment, there are not enough measured vibrational levels in the region. Thus, this long range analysis should be expected to be an estimate only of the actual long range potential. Particularly, since there is a barrier above the atomic Li 3s asymptote in long range region, the shape of the potential is not well determined using this method.

FIGURE 23

Fitting of the 5th power of the long range analysis for the $3s^2\Sigma^+$ state of $^7Li^{20}Ne$.

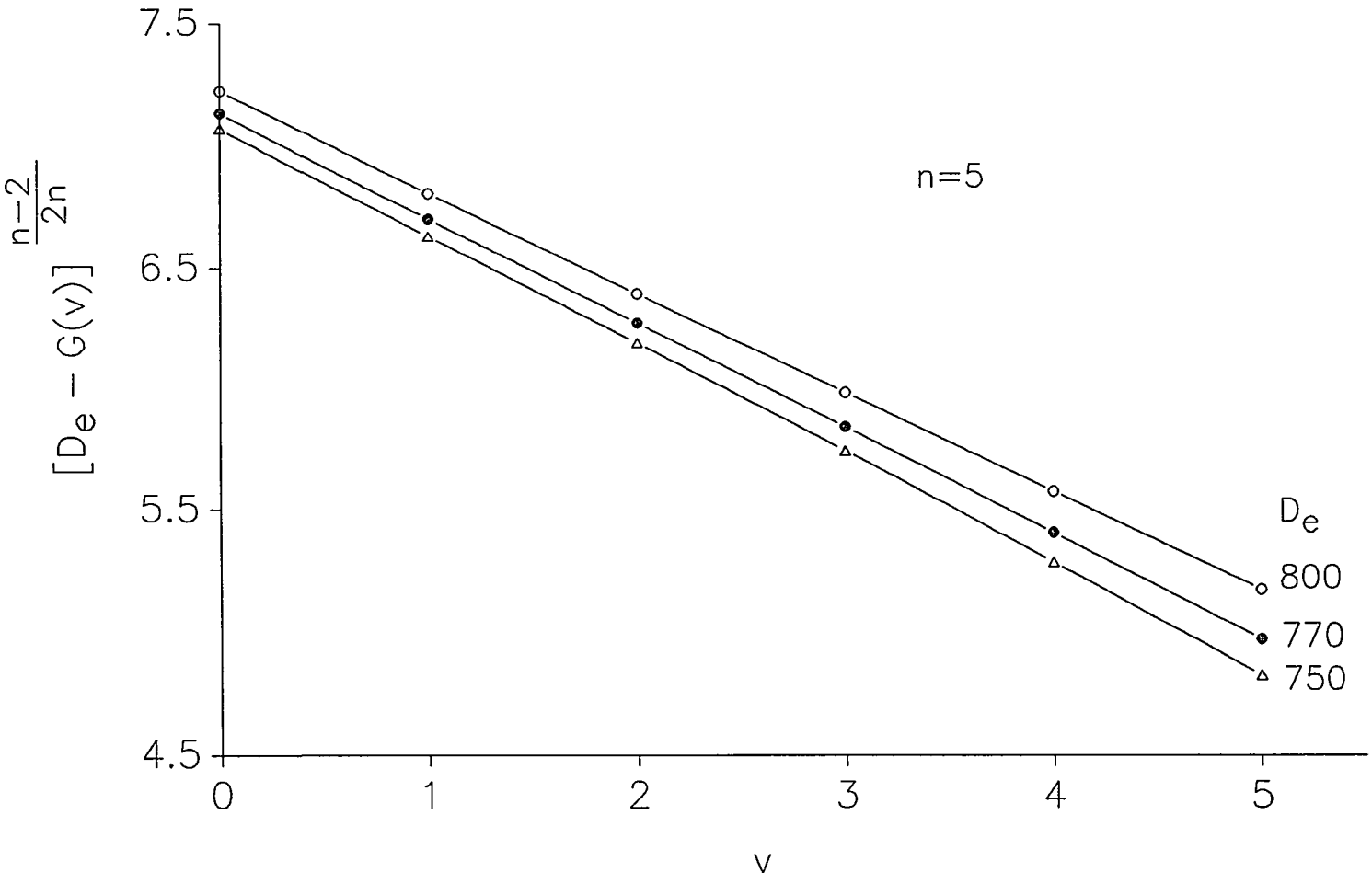

FIGURE 24

Fitting of the 5th power of the long range analysis for the $2p^2\Pi$ state of $^7Li^{20}Ne$.

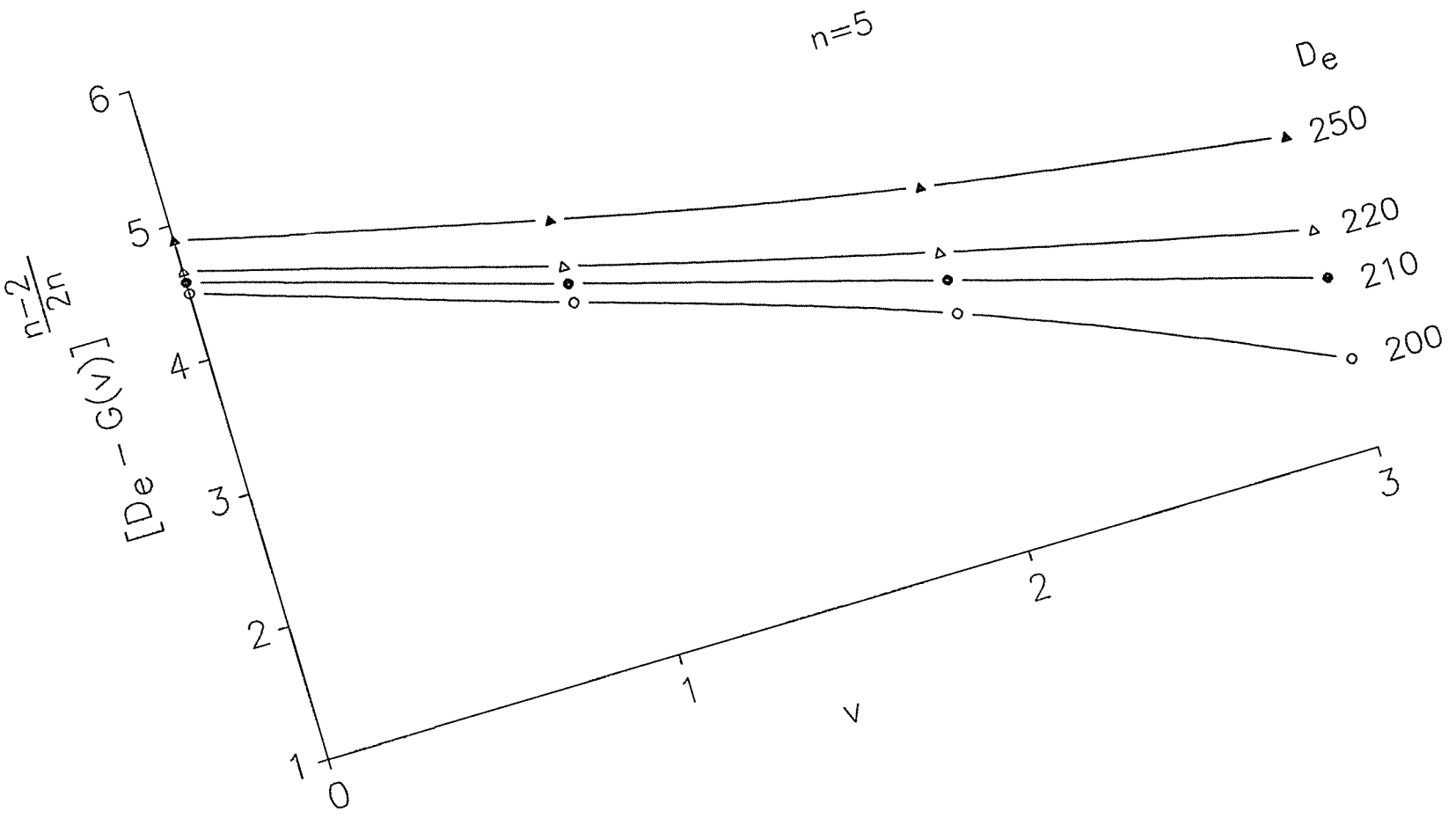

G. INVERSE PERTURBATION ANALYSIS

Inverse perturbation analysis (IPA) uses first-order perturbation theory [85, 53]. The equation for the first-order energy correction is used inversely to find the perturbation responsible for the energy correction. Consider the Schrodinger equation in the adiabatic approximation,

$$\begin{aligned} H\psi_n &= E_n\psi_n \\ &= (T+V(r))\psi_n \end{aligned} \tag{5-37}$$

where T is the nuclear kinetic energy, V(r) is the effective potential, and r is the internuclear distance. V(r) can be initially expressed in terms of a set of ordinary linear equations

$$V(r) = \sum_i C_i f_i(r) \tag{5-38}$$

By adding a small correction ΔV(r), equation (5-37) becomes

$$\begin{aligned} (T+V(r)+\Delta V(r))\psi_n &= (T+V(r))\psi_n + \Delta V(r)\psi_n \\ &= E_n\psi_n + \Delta V(r)\psi_n \end{aligned} \tag{5-39}$$

If the experimental eigenenergies are ε_n then

$$\varepsilon_n - E_n = \langle \psi_n \mid \Delta V(r) \mid \psi_n \rangle \tag{5-40}$$

where $\Delta V(r)$ can be expressed as

$$\Delta V(r) = \sum_i \Delta C_i f_i(r)$$

The ΔC_i can be obtained from equation (5-40) with a least squares fitting routine. In other words, new C_i and V(r) can be obtained as

$$C_i^{new} = C_i^{old} + \Delta C_i \qquad (5-41)$$

$$and \quad V_{(r)}^{new} = V_{(r)}^{old} + \Delta V(r) \qquad (5-42)$$

The initial potential was expressed in terms of the same basis functions. The potential energy correction, $\Delta V(r)$, calculated with these best expansion coefficients will not be the true correction but only a partial correction. This correction can be used to calculate a new, improved approximate potential V(r), and the whole procedure can be iterated with this improved approximate potential. Calculations using this method are described in Meyer, et.al. [53].

To choose the basis functions, it was convenient to express the potential for $R<R_e$ in a manner different than for $R>R_e$

$$V(R) = \sum_{i=0}^{1} \frac{e_i'}{R} \lambda^{2i+1} \qquad R<R_e$$

$$V(R) = \sum_{i=0}^{5} e_i \lambda^{2i+1} \qquad R>R_e \qquad (5-43)$$

where $\lambda = 1-(R_e/R)^P$; R_e is the equilibrium internuclear separation and P a parameter. The 1/R factor for $R<R_e$ produces a hard repulsive wall while the power λ with

$P' < 0$, tends to soften it in an adjustable manner. For $R > R_e$ with $P > 0$, the potential asymptotically approaches a dissociation energy as $R \rightarrow \infty$. The two forms join smoothly at $R = R_e$. This potential is obtained from a variant of the Thakkar potential [86]. Since the highest of the levels are predicted to be quasibound, the levels for the $2p^2\Pi$ state above 210 cm^{-1} are not included in the IPA data set initially. Subsequent inclusion of these levels did not lead to a significant increase in the IPA potential well depth. For the $2p^2\Pi$ state a total of 88 data points from both isotopes are included to obtain the best result. The parameter P and the coefficients e_i and e_i', describe a potential whose calculated eigenvalues for the 88 levels agree with those obtained from the experimental data to less than ± 0.1 cm^{-1}. The predicted well depth is 211.9 cm^{-1}. Figures 25 and 26 show how the energy levels depend on N". The rotational mixing between different vibrational level can be ignored, since energy levels with same N" and different v" are well separated.

For the $3s^2\Sigma^+$ state, 165 energy level positions are used in the fit and the calculated levels agree with the experimental data within ± 0.18 cm^{-1} (only 7 points do not agree within ± 0.1 cm^{-1}). Also, in this state, both $^6Li^{20}Ne$ and $^7Li^{20}Ne$ data are used for the IPA fit. A maximum depth of 570 cm^{-1} relative to its $R \rightarrow \infty$ asymptote is predicted. A calculated barrier of 80.3 cm^{-1} peaked around 10.02 a_o produces a 650.8 cm^{-1} well depth from the top of the barrier. More discussion about this barrier is provided in Chapter 6. As shown as in Figures 27 and 28, the vibrational level $v' = 5$ is above the asymptote ($R \rightarrow \infty$) for both isotopes.

Figures 29 and 30 show the potential and the associated squared vibrational wavefunctions of the $2p^2\Pi$ and $3s^2\Sigma^+$ states, respectively. As discussed before, a

FIGURE 25

Diagram of ro-vibrational energy versus rotational quantum number (N) for each vibrational level of the $2p^2\Pi$ state of $^7Li^{20}Ne$.

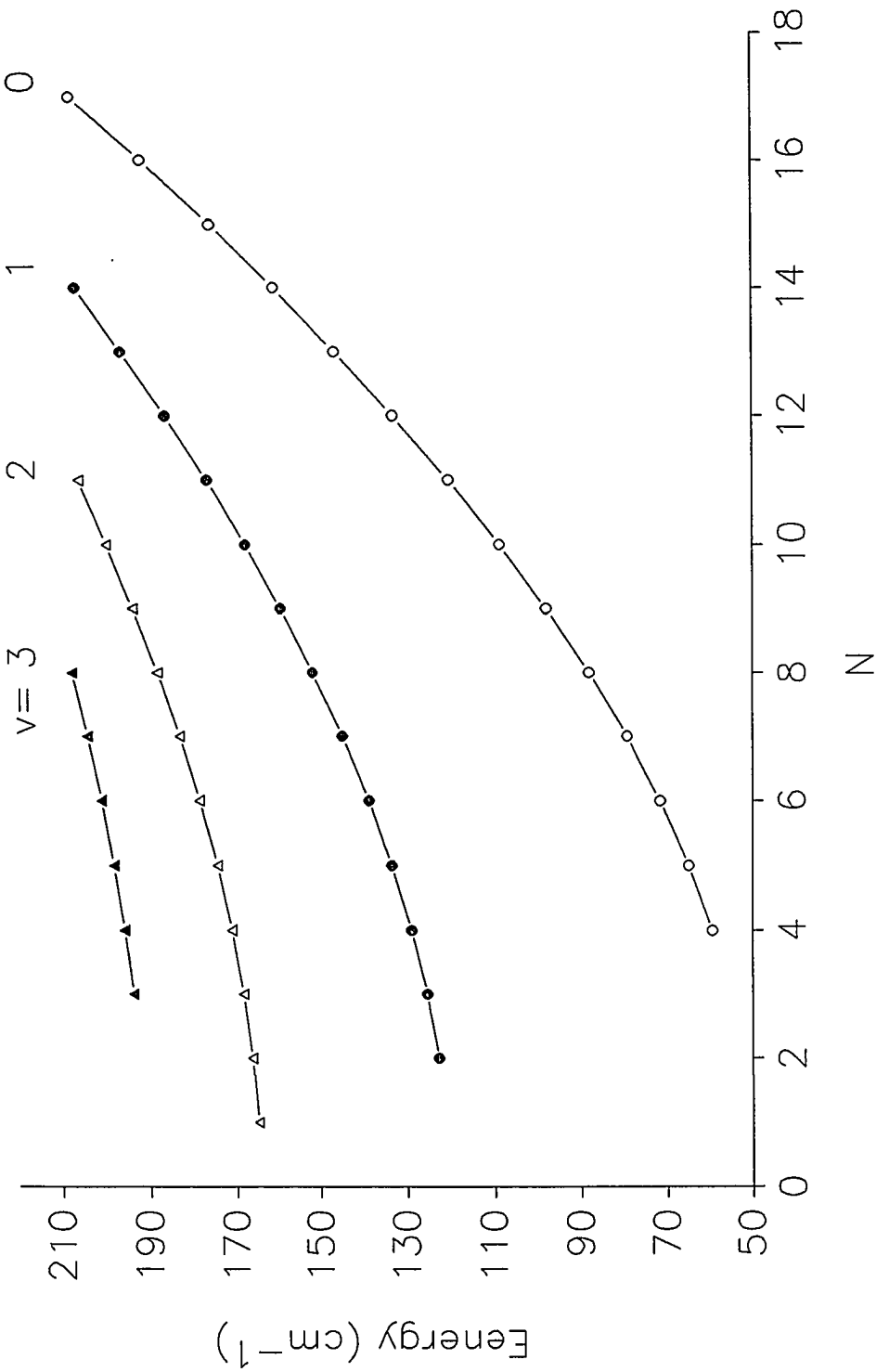

FIGURE 26

Diagram of ro-vibrational energy versus rotational quantum number (N) for each vibrational level of the $2p^2\Pi$ state of $^6Li^{20}Ne$.

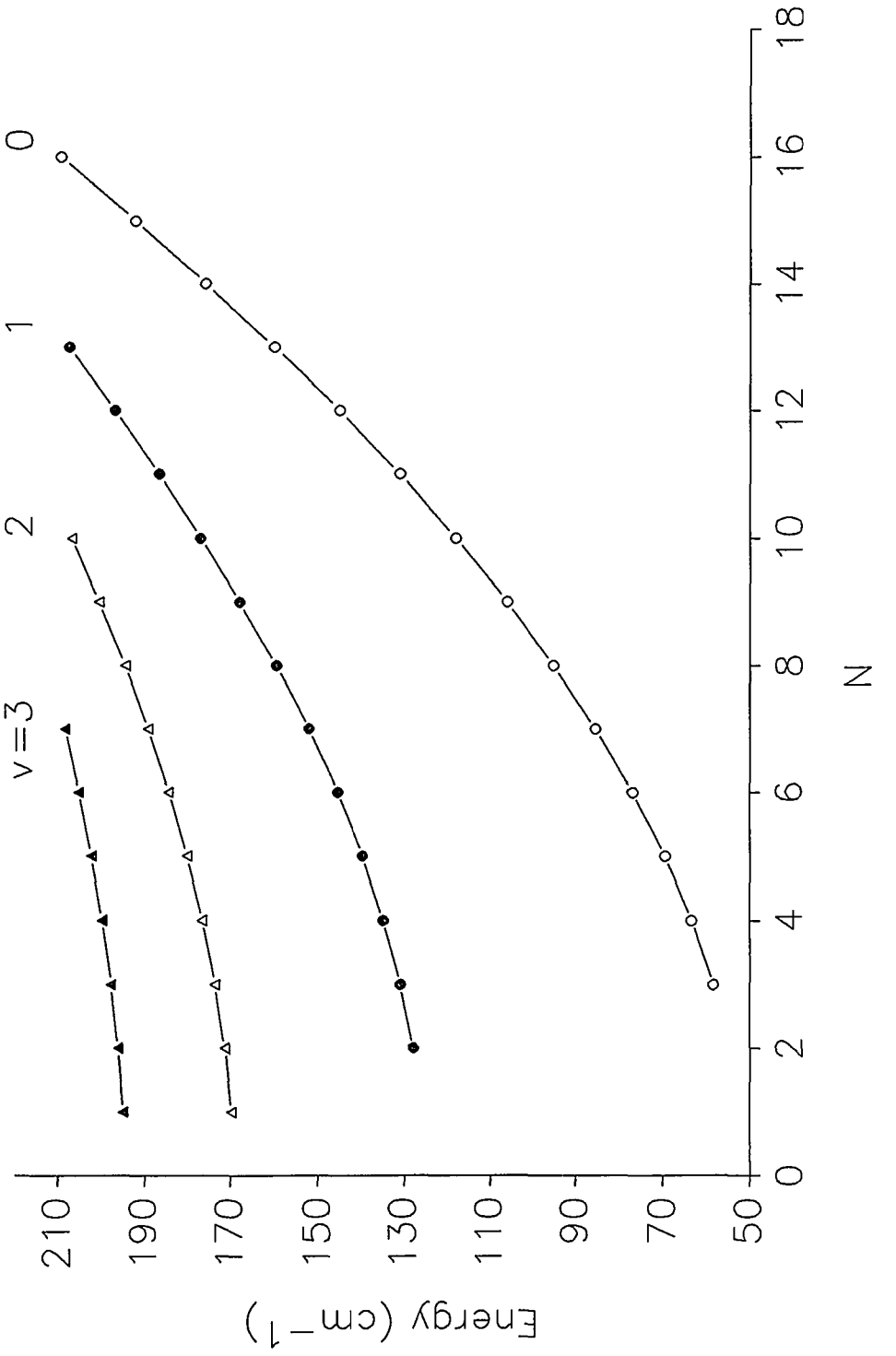

FIGURE 27

Diagram of ro-vibrational energy versus rotational quantum number (N) for each vibrational level of the $3s^2\Sigma^+$ state of $^6Li^{20}Ne$.

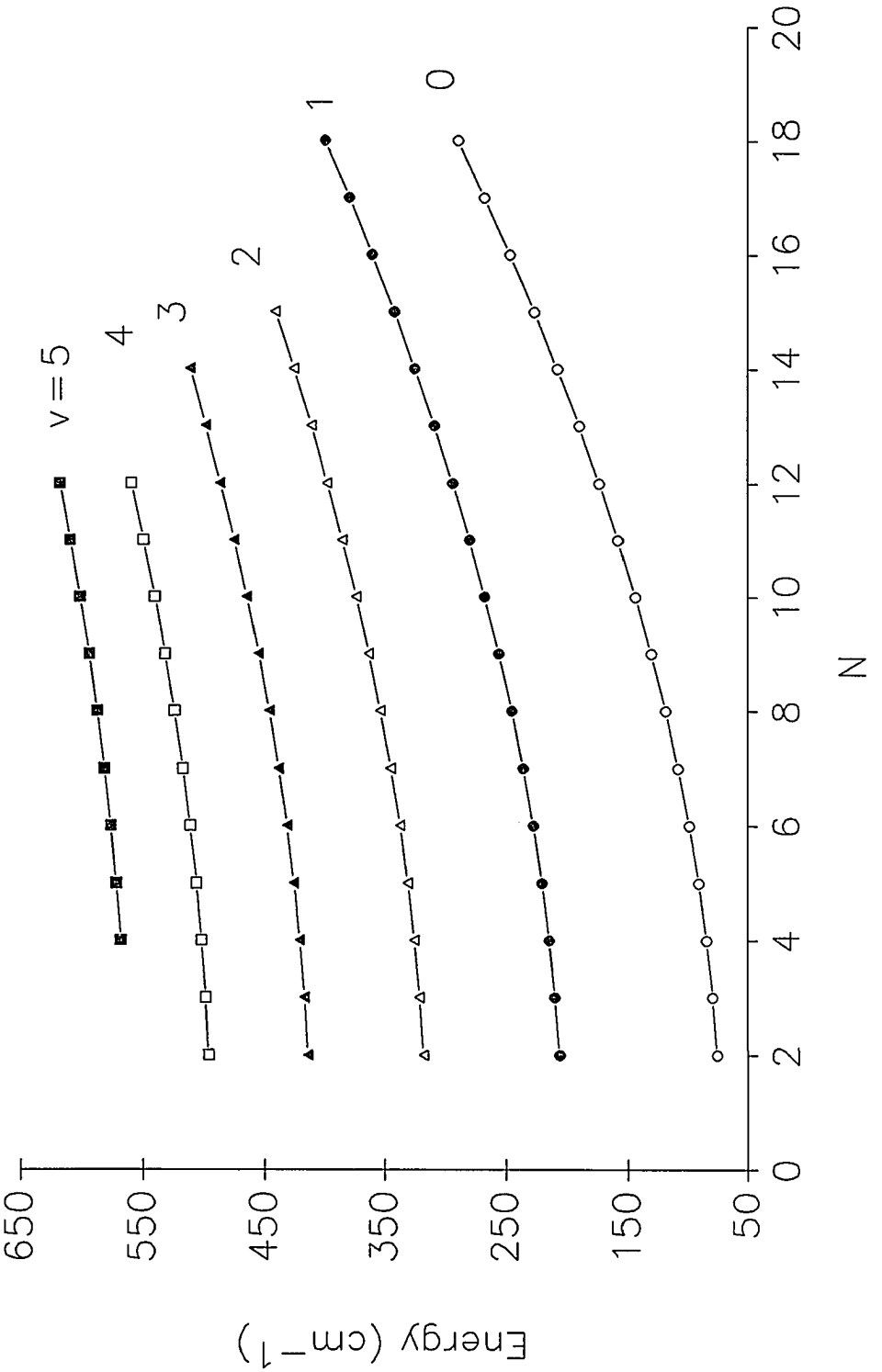

FIGURE 28

Diagram of ro-vibrational energy versus rotational quantum number (N) for each vibrational level of the $3s^2\Sigma^+$ state of $^7Li^{20}Ne$.

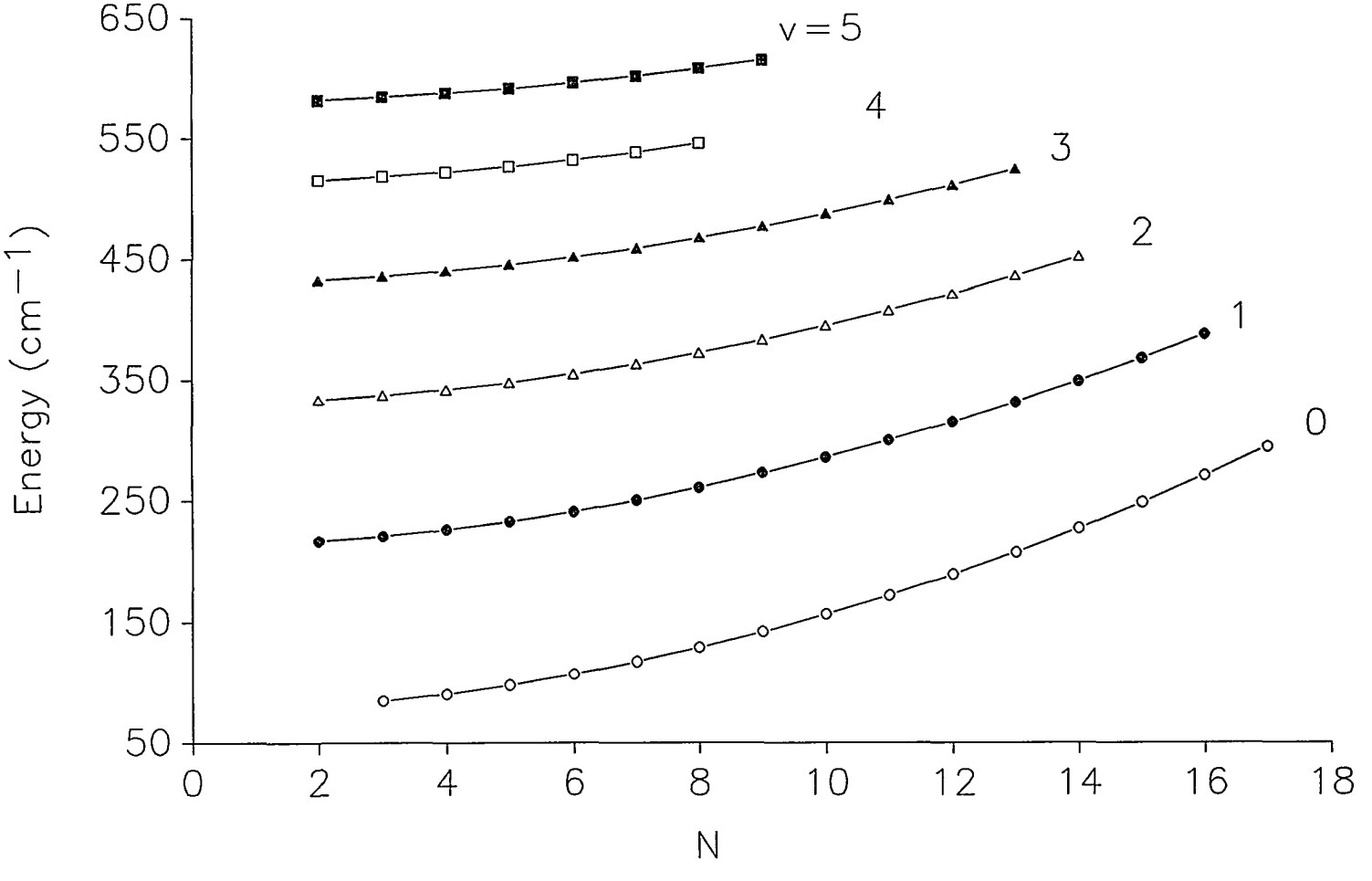

FIGURE 29

IPA potential and the vibrational probability distributions for the LiNe $2p^2\Pi$ state.

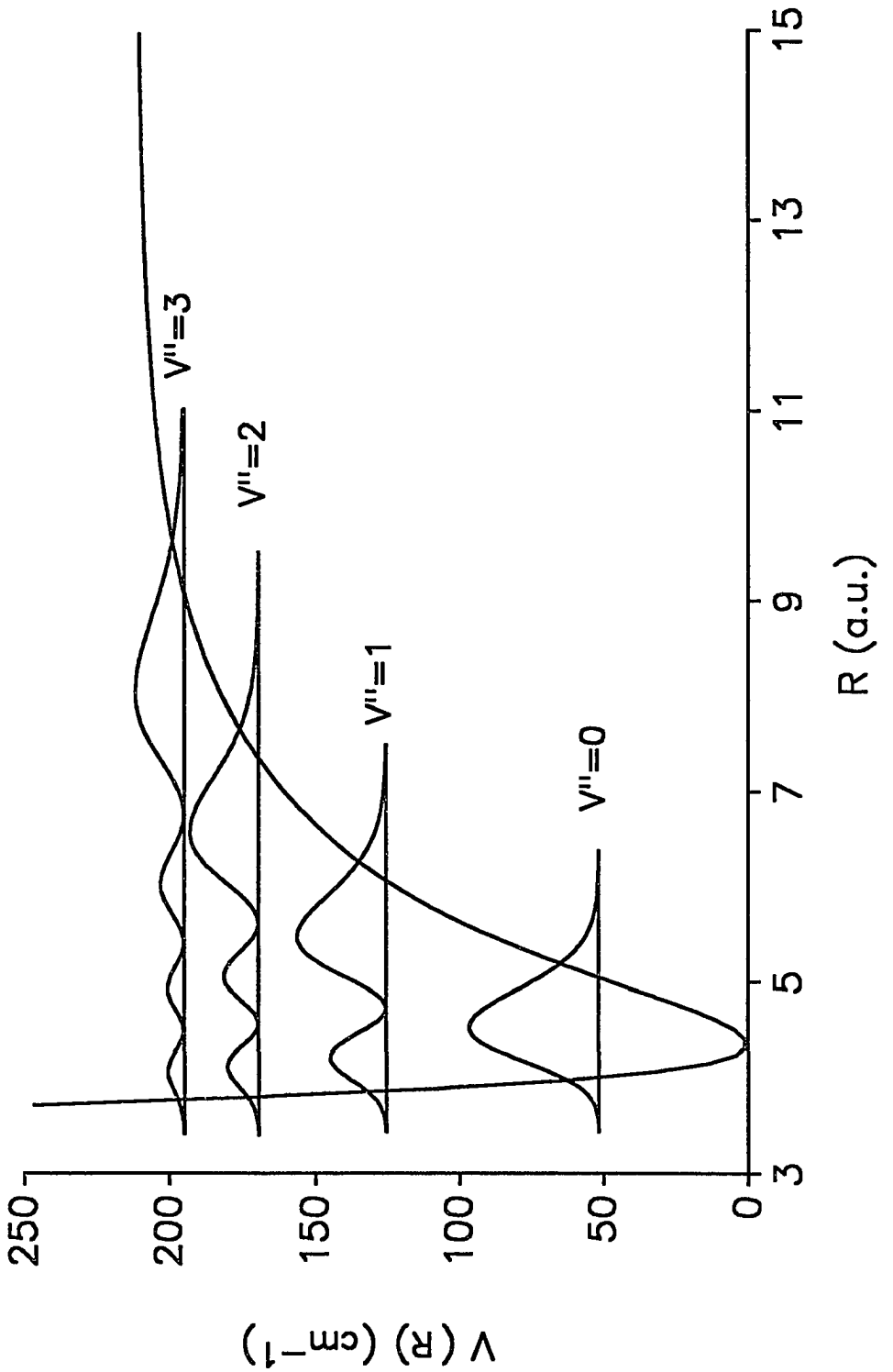

FIGURE 30

IPA potential and the vibrational probability distributions for the LiNe $3s^2\Sigma^+$ state.

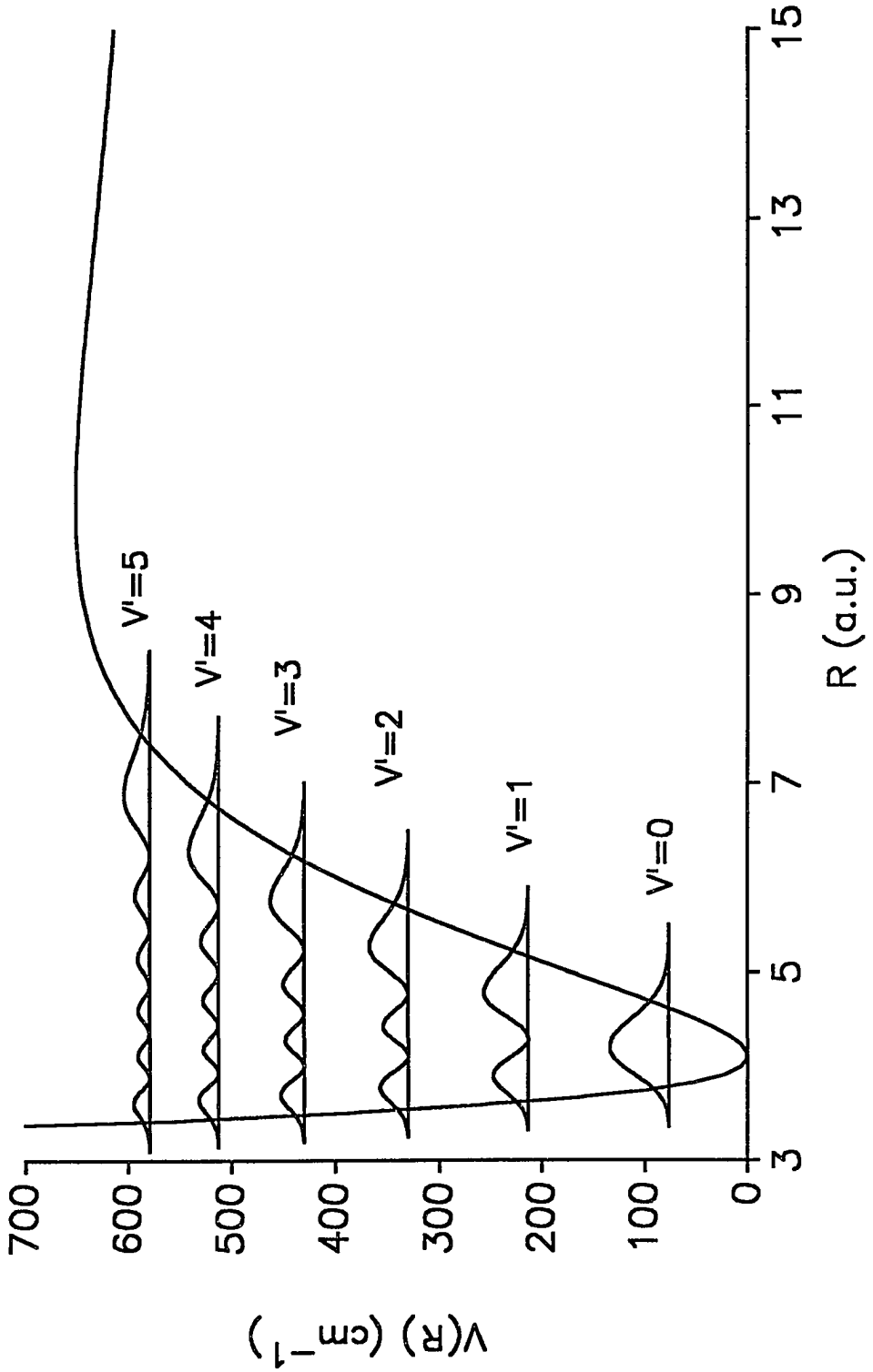

quantum mechanical treatment confirms in a general way the basic assumption of the Frank-Condon principle that transitions vertically upward may take place within a narrow range of the internuclear separation R. Therefore, according to Figures 29 and 30, the intensity of the $3s^2\Sigma^+ \leftarrow 2p^2\Pi$ (v"=0, v'=0) band is expected to be the strongest among the possible transition bands. When the figures are overlapped, it can be seen that this band has the largest overlap of the wavefunction. Notice that for convenience, the square of the unnormalized wavefunctions are drawn in the figures.

For the $3s^2\Sigma^+$ state potential, the vibrational wavefunctions have negligible amplitude in the outer region of the barrier since the barrier width is so large for these levels ($>7\ a_o$). It is difficult, from the data in this experiment, to give an accurate value for the barrier height. To do so would require more experimental data around the barrier.

The IPA fitting procedure determines a potential only within the radial range about 3.5 a_o to 8.5 a_o for which discrete eigenenergies are available. Outside this range only qualitative agreement can be expected with other results.

The coefficients e_i and P describing the IPA $2p^2\Pi$ and $3s^2\Sigma^+$ potential are given in Table 10. The R_e that is determined from equation (5-23) is also provided.

TABLE 10

Parameters used in the IPA method that describe the potentials for the $2p^2\Pi$ and $3s^2\Sigma^+$ states.

	$2p^2\Pi$		$3s^2\Sigma^+$	
	$R>R_e$	$R<R_e$	$R>R_e$	$R<R_e$
P	5.0		3.3	
e_0	189.2	684	749.54	3196
e_1	7.5	7700	54.1	28563
e_2	-11.9		84.4	
e_3	26.80		-282.9	
e_5			-34.40	
R_e (a.u.)	4.363		4.113	

CHAPTER 6

DISCUSSION

The molecular line intensity as a function of N" is expected to behave according to equation (2-62). In Figure 31 the experimentally measured relative intensity divided by the theoretical intensity from equation (2-62), is plotted as a function of N" for the Q branch of $^6Li^{20}Ne$ (v"=0 - v'=0). The intensity ratio is nearly constant up to N"=15 after which it decreases sharply with increasing N". This decrease is due to the rotational predissociation of the $2p^2\Pi$ state. The N"=16 level lies 208.8 cm^{-1} above the bottom of the $2p^2\Pi$ well.

In contrast, for the $^6Li^{20}Ne$ $3s^2\Sigma^+(v'=5) \leftarrow 2p^2\Pi(v"=2)$ transition in Figure 32, a sharp decrease in intensity is measured for P(12), Q(12), and R(12) compared to the N"=11 branch intensities. The N"=12 level lies 220.0 cm^{-1} above the bottom of the $2p^2\Pi$ well and is clearly dissociated. On the other hand, the N"=11 level at 213.2 cm^{-1} shows no evidence of predissociation in the data. Further, the N"=9 level on the v"=3 P-branch is at 215.2 cm^{-1} above the well minimum while N"=8 lies at 211.6 cm^{-1}.

Therefore, the well depth for the $2p^2\Pi$ state is predicted to be 212 cm^{-1} with an estimated uncertainty of about 5 cm^{-1}. Also, as discussed before, the prediction for

FIGURE 31

The experimentally measured relative intensity divided by the theoretical intensity versus N" for the Q branch of $^{6}Li^{20}Ne$ (v"=0 - v'=0).

FIGURE 32

A portion of the (2-5) band of the $^{6}Li^{20}Ne$ rovibrational band, illustrating the effect of rotational predissociation in the $2p^{2}\Pi(2)$ state.

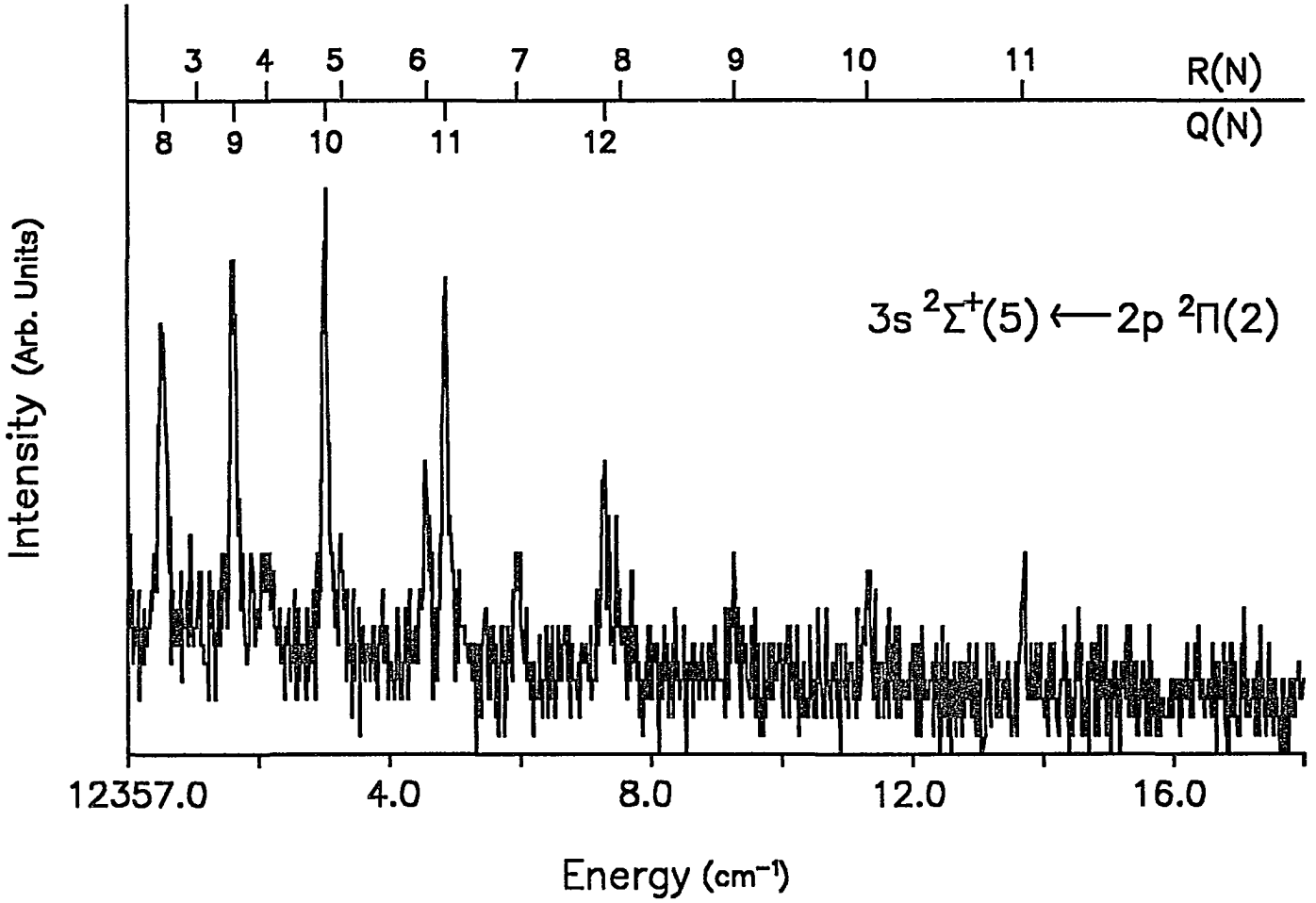

the well depth of the $2p^2\Pi$ state using the IPA method gives 211.9 cm^{-1}. By the long range method, the value of the dissociation energy was predicted to be 210(10) cm^{-1} which supports the above conclusion.

The experimental data clearly show that there is a barrier in the $3s^2\Sigma^+$ potential. The combination of the $2p^2\Pi$ dissociation energy for each isotope with the (0-0) band origins and the atomic Li 2p - 3s transition show that the portion of the $3s^2\Sigma^+$ potential below the Li 3s asymptote has a depth of 570(7) cm^{-1}. The depth is obtained from the following relation [76, 82, 83]:

$$570(7)\,cm^{-1} = \Delta E(2p-3s) + D_e(2p^2\Pi) - \nu_o(v''=0, v'=0)$$

$$+ G(v'=0, 3s^2\Sigma) - G(v''=0, 2p^2\Pi) \qquad (6-1)$$

where G(v"=0, $2p^2\Pi$) and G(v'=0, $3s^2\Sigma^+$) are the zero point energies, ΔE(2p-3s) is 12302.21 cm^{-1} and $D_e(2p^2\Pi)$ is 212(5) cm^{-1}. Even the small fine structure of 2p the state is accounted for in the above calculation [76]. The vibrational level v'=5 is at 581.6 cm^{-1}, and rotational levels extend to 630.6 cm^{-1}, which is above the atomic dissociation asymptote. Therefore, a barrier of 60.6 cm^{-1}, or larger, exists in the $3s^2\Sigma^+$ potential.

The existence of a barrier in the $3s^2\Sigma^+$ potential may be understood in the following way. In the case of the state of 3s atomic Li [87] as shown in Figure 33, a region of about 8 a_o of e^--Li^+ separation has a maximum of electron charge density. Therefore, as the Ne atom is brought from long range toward the Li atom, it experiences a repulsive electrostatic interaction. As the Li-Ne separation is

decreased, the electrostatic repulsion becomes smaller and is overcome by the attractive interaction between the two atoms. Calculations using the model potential of Peach [66] show a long range barrier in many of the adiabatic potentials.

Table 11 shows a comparison of our results for the dissociation energy D_e and the equilibrium distance R_e with others for both the $2p^2\Pi$ and $3s^2\Sigma^+$ states. For the $2p^2\Pi$ state, D_e obtained from the line broadening experiment of Balling, et.al. [34] is in close agreement with our result. The other results differ significantly from ours. Scheps, et. al. [32] reported the dependence on pressure of the intensity of the $2p^2\Pi \rightarrow 2s^2\Sigma^+$ continuum emission spectrum in the range of 40-600 torr. Their upper limit of the well depth in Table 11 is considerably smaller than our result. If accurate lower pressure data could have been obtained in the difficult experiments of Scheps, et. al. [32], it undoubtedly would have revealed the deeper LiNe $2p^2\Pi$ state potentials measured in the experiment. The model potential results of Roberts [66] and the recent pseudopotential calculations of Czuchaj et. al. [21] are in rough agreement with our experiment even though some refinement of these calculations seems necessary.

For the R_e case, the Roberts result agrees with our result within 5 %. Pascal, et. al. [7] and the earlier results of Czuchaj, et. at. [19] show significantly shallower wells and larger internuclear separations than the results of this experiment.

For the $3s^2\Sigma^+$ state potential, the dissociation energy, barrier height, and equilibrium separation are listed in Table 11. The theoretical results do not agree well with the results of this experiment.

If the peak emission intensity in the $3s^2\Sigma^+ \rightarrow 2s^2\Sigma^+$ transition arises from transitions out of the lower part of the $3s^2\Sigma^+$ state [73], the height of the repulsive

FIGURE 33

Radial electronic charge density distribution of the atomic Li 3s state [87].

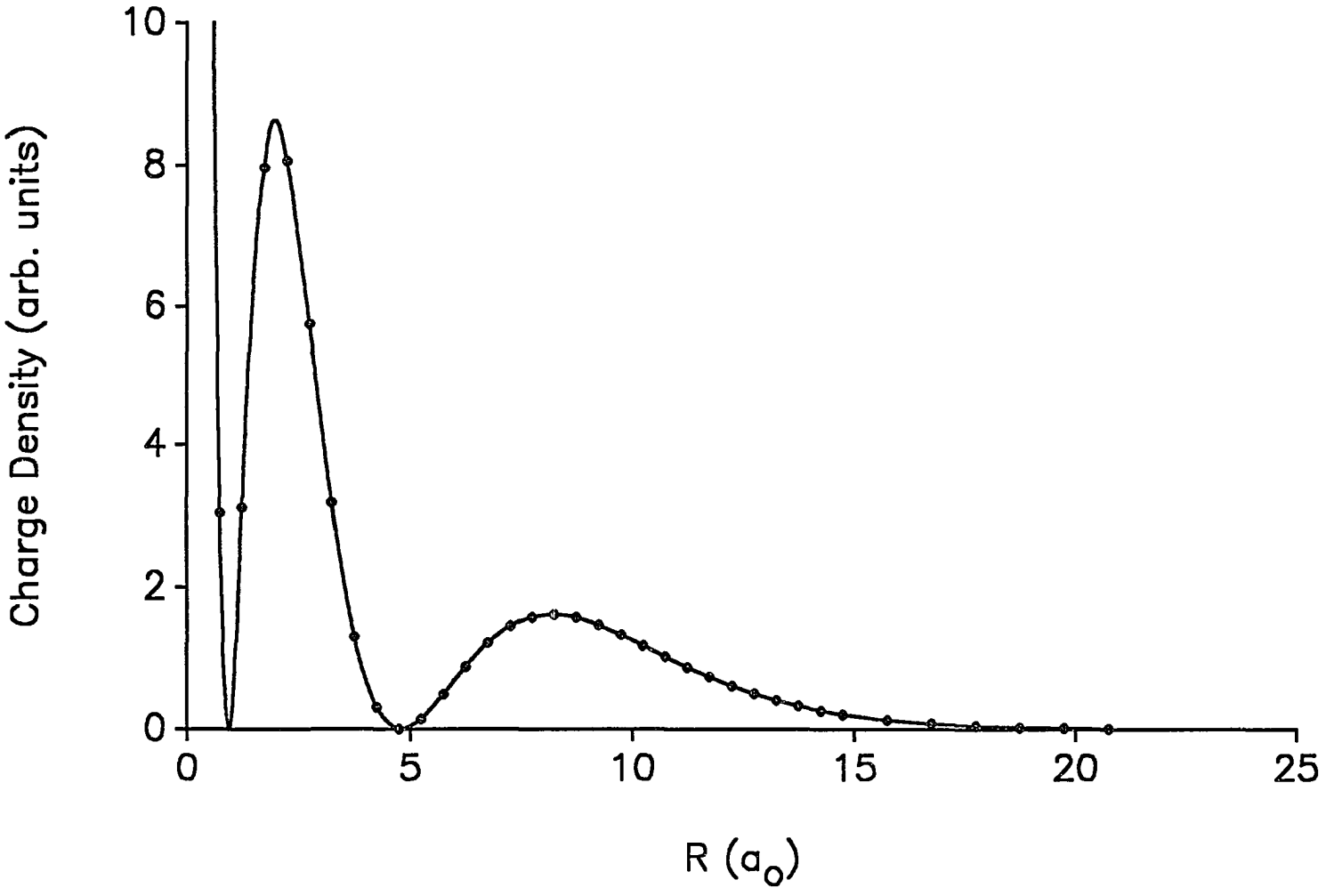

TABLE 11

Comparison of various determinations of the binding energy (D_e), and equilibrium separation (R_e) for the LiNe $3s^2\Sigma^+$ and $2p^2\Pi$ states.

	$2p^2\Pi$	
	D_e (cm^{-1})	R_e (a_o)
This Expt.	212(5)	4.36(2)
Balling et.al. (Ref.34)	225(30)	
Scheps et.al. (Ref.32)	< 160	
Czuchaj et.al. (Ref.21)	22	7.5
Roberts (Ref.66)	289.0	4.5
Pascale et.al. (Ref.7)	16.9	8.0
Czuchaj et.al. (Ref.19)	166.0	4.0

	$3s^2\Sigma^+$		
	D_e (cm^{-1})	Barrier (cm^{-1})	R_e (a_o)
This Expt.	570(7)	> 60.9	4.11(1)
Czuchaj et.al. (Ref.19)	71.3	454.7	5.25
Roberts (Ref.66)	511.6	218.4	4.5
Pascale et.al. (Ref.7)	134.4		5.75

$2s^2\Sigma^+$ potential at the internuclear separation corresponding to the excimer emission peak can be estimated and obtained to be a height of 1300 cm^{-1} at R=4.11 a_o. These numbers are consistent with the results of Balling, et. at. [34] if one sets the radial scale of their potential by the $2p^2\Pi$ state equilibrium R=4.36(2) a_o given in Table 4.

The spin-orbit constant A=2.77(3) cm^{-1} is much larger than the value of A=0.23 cm^{-1} that would be expected in a case (a) limit if the valence electronic state was a 2p orbital centered on the Li^+ ion [76]. Similar effects have also been measured [44, 49 - 51] in the NaAr, NaKr, and NaXe $3p^2\Pi$ states. Cooper [88] has suggested that excitation of the Ne $2p^6$ core perturbs the 3p state. Thus, the possible explanation for a large A for v"=0 is that the nominal Li 2p configuration becomes mixed with excitation of the Ne $2p^6$ configuration, since the spin-orbit interaction constant for those is quite large [89, 90].

CHAPTER 7

SUMMARY

The rotationally resolved $3s^2\Sigma^+ \leftarrow 2p^2\Pi$ absorption spectrum of $^6Li^{20}Ne$ and $^7Li^{20}Ne$ is reported in this dissertation. In this experiment, two dye lasers are employed. One resonantly excites Li atoms to the 2p states and the other is scanned over the range of rovibrational transitions associated with the $3s^2\Sigma^+ \leftarrow 2p^2\Pi$ electronic transition. Molecular LiNe fluorescence on the bound- continuum $3s^2\Sigma^+ \rightarrow 2s^2\Sigma^+$ transition serves as the monitor of molecular LiNe absorption. A specially designed cell is used which directly heats the metal Li providing an estimated density of about 10^{11} cm^{-1} in the center of a cell containing 50 Torr of Ne. Data acquisition and display were controlled by a laboratory computer.

For each isotope, thirteen vibrational transition from four vibrational levels of the lower $2p^2\Pi$ state to six vibrational level of the upper $3s^2\Sigma^+$ state have been observed. For each band, the rotational constants have been obtained along with the vibrational constants and the equilibrium nuclear separation for two electronic states of $^6Li^{20}Ne$ and $^7Li^{20}Ne$.

Adiabatic potentials and dissociation energies for both states have been obtained through the IPA method. For the $2p^2\Pi$ state a well depth of 212(5) cm^{-1} and

an equilibrium separation of 4.36(2) a_o have been obtained. For the $3s^2\Sigma^+$ state, there is a barrier greater than 60 cm^{-1} above the atomic Li 3s asymptote. The well region has a minimum of 570(7) cm^{-1} located at 4.11(1) a_o.

A large spin-orbit constant A=2.77(3) cm^{-1} has been determined for the $2p^2\Pi(v''=0)$ level, while no splitting within our experimental resolution is observed from transitions out of any $2p^2\Pi$ states with $v''>0$. The large spin-orbit constant indicates that states associated with the atomic Ne 2p shell must contribute to the nominal Li 2p configuration of the $^2\Pi$ state.

In conclusion, the $2p^2\Pi$ and $3s^2\Sigma^+$ electronic states of $^6Li^{20}Ne$ and $^7Li^{20}Ne$ diatomic molecules have been studied by rotationally resolved laser spectroscopy. Adiabatic potentials and dissociation energies for both states have been obtained through an inverse perturbation analysis. Also, an anomalously large spin-orbit constant was determined for the $2p^2\Pi(v''=0)$ state. These experimental results were compared with others; most theoretical results do not agree well with the results of this experiment. This experimental technique can be extended to study excited states of other alkali-rare gas systems [52].

REFERENCES

1. L. Krause, "Sensitized Fluorescence and Quenching." in The Excited State in Chemical Physics, John Wiley and Sons (1985).

2. E. E. Nikitin, "Theory of the Nonadiabatic Collision Processes Including Excited Alkali Atoms." in The Excited State in Chemical Physics, John Wiley and Sons (1975).

3. R. P. Saxon, R. E. Olson, and B. Liu, J. Chem. Phys. 67, 2692 (1977).

4. M. Krauss, P. Maldonado, and A. C. Wahl, J. Che,. Phys. 54, 4944 (1971).

5. N. Scheel and V. Griffing, J. Chem. Phys. 36, 1453 (1962).

6. S. B. Schneiderman and H. H. Michels, J. Chem. Phys. 42, 3706 (1965).

7. J. Pascale and J. Vandeplanque, J. Chem. Phys. 60, 2278 (1974).

8. C. Bottcher, Chem. Phys. Lett. 18, 457 (1973).

9. W. E. Baylis, J. Chem. Phys. 51, 2665 (1969).

10. F. Masnou-seeuws, J. Phys. B15, 883 (1982).

11. G. Peach, Comm. At. Mol. Phys. 11, 101 (1982).

12. F. Masnou-seeuws, M. Philippe, and P. Valiron, Phys. Rev. Lett. 41, 395 (1978)

13. R. Düren and G. Moritz, J. Chem. Phys. 73, 5155 (1980).

14. J. N. Bardsley, Case Stud. At. Phys. 4,299 (1974).

15. J. Hanssen, R. McCarrall and P. Valiron, J. Phys. B12, 899 (1979).

16. C. Bottcher, A. Dalgarno, and E. L. Wright, Phys. Rev. 7, 1606 (1973).

17. J. Pascale, Phys. Rev. A28, 632 (1983).

18. M. Phillipe, F. Masnou-Seeuws, and P. J. Valiron, J. Phys. B12, 2493 (1979).

19. E. Czuchaj and J. Sienkiewicz, Z. Naturfursch, Teil A34, 694 (1979).

20. M. Jungen and V. Staemmler, J. Phys. B21, 463 (1988).

21. E. Czuchaj, F. Rebentrost, H. Stoll, and H. Preuss, Chem. Phys. 136, 79 (1989).

22. E. de Prunelé, Phys. Rev. A35, 496 (1987).

23. B. C. Laskoqski, S. R. Langhoff, and J. R. Stallcop, J. Chem. Phys. 75, 815 (1981).

24. M. Dolan and F. Masnou-Seeuws, J. Phys. B14, L583 (1981).

25. R.J. LeRoy and R. B. Bernstein, J. Chem. Phys. 52, 3869 (1970).

26. W. C. Stwalley, Y. Uang and G. Picher, Phys. Rev. Lett. 41, 1164 (1978).

27. K. R. Way and W. C. Stwalley, J. Chem. Phys. 59, 5298 (1973).

28. W. C. Stwalley, J. Chem. Phys. 63, 3063 (1975).

29. R. E. Hedges, D. L. Drummond, and A. Gallagher, Phys. Rev. A6, 1519 (1972).

30. D. L. Drummond and A. Gallagher, J. Chem. Phys. 60, 3426 (1974).

31. G. York, R. Scheps, and A. Gallagher, J. Chem. Phys. 63, 1052 (1975).

32. R. Scheps, Ch. Ottinger, G. York, and A. Gallagher, J. Chem. Phys. 63, 2581 (1975).

33. M. D. Havey, S. E. Frolking, and J. J. Wright, Phys. Rev. Lett. 45, 1783 (1980).

34. L. C. Balling, J. J. Wright, and M. D. Havey, Phys. Rev. A26, 1426 (1982).

35. M. Ferry, J. P. Visiticot, J. Lozingot, and B. Sayer, J. Phys. B13, 2571 (1980).

36. G. M. Carter, D. E. Pritchard, M. Kaplan, and T. W. Ducas, Phys. Rev. Lett. 35, 1144 (1975).

37. P. Dehmer and L. Wharton, J. Chem. Phys. 57, 4821 (1972).

38. R. Düren, and E. Hasselbrink, and G. Moritz, Z. Phys. A307 1 (1982).

39. R. Düren, W. Groger, E. Hasselbrink, and R. Liedtke, J. Chem. Phys. 74, 6806 (1981).

40. R. Düren and W. Groger, Chem. Phys. Lett. 56, 67 (1978).

41. R. Düren and Liedtke, J. Chem. Phys. 74, 6995 (1981).

42. R. Düren, Adv. At. Mol. Phys. 16, 55 (1980).

43. R. Ahmad-Bitar, W. P. Lapatovich, D. E. Pritchard, and I. Renhorn, Phys. Rev. Lett. 39, 1657 (1977).

44. R. E. Smalley, D. J. Auerbach, P. S. H. Fitch, D. H. Levy, and L. Wharton, J. Chem. Phys. 66, 3778 (1977).

45. J. Tellinghuisen, A. Rangone, M. S. Kim, D. J. Auerbach, R. E. Smalley, L. Wharton, and D. H. Levy, J. Chem. Phys. 71, 1283 (1979).

46. W. P. Lapatovich, R. Ahmad-Bitar, P. E. Moslowitz, I. Renhorn, R. A. Gottscho, and D. E. Pritchard, J. Chem. Phys. 73, 5419 (1980).

47. R. A. Gottscho, R. Ahmad-Bitar, W. P. Lapatovich, I. Renhorn, and D. E. Pritchard, J. Chem. Phys. 75, 2546 (1981).

48. M. D. Havey, Phys. Rev. Lett. 48, 1100 (1982).

49. G. Aefelbach, A. Nunnemann, and D. Zimmermann, Chem. Phys. Lett. 96, 311

(1983).

50. E. Zanger, V. Schmatloch, and D. Zimmermann, J. Chem. Phys. 88, 5396 (1988).

51. D. Zimmermen, Private communication.

52. C. J. Lee, M. D. Havey, and R. P. Meyer, Phys. Rev. A43, 77 (1991).

53. R. P. Meyer, M. D. Havey, and C. J. Lee, to be published.

54. M. Born and J. R. Oppenheimer, Ann. Phys. 84, 457 (1927).

55. G. Herzberg, Spectra of Diatomic Molecules, 2nd ed. Van Nostrand, Reinhold, and Co., (New York, 1950).

56. Hélène Lefebvre-Brion and R. W. Field, Perturbations in the Spectra of Diatomic Molecules, Academic Press (1986).

57. J. T. Hougen, NBS Monogram 115 (1970).

58. M. Weissbluth, Atoms and Molecules, Academic Press (1978).

59. A. R. Edmonds, Angular Momentum in Quantum Mechanics, 2nd ed. Princeton University Press (1974).

60. M. E. Rose, Elementary Theory of Angular Momentum, Wiley (N.Y. 1957).

61. J. H. Van Vleck, Rev. Mod. Phys. 23, 213 (1951).

62. E. L. Hill and J. H. Van Vleck, Phys. Rev. 32, 250 (1928).

63. E. Merzbacher, Quantum Mechanics, 2ns. ed., John Wiley & Sons (1970).

64. J. H. Van Vleck, Phys. Rev. 33, 467 (1929).

65. R. S. Mulliken and A. Christy, Phys. Rev. 38, 87 (1931).

66. G. Roberts, private communication. Potentials are calculated using the model potential of G. Peach.

67. I. Kovács, Rotational Structure in the Spectra of Diatomic Molecules, Adam Hilger LTD (London, 1969).

68. J. I. Steinfeld, An Introduction to Modern Molecular Spectroscopy, 2nd ed. The MIT Press (1985).

69. R. E. Hanig, RCA Review, 23, 574 (1962).

70. W. Demtröder, Laser Spectroscopy, 2nd ed. Springer Series in Chemical Physics 5, Springer-Verlag (N.Y. 1982).

71. A. C. G. Mitchell and M. W. Zemansky, Resonance Radiation and Excited Atoms, Cambridge at the University Press (1971).

72. B. A. Palmer, R. A. Keller, and R. Engleman, Jr., An Atlas of Uranium Emission Intensities in a Hollow Cathode Discharge, Informal Report LA-8251MS Los Alamos Scientific Lab. (1980).

73. F. Rostas, "Alkali-Rare Gas Excimers," ed. B. Wende, in Spectral Line Shapes, Walter de Gruyter and Co. (1981).

74. W. J. Wang and M. D. Havey, Phys. Rev. A29, 3184 (1984).

75. R. P. Meyer, C. J. Lee, and M. D. Havey, to be published.

76. C. E. Moore, Atomic Energy Levels, NSRDS-NBS 35, U.S. Government Printing Office (1971).

77. M. Allegrini, G. Alzetta, A. Kopystynska, and L. Moi, Opt. Commun 19, 96 (1976).

78. M. Allegrini, G. Alzetta, A. Kopystynska, L. Moi, and G. Orriols, Opt. Commun 22, 329 (1977).

79. H. G. C. Werij, M. Harris, J. Cooper, A. Gallagher, and J. F. Kelly,

Phys. Rev. A 43, 2237 (1991).

80. CRC Handbook of Chemistry and Physics, 62nd ed., ed. R. C. Weast and M. J. Astle, CRC Press (Boca Raton, 1982).

81. P.R. Bevington, Data Reduction and Error Analysis for the Physical Sciences, Mcgraw-Hill Book Co. (1969).

82. Cohen and Taylor, Mod. Phys. 59, 1139 (1987).

83. F. W. Walker, D. G. Miller, and F. Feiner, Chart of the Nuclides, 13th ed. Knolls Atomic Power Lab. (1983).

84. R. S. Mulliken, Rev. Mod. Phys. 3, 89 (1931).

85. W. M. Koseman and J. Hinze, J. Mol. Spect. 56, 93 (1975).

86. A. J. Thakkar, J. Chem. Phys. 62, 1693 (1975).

87. G. Simons, J. Chem. Phys. 60, 645 (1974).

88. D. L. Cooper, J. Chem. Phys. 75, 4157 (1981).

89. A. A. Radzig and B. M. Smirnov, Reference Data on Atoms, Molecules, and Ions, Springer Series in Chemical Physics 31, Springer-Verlag (1985).

90. C. J. Lee and M. D. Havey, Accepted in Phys. Rev. A (June, 1991).

91. D. Park, Introduction to the Quantum Theory, 2nd ed. McGraw-Hill Book Co. (1974).

92. I. S. Gradshteyn and I. M. Ryzhik, Table of Integrals, Series and Products, Sec.3.251 p295, Academic Press (1965).

93. J. Mathews and Walker, Mathematical Methods of Physics, 2nd. ed., The Benjamin/Cummings Publising Co. (1970).

APPENDIX 1

Measured line positions for the $3s^2\Sigma^+(v', N')\leftarrow 2p^2\Pi(v'', N'')$ transition in LiNe.

$^6Li^{20}Ne$

(0,0)

N"	R(N")	Q(N")	P(N")
2	11975.4(1)	11971.0(1)	11968.1(1)
3	11977.5(1)	11971.7(1)	11967.3(1)
4	11979.9(1)	11972.5(1)	11966.7(1)
5	11982.4(1)	11973.6(1)	11966.4(1)
6	11985.2(1)	11975.0(1)	11966.3(1)
7	11988.2(1)	11976.6(1)	11966.4(1)
8	11991.4(1)	11978.4(1)	11966.9(1)
9	11995.0(1)	11980.6(1)	11967.6(1)
10	11998.7(1)	11983.0(1)	11968.7(1)
11	12002.8(1)	11985.7(1)	11970.0(1)
12	12007.3(1)	11988.8(1)	11971.8(1)
13	12012.0(1)	11992.3(1)	11974.0(1)
14	12017.2(1)	11996.2(1)	11976.6(1)
15	12022.9(1)	12000.6(1)	11979.8(1)
16	12029.2(1)	12005.7(1)	11983.6(1)
17	12036.2(1)	12011.6(1)	11988.3(1)
18	12044.5(1)	12018.7(1)	11994.3(1)

(0,1)

2		12107.0(1)	12104.4(1)
3	12112.5(1)	12107.2(1)	12103.3(1)
4	12114.2(1)	12107.6(1)	12102.3(1)
5	12115.9(1)	12108.0(1)	12101.3(1)
6	12117.7(1)	12108.5(1)	12100.6(1)
7	12119.5(1)	12109.0(1)	12099.9(1)
8	12121.5(1)	12109.8(1)	12099.4(1)
9	12123.6(1)	12110.6(1)	12098.9(1)
10	12125.8(1)	12111.6(1)	12098.7(1)

11	12128.2(1)	12112.8(1)	12098.7(1)
12	12130.8(1)	12114.2(1)	12098.9(1)
13	12133.5(1)	12115.8(1)	12099.4(1)
14	12136.6(1)	12117.7(1)	12100.1(1)
15	12140.0(1)	12120.0(1)	12101.3(1)
16	12143.9(1)	12122.8(1)	12103.0(1)
17	12148.3(1)	12126.2(1)	12105.4(1)
18	12153.8(1)	12130.8(1)	12108.9(1)

(0,2)

7	12231.7(1)		
8	12232.5(1)	12222.0(1)	
9	12233.3(1)	12221.6(1)	
10	12234.1(1)	12221.3(1)	12209.7(1)
11	12234.8(1)	12221.0(1)	12208.4(1)
12	12235.7(1)	12220.8(1)	12207.1(1)
13	12236.5(1)	12220.7(1)	12206.0(1)
14	12237.6(1)	12220.7(1)	12205.0(1)
15	12238.9(1)	12221.0(1)	12204.3(1)
16	12240.4(1)	12221.6(1)	12204.0(1)
17	12242.4(1)	12222.8(1)	12204.3(1)
18	12245.3(1)	12224.8(1)	12205.5(1)

(1,0)

1		11896.8(1)	11895.3(1)
2	11902.2(1)	11897.8(1)	11894.9(1)
3	11905.1(1)	11899.2(1)	11894.9(1)
4	11908.4(1)	11901.1(1)	11895.3(1)
5	11912.3(1)	11903.6(1)	11896.3(1)
6	11916.7(1)	11906.5(1)	11897.8(1)
7	11921.6(1)	11910.0(1)	11899.8(1)
8	11927.0(1)	11914.0(1)	11902.5(1)
9	11933.1(1)	11918.7(1)	11905.7(1)
10	11939.8(1)	11924.0(1)	11909.7(1)
11	11947.2(1)	11930.1(1)	11914.4(1)
12	11955.4(1)	11936.9(1)	11919.9(1)
13	11964.5(1)	11944.8(1)	11926.4(1)
14		11953.7(1)	11934.1(1)

(1,1)

1	12035.8(1)	12033.1(1)	12031.8(1)
2	12037.8(1)	12033.8(1)	12031.2(1)
3	12040.1(1)	12034.8(1)	12030.8(1)
4	12042.7(1)	12036.2(1)	12030.9(1)
5	12045.8(1)	12037.9(1)	12031.3(1)
6	12049.1(1)	12040.0(1)	12032.1(1)
7	12052.9(1)	12042.4(1)	12033.3(1)

8	12057.1(1)	12045.4(1)	12034.9(1)
9	12061.7(1)	12048.7(1)	12037.1(1)
10	12066.8(1)	12052.6(1)	12039.8(1)
11	12072.7(1)	12057.1(1)	12043.0(1)
12	12078.9(1)	12062.3(1)	12047.0(1)
13	12086.1(1)	12068.3(1)	12051.8(1)
14	12094.2(1)	12075.4(1)	

(1,2)

1			12148.7(1)
2	12153.9(1)	12150.3(1)	12148.0(1)
3	12155.7(1)	12150.9(1)	12147.4(1)
4	12157.7(1)	12151.7(1)	12147.0(1)
5	12159.7(1)	12152.8(1)	12146.9(1)
6	12162.6(1)	12154.1(1)	12147.0(1)
7	12165.1(1)	12155.7(1)	12147.4(1)
8	12168.1(1)	12157.5(1)	12148.2(1)
9	12171.4(1)	12159.7(1)	12149.3(1)
10	12175.1(1)	12162.3(1)	12150.8(1)
11	12179.2(1)	12165.4(1)	12152.8(1)
12	12183.8(1)	12168.9(1)	12155.2(1)
13	12189.1(1)	12173.2(1)	12158.5(1)
14	12195.2(1)	12178.3(1)	12162.3(1)
15	12202.5(1)	12184.6(1)	12168.0(1)

(1,3)

2	12252.5(2)	12249.3(1)	12247.2(1)
3	12253.9(1)	12249.5(1)	12246.3(1)
4	12255.1(1)	12249.8(1)	12245.6(1)
5	12256.6(1)	12250.3(1)	12245.0(1)
6	12258.2(1)	12250.8(1)	12244.4(1)
7	12259.9(1)	12251.5(1)	12244.1(1)
8	12261.7(1)	12252.4(1)	12244.0(1)
9	12263.8(1)	12253.4(1)	12244.2(1)
10	12266.0(1)	12254.7(1)	12244.5(1)
11	12268.6(1)	12256.3(1)	12245.1(1)
12	12271.7(1)	12258.4(1)	12246.2(1)
13	12274.9(1)	12260.9(1)	12247.9(1)
14	12279.1(1)	12264.2(1)	12250.3(1)
15	12284.3(1)	12268.6(1)	12253.9(1)
16			12258.1(1)

(1,4)

6	12337.5(1)		
7	12338.2(1)	12330.8(1)	12324.4(1)
8	12338.9(1)	12330.7(1)	12323.4(1)
9	12339.7(1)	12330.7(1)	12322.4(1)

10	12340.5(1)	12330.6(1)	12321.6(1)
11	12341.5(1)	12330.8(1)	12321.0(1)
12	12342.7(1)	12331.2(1)	12320.7(1)
13	12344.2(1)	12332.0(1)	12320.7(1)
14	12346.2(1)	12333.4(1)	12321.4(1)
15	12349.2(1)	12335.7(1)	12323.1(1)

(2,0)

1	11855.8(1)	11852.9(1)	11851.4(1)
2	11858.8(1)	11854.4(1)	11851.4(1)
3	11862.5(1)	11856.5(1)	11852.1(1)
4	11866.8(1)	11859.5(1)	11853.6(1)
5	11871.9(1)	11863.1(1)	11855.9(1)
6	11877.8(1)	11867.6(1)	11858.9(1)
7	11884.5(1)	11872.9(1)	11862.8(1)
8	11892.1(1)	11879.1(1)	11867.6(1)
9	11900.6(1)	11886.2(1)	11873.3(1)
10		11894.4(1)	11880.1(1)
11		11903.7(1)	11888.0(1)

(2,3)

2	12209.1(1)		
3	12211.1(1)	12206.9(1)	12203.7(1)
4	12213.5(1)	12208.2(1)	12204.0(1)
5	12216.2(1)	12209.8(1)	12204.6(1)
6	12219.3(1)	12211.9(1)	12205.6(1)
7		12214.5(1)	

(2,4)

1		12287.9(2)	
2	12291.2(2)	12288.4(1)	
3	12292.7(1)	12289.0(1)	
4	12294.5(1)	12289.8(1)	12286.0(1)
5	12296.5(1)	12290.9(1)	12286.2(1)
6	12298.7(1)	12292.2(1)	12286.6(1)
7		12293.8(1)	12287.4(1)
8		12295.8(1)	12288.4(1)
9		12298.2(1)	12290.0(1)
10			12292.0(1)

(2,5)

2	12357.0(1)	12354.6(1)	
3	12358.1(1)	12354.8(1)	12352.3(1)
4	12359.1(1)	12355.1(1)	12351.9(1)
5	12360.3(1)	12355.5(1)	12351.5(1)

6	12361.6(1)	12356.0(1)	12351.3(1)
7	12363.0(1)	12356.7(1)	12351.2(1)
8	12364.5(1)	12357.5(1)	12351.4(1)
9	12366.3(1)	12358.6(1)	12351.7(1)
10	12368.3(1)	12360.0(1)	12352.5(1)
11	12370.7(1)	12361.9(1)	

(3,0)

1	11830.6(1)		
2	11834.0(1)	11829.6(1)	
3	11838.3(1)	11832.4(1)	
4	11843.5(1)	11836.2(1)	11830.3(1)
5	11849.7(1)	11841.0(1)	11833.7(1)
6		11846.8(1)	11838.1(1)
7			11843.6(1)
8			11850.3(1)

$^{7}Li^{20}Ne$

(0,0)

3		11969.9(1)	
4	11977.2(1)	11970.7(1)	11965.4(1)
5	11979.5(1)	11971.6(1)	11965.1(1)
6	11981.9(1)	11972.8(1)	11965.1(1)
7	11984.6(1)	11974.2(1)	11965.2(1)
8	11987.4(1)	11975.8(1)	11965.5(1)
9	11990.5(1)	11977.7(1)	11966.1(1)
10	11993.9(1)	11979.7(1)	11966.9(1)
11	11997.5(1)	11982.1(1)	11968.1(1)
12	12001.3(1)	11984.7(1)	11969.5(1)
13	12005.4(1)	11987.7(1)	11971.3(1)
14	12009.9(1)	11991.0(1)	11973.4(1)
15	12014.7(1)	11994.7(1)	11976.0(1)
16	12020.0(1)	11998.9(1)	11979.0(1)
17	12025.8(1)	12003.6(1)	11982.7(1)
18	12032.3(1)	12009.0(1)	11987.0(1)
19	12039.7(1)	12015.4(1)	11992.3(1)

(0,1)

3		12099.2(1)	12095.5(1)
4		12099.4(1)	12094.6(1)
5		12099.8(1)	12093.8(1)
6	12108.4(1)	12100.2(1)	12093.1(1)
7	12110.3(1)	12100.8(1)	12092.5(1)

8	12111.9(1)	12101.4(1)	12092.0(1)
9	12113.8(1)	12102.1(1)	12091.7(1)
10	12115.9(1)	12103.0(1)	12091.4(1)
11	12118.0(1)	12104.1(1)	12091.4(1)
12	12120.3(1)	12105.3(1)	12091.5(1)
13	12122.7(1)	12106.7(1)	12091.8(1)
14	12125.4(1)	12108.3(1)	12092.4(1)
15	12128.3(1)	12110.2(1)	12093.3(1)
16	12131.5(1)	12112.4(1)	12094.5(1)
17	12135.1(1)	12115.1(1)	12096.2(1)
18	12139.3(1)	12118.3(1)	12098.5(1)
19	12144.2(1)	12122.3(1)	12101.6(1)
20			12105.3(1)
21			12110.2(1)

(0,2)

8	12219.1(1)		
9	12220.1(1)	12209.5(1)	12200.0(1)
10	12220.9(1)	12209.2(1)	12198.7(1)
11	12221.6(1)	12209.1(1)	12197.5(1)
12	12222.4(1)	12208.8(1)	12196.4(1)
13	12223.3(1)	12208.7(1)	12195.4(1)
14	12224.2(1)	12208.9(1)	12194.6(1)
15	12225.4(1)	12209.1(1)	12193.8(1)
16	12226.7(1)	12209.5(1)	12193.4(1)
17	12228.2(1)	12210.2(1)	12193.3(1)
18	12230.2(1)	12211.4(1)	12193.6(1)
19	12232.8(1)	12213.3(1)	12194.7(1)

(1,0)

1			11896.0(1)
2	11902.2(1)	11898.3(1)	11895.7(1)
3	11904.8(1)	11899.6(1)	11895.7(1)
4	11907.7(1)	11901.2(1)	11896.0(1)
5	11911.1(1)	11903.2(1)	11896.7(1)
6	11914.8(1)	11905.8(1)	11897.9(1)
7	11919.1(1)	11908.7(1)	11899.6(1)
8	11923.8(1)	11912.1(1)	11901.8(1)
9	11928.9(1)	11916.1(1)	11904.5(1)
10	11934.6(1)	11920.6(1)	11907.7(1)
11	11941.0(1)	11925.6(1)	11911.6(1)
12	11947.9(1)	11931.3(1)	11916.1(1)
13	11955.5(1)	11937.8(1)	11921.3(1)
14	11963.9(1)	11945.0(1)	11927.5(1)
15		11953.3(1)	11934.6(1)
16		11962.9(1)	11943.0(1)

(1,1)

1		12027.3(1)	12026.1(1)
2		12027.8(1)	12025.4(1)
3	12033.4(1)	12028.7(1)	12025.1(1)
4	12035.8(1)	12029.9(1)	12025.1(1)
5	12038.4(1)	12031.3(1)	12025.4(1)
6	12041.4(1)	12033.1(1)	12026.0(1)
7	12044.7(1)	12035.2(1)	12027.0(1)
8	12048.3(1)	12037.7(1)	12028.3(1)
9	12052.2(1)	12040.6(1)	12030.1(1)
10	12056.7(1)	12043.9(1)	12032.2(1)
11	12061.5(1)	12047.6(1)	12034.9(1)
12	12066.8(1)	12051.9(1)	12038.1(1)
13	12072.8(1)	12056.7(1)	12041.9(1)
14	12079.4(1)	12062.3(1)	

(1,2)

2		12139.8(1)	12137.7(1)
3	12144.6(1)	12140.3(1)	12137.1(1)
4	12146.4(1)	12141.1(1)	12136.7(1)
5	12148.4(1)	12141.9(1)	12136.6(1)
6	12150.6(1)	12143.0(1)	12136.7(1)
7	12152.9(1)	12144.4(1)	12137.0(1)
8	12155.5(1)	12146.0(1)	12137.5(1)
9	12158.4(1)	12147.9(1)	12138.4(1)
10	12161.6(1)	12150.0(1)	12139.5(1)
11	12165.1(1)	12152.5(1)	12141.1(1)
12	12169.0(1)	12155.5(1)	12143.0(1)
13	12173.4(1)	12158.9(1)	12145.5(1)
14	12178.3(1)	12162.9(1)	12148.6(1)
15	12184.0(1)	12167.7(1)	12152.5(1)
16	12190.6(1)	12173.5(1)	12157.4(1)
17			12162.9(1)

(1,3)

2		12235.9(1)	12234.0(1)
3	12240.0(1)	12236.2(1)	12233.3(1)
4	12241.3(1)	12236.4(1)	12232.6(1)
5	12242.6(1)	12236.8(1)	12232.0(1)
6	12244.0(1)	12237.3(1)	12231.5(1)
7	12245.6(1)	12237.9(1)	12231.2(1)
8	12247.3(1)	12238.6(1)	12231.0(1)
9	12249.0(1)	12239.5(1)	12231.0(1)
10	12251.0(1)	12240.7(1)	12231.2(1)
11	12253.2(1)	12242.0(1)	12231.7(1)
12	12255.7(1)	12243.6(1)	12232.5(1)
13	12258.5(1)	12245.6(1)	12233.6(1)
14	12261.8(1)	12248.1(1)	12235.3(1)

15	12265.7(1)	12251.2(1)	

(1,4)

9		12316.6(1)	
10		12316.5(1)	
11		12316.6(1)	12307.2(1)
12	12327.6(1)	12317.0(1)	12306.9(1)
13	12328.9(1)	12317.5(1)	12306.9(1)
14	12330.5(1)	12318.4(1)	12307.1(1)
15	12332.6(1)	12319.9(1)	12308.0(1)
16	12335.4(1)	12322.2(1)	12309.6(1)

(2,0)

1			11852.1(1)
2	11858.7(1)	11854.6(1)	11852.1(1)
3	11861.8(1)	11856.6(1)	11852.6(1)
4	11865.5(1)	11859.0(1)	11853.8(1)
5	11870.1(1)	11862.2(1)	11855.7(1)
6	11875.1(1)	11866.0(1)	11858.2(1)
7	11880.9(1)	11870.5(1)	11861.4(1)
8	11887.3(1)	11875.7(1)	11865.4(1)
9	11894.7(1)	11881.7(1)	11870.2(1)
10	11902.7(1)	11888.6(1)	11875.7(1)
11	11911.8(1)	11896.3(1)	11882.3(1)
12	11921.7(1)	11905.1(1)	11889.9(1)
13		11915.1(1)	

(2,3)

2		12192.3(1)	12190.4(1)
3	12197.1(1)	12193.2(1)	12190.3(1)
4	12199.2(1)	12194.3(1)	12190.4(1)
5	12201.6(1)	12195.8(1)	12191.0(1)
6	12204.3(1)	12197.5(1)	12191.8(1)
7	12207.4(1)	12199.7(1)	12193.0(1)
8	12210.8(1)	12202.3(1)	
9	12214.7(1)	12205.2(1)	

(2,4)

1	12275.0(1)		12272.6(1)
2	12276.3(1)	12273.7(1)	12272.0(1)
3	12277.7(1)	12274.2(1)	12271.6(1)
4	12279.2(1)	12274.9(1)	12271.5(1)
5	12280.9(1)	12275.9(1)	12271.6(1)
6	12283.0(1)	12277.0(1)	12271.9(1)
7	12285.3(1)	12278.4(1)	12272.5(1)

8	12287.8(1)	12280.1(1)	12273.3(1)
9	12290.5(1)	12282.1(1)	12274.5(1)
10	12293.7(1)	12284.5(1)	12276.2(1)
11	12297.3(1)	12287.3(1)	12278.2(1)
12		12290.7(1)	12281.0(1)
(2,5)			
4		12341.1(1)	12338.1(2)
5	12346.0(2)	12341.5(1)	12337.8(1)
6	12347.2(1)	12342.0(1)	12337.5(1)
7	12348.5(2)	12342.6(1)	12337.5(1)
8	12350.0(1)	12343.4(1)	12337.5(1)
9	12351.7(1)	12344.4(1)	12337.8(1)
10	12353.6(1)	12345.7(1)	12338.4(1)
11	12355.8(1)	12347.2(1)	12339.4(1)
12	12358.3(1)	12349.2(1)	12340.8(1)
13	12361.5(1)	12351.7(1)	12342.8(1)
(3,0)			
3		11831.2(1)	
4		11834.5(1)	11829.3(1)
5		11838.5(1)	11832.1(1)
6		11843.5(1)	11835.7(1)
7		11849.4(1)	11840.4(1)
8			11845.9(1)

APPENDIX 2

Rotational and rotational distortion constants for each transition of the $3s^2\Sigma^+$ and $2p^2\Pi$ states.

$^6Li^{20}Ne$

	$2p^2\Pi$			$3s^2\Sigma^+$	
(v",v')	B_v"	D_v"*	H_v"**	B_v'	D_v'*
(0,0)	0.618(4)	0.49(20)	-0.31(3)	0.734(2)	0.81(4)
(0,1)	0.619(4)	0.57(21)	-0.30(4)	0.664(2)	0.84(4)
(0,2)	0.618(3)	0.53(14)	-0.30(2)	0.601(1)	0.93(2)
(1,0)	0.494(5)	1.43(49)	-0.48(14)	0.733(3)	0.76(10)
(1,1)	0.496(5)	1.56(56)	-0.43(18)	0.664(3)	0.84(11)
(1,2)	0.489(5)	0.78(38)	-0.68(9)	0.597(2)	0.80(7)
(1,3)	0.496(4)	1.48(34)	-0.51(8)	0.535(2)	0.93(7)
(1,4)	0.494(2)	1.31(2)	-0.52(6)	0.473(2)	1.03(5)
(2,0)	0.380(4)	3.55(28)		0.734(4)	0.83(29)
(2,3)	0.38(1)	2.7(2.1)		0.53(1)	0.6(1.7)
(2,4)	0.376(7)	2.88(86)		0.472(9)	0.6(1.1)
(2,5)	0.378(5)	3.39(30)		0.408(4)	1.42(26)

(3,0)	0.271(15)	4.38(1.58)		0.734(2)	0.80(10)
$^{7}Li^{20}Ne$					
(0,0)	0.552(3)	0.38(18)	-0.21(3)	0.655(2)	0.63(3)
(0,1)	0.557(4)	0.65(17)	-0.17(3)	0.597(2)	0.67(3)
(0,2)	0.555(3)	0.51(12)	-0.19(2)	0.543(1)	0.71(2)
(1,0)	0.449(4)	0.94(34)	-0.38(8)	0.655(3)	0.62(8)
(1,1)	0.452(6)	1.34(6)	-0.24(19)	0.596(3)	0.65(11)
(1,2)	0.451(4)	1.15(28)	-0.32(6)	0.540(2)	0.66(6)
(1,3)	0.451(5)	1.21(46)	-0.29(13)	0.488(3)	0.71(9)
(1,4)	0.451(2)	1.16(22)	-0.31(6)	0.433(2)	0.71(6)
(2,0)	0.356(3)	2.91(16)		0.656(3)	0.63(15)
(2,3)	0.351(9)	2.58(1.09)		0.487(7)	0.74(81)
(2,4)	0.353(4)	2.79(18)		0.433(4)	0.72(18)
(2,5)	0.359(4)	3.14(15)		0.381(3)	0.97(13)
(3,0)	0.259(15)	3.27(1.58)		0.655(2)	0.63(8)

* 10^{-4}

** 10^{-6}

APPENDIX 3

DERIVATION OF A FITTING EQUATION FOR THE LONG RANGE ANALYSIS

The WKB approximation can be applied to derive an equation for the energies of bound states. The condition on the WKB approximation is similar to that of the quantization of the action integral. The WKB quantum condition [91] is

$$(v+\frac{1}{2})\pi = \int_{R_1(v)}^{R_2(v)} \sqrt{\{\frac{2\mu}{\hbar^2}[E(v)-V(R)]\}}\,dR \qquad \text{(A3-1)}$$

where $E(v) > V(R)$ and is the energy of level v. $R_1(v)$ and $R_2(v)$ are the classical turning points. Differentiation of equation (A3-1) with respect to E(v) yields

$$\frac{dv}{dE(v)} = \frac{\sqrt{\mu/2}}{\pi\hbar}\int_{R_1(v)}^{R_2(v)} [E(v)-V(R)]^{-1/2}\,dR \qquad \text{(A3-2)}$$

By putting

$$V(R) = D - \frac{C_n}{R^n} \qquad \text{(A3-3)}$$

$$and \quad E(v) = D - \frac{C_n}{R_2^n(v)} \qquad \text{(A3-4)}$$

$$\therefore \quad C_n = -R_2^n\{E(v) - D\} \qquad \text{(A3-5)}$$

By substituting equations (A3-3) and (A3-5) into equation (A3-2)

$$\frac{dv}{dE(v)} = \frac{\sqrt{\mu/2}}{\pi\hbar}\int_{R_1(v)}^{R_2(v)} [\{D-E(v)\}\{(\frac{R_2}{R})^n - 1\}]^{-1/2} dR$$

$$= \frac{R_2\sqrt{\mu/2}}{\pi\hbar\sqrt{D-E(v)}}\int_1^{R_2/R_1} y^{-2}(y^n-1)^{-1/2} dy$$

where $y=R_2/R$ and $R_2=[C_n/\{D\text{-}E(v)\}]^{1/n}$. Thus

$$\frac{dv}{dE(v)} = \frac{\sqrt{\mu/2}}{\pi\hbar}\frac{C_n^{1/n}}{\{D-E(v)\}^{\frac{1}{2}+\frac{1}{n}}}\int_1^{R_2/R_1} y^{-2}(y^n-1)^{-1/2} dy \qquad (A3\text{-}6)$$

In the limit $R_1(v)\rightarrow 0$ then the integration can be solved [92]

$$\int_1^{\infty} y^{-2}(y^n-1)^{-1/2} dy = \frac{1}{n}B(\frac{n+2}{2n}, \frac{1}{2}) = \frac{\sqrt{\pi}}{n}\frac{\Gamma(\frac{n+2}{2n})}{\Gamma(\frac{n+1}{n})} \qquad (A3\text{-}7)$$

where n>2, B is the Beta function, and Γ is the Gamma function [93]. Therefore,

$$\frac{dE(v)}{dv} = \hbar\sqrt{\frac{2\pi}{\mu}}\frac{\Gamma(\frac{n+1}{n})}{\Gamma(\frac{n+2}{2n})}\frac{n}{C_n^{1/n}}[D-E(v)]^{(n+2)/2n}$$

$$\equiv K_n[D-E(v)]^{(n+2)/2n} \qquad (A3\text{-}8)$$

Again, changing the variable to y=D-E(v) then equation (A3-8) becomes

$$-\frac{dy}{dv} = K_n y^{(n+2)/2n} \qquad \text{(A3-9)}$$

Integrating equation (A3-9) from v=v to v_D

$$\int_v^{v_D} -y^{-(n+2)/2n}dy = \int_v^{v_D} K_n dv \qquad \text{(A3-10)}$$

Then equation (A3-10) yields

$$\frac{2n}{n-2}[D-E(v)]^{(n-2)/2n} = K_n(v_D - v) \qquad \text{(A3-11)}$$

where $H_n=K_n(n-2)/(2n)$. Equation (A3-11) was first derived by LeRoy and Bernstein [25]. Therefore,

$$[D - E(v)]^{(n-2)/2n} = C(v_D - v) \qquad \text{(A3-12)}$$

where C is a constant.

BIOGRAPHY

Chang Jae Lee was born in Po-Hang, Korea(South) on June 17, 1958. and grew up mostly in Dae-Gu, Korea. He entered the Young-Nam University at Kyung-San, Korea, and received his Bachelor of Science Degree in physics in 1982. After attending the Master of Science program for one semester in Young-Nam University, he came to America to study at Hampton University in 1983. He received his Master of Science Degree. The thesis title was "Reduction of Threshold Pump Power of a Dye Laser Using Converter Techniques" and his advider was Dr. Demetrius Venable. He married Miss Yun H. Shon Lee in June 1985. In July 1985, he started research and study under the direction of Dr. Mark D. Havey. His son was born in Norfolk, Virginia on May 10, 1987. During his graduate studies, three papers were published and four papers are being prepared for publication. He also presented four contributed talks at scientific meetings. He was Public Relation Secretary of the South Eastern Virginia Chapter of Korean Scientists and Engineers Association in America (KSEA) during August, 1989 through August, 1990. He is a member of KSEA, the American Physics Honor Society (Sigma Pi Sigma) and the American Physical Society (APS).

PUBLICATIONS

C. J. Lee, M. D. Havey and R. P. Meyer, "Laser Spectroscopy of Molecular LiHe: The $3d^2\Delta \leftarrow 2p^2\Pi$ Transition." Phys. Rev. A43, 77 (1991).

C. J. Lee and M. D. Havey, "Laser Spectroscopy of $3s^2\Sigma^+ \leftarrow 2p^2\Pi$ Transition in LiNe" Phys. Rev. A43 (June 1991).

C. J. Lee, "Laser Spectroscopy of the $3s^2\Sigma^+ \leftarrow 2p^2\Pi$ Transition in $^{6,7}Li^{20}Ne$ van der Waals Molecules" Proceedings of KSEA Workshop in Raleigh (Feb. 1991)